ANL-02/13

ANL/CRIEPI Collaborative Program for Evaluation of Irradiated EBR-II Stainless Steel

Final Report

By Todd Allen, Jim Cole, Hanchung Tsai,
Ross Jensen, Kermit Bunde, Joji Ohta,
Kenji Dohi, and Hideo Kusanagi

Argonne National Laboratory, Argonne, Illinois 60439
operated by The University of Chicago
for the United States Department of Energy under Contract W-31-109-Eng-38

ANL-02/13

ANL/CRIEPI COLLABORATIVE PROGRAM FOR EVALUATON OF IRRADIATED EBR-II STAINLESS STEELS

Final Report

by

Todd Allen, Jim Cole, Hanchung Tsai, Ross Jensen, and Kermit Bunde
Argonne National Laboratory
9700 South Cass Avenue
Argonne, IL 60439

and

Joji Ohta, Kenji Dohi, and Hideo Kusanagi
Central Research Institute of Electric Power Industry
Iwado Kita, Komae-shi, Tokyo 201
Japan

May 2002

Argonne National Laboratory, with facilities in the states of Illinois and Idaho, is owned by the United States Government and operated by The University of Chicago under the provisions of a contract with the Department of Energy.

Available electronically at http://www.doe.gov/bridge

Available for a processing fee to U.S. Department of Energy and its contractors, in paper, from:

U.S. Department of Energy
Office of Scientific and Technical Information
P.O. Box 62
Oak Ridge, TN 37831-0062
phone: (865) 576-8401
fax: (865) 576-5728
email: reports@adonis.osti.gov

TABLE OF CONTENTS

Page

TABLE OF CONTENTS
(Contd.)

LIST OF FIGURES

Page

LIST OF FIGURES
(Contd.)

LIST OF TABLES

Page

INTRODUCTION

The objective of this collaboration between Argonne National Laboratory (ANL) and the Central Research Institute of Electric Power Industry (CRIEPI) is to evaluate the effects of long-term, low-dose neutron exposure on the mechanical properties, dimensional stability, and associated microstructural changes of reactor structural materials. ANL believes that material data obtained from components irradiated in EBR-II provide valuable information that is useful for LWR plant life extension. CRIEPI is currently conducting research on many aspects of materials aging of LWR components including irradiation damage. Therefore, ANL and CRIEPI have decided to perform the following joint work, which is of interest to both laboratories and continues the collaborative relationship between the two labs.

The program was initiated in February of 1999. Samples were taken from two separate subassemblies, designated S1951 and S1952. These subassemblies were constructed of 20% cold-worked Type 316 stainless steel. The samples from these subassemblies were irradiated at temperatures from 371-390ºC to doses up to 56 dpa. The examinations in this program included: immersion density, microhardness, microstructure, and tensile properties. The material history, test plan, results of measurements, and discussion of results are included in this report.

1.0 Experiment

The objective of this project was to evaluate the effects of long-term, low-dose neutron exposure on the mechanical properties, density, and the microstructure of 20% cold worked Type 316 stainless steel. The material analyzed in this study came from 1-mm thick subassembly wrappers (hex cans) irradiated in row 8 of the reflector region of EBR-II. The majority of information available on the effect of neutron radiation on 20% cold-worked Type 316 stainless steel came from experiments performed in the driver (fueled) regions of the EBR-II reactor where dose rates are on the order of $1x10^{-6}$ dpa/s (see Figures 1 and 2). The displacement rates in row 8 are about an order of magnitude lower than in the fueled region of the core. This section describes both the irradiation history and the experimental sampling plan for the material analyzed in this study.

1.1 Irradiation History

Experimental samples were taken from two different reflector hex cans removed from EBR-II upon final shutdown. These hex cans were identified as S1951 and S1952. S1951 and S1952 held neutron source tubes. The dimensions of the hex cans are shown in Figure 1. The subassembly history, dose calculations, and temperature calculations are described in the sections below.

1.1.1 Subassembly History

Neutron source tube S1951 was irradiated for 122,000 megawatt-days (MWD) in position 8D6 (row 8) in EBR-II. The dose as a function of axial position for each of the six flats of S1951 is plotted in Figure 3. Neutron source tube S1952 was irradiated for 9525 MWD in position 8A4 (row 8) in EBR-II. The dose as a function of axial position for each of the six flats of S1952 is plotted in Figure 4. The temperatures for S1951 and S1952 are plotted in Figure 5. For this program, samples were chosen from the lower temperature portions of the duct. To be conservative, sample locations were chosen from S1951 using the higher temperature run 139A data.

1.1.2 Dose Calculations

Neutronic analysis of the EBR-II hex duct irradiation environment was conducted using the two-dimensional solver routines in the transport code DANTSYS. All of the calculations used ENDF/B-V cross sections in a 28-energy group structure and radius-axial (R-Z) geometry. The cross sections were collapsed using weighting fluxes appropriate for the specific regions within the EBR-II core (i.e., fueled core region, reflector, and blanket). Twenty-eight group damage cross-sections were collapsed from ENDF/B-VI data using the cross-section processing code NJOY. The displacement per atom (dpa) values were calculated by multiplying the calculated neutron fluence by the ENDF/B-VI damage cross sections. For each subassembly, the dose was not calculated for every reactor run, but was calculated for periods in which the overall core configuration was relatively stable. For S1951, the core configurations for reactor run 139A and 165A were chosen as representative. For S1952, the core configuration for reactor run 165A was chosen as representative.

1.1.3 Temperature Calculations

Duct temperatures for the two subassemblies (S1951 and S1952) have been calculated as a function of time and position in the EBR-II outer blanket. The calculated temperatures are the azimuthal mean duct temperatures as a function of axial distance from the reactor core centerline. The duct temperature calculation accounted for local power and flow in the subassembly and intersubassembly heat transfer between the subassembly and the six surrounding subassemblies.

The temperature estimates are based upon calculations performed using the SUPERENERGY-2 computer code [1-2]. A direct calculation was performed for EBR-II run 165A using an archived reference input deck. The archived SUPERENERGY-2 input deck was changed to provide a better estimate of the subassembly flow for subassemblies as discussed below. The power generation in each subassembly varied with irradiation time and reactor grid location. Since the SUPERENERGY-2 calculation was only for EBR-II run 165A, further calculations were required to extrapolate the subassembly temperatures to other reactor runs and subassembly locations and thus provide an estimated temperature history for each subassembly. The procedure used for this extrapolation is also presented below.

Meneghetti [3] compared calculated and measured temperatures in reflector subassemblies and concluded that the reflectors are either over-cooled or under-powered relative to the flows and powers used in the calculations. He concluded that flow in the reflector subassemblies would need to be approximately 75% higher to obtain agreement between the calculated and measured temperatures. Koenig [4] concluded that if high reflector flow were the primary cause for the apparent low reflector temperatures it is likely due to the flow split between the reflector and blanket subassemblies. A flow reduction of 16% in the blanket subassemblies would be required to increase the flow rate of the reflectors by 75%.

The low power in the reflector subassemblies causes the duct wall temperature to be nearly equal to the fluid temperature so it is necessary to correct the subassembly flows. In addition, the heat received by intersubassembly heat transfer to a reflector is two to three times larger than the heat generation within the subassembly. It is, thus, important to also correct for flow errors in the subassemblies adjacent to the reflectors. For the final SUPERENERGY-2 calculation, the flow in the two reflector subassemblies was increased by 75% as suggested by Meneghetti. In addition, the flow in each of the six subassemblies adjacent to each subassembly was increased by 75% if it was a reflector and decreased by 16% if it was a blanket subassembly. The calculated duct temperatures are, thus, corrected for the assumed error in the calculated reflector flow rates. Although subassemblies S1951 and S1952 were neutron source tubes instead of reflectors, they were located in row 9, surrounded by reflector subassemblies. Therefore, the temperature calculations were performed as if they were reflectors.

The SUPERENERGY-2 calculation gives a snapshot of the SURV subassemblies duct temperatures during EBR-II run 165A. It is necessary to estimate the duct temperatures at enough points in their lifetimes to indicate the extent to which the subassembly duct temperatures changed as the irradiation time increased. The ideal way to accomplish this would be to perform multiple SUPERENERGY-2 calculations. This, however, would be quite time consuming because of the large amount of effort required to create the SUPERENERGY-2 code

input for additional EBR-II runs. The irradiation history of each of the subassemblies was examined and several reactor runs were identified which when analyzed would provide a reasonable approximation of the subassembly temperature as a function of time and temperature. Table 1 summarizes the history of each subassembly and the reactor runs for which temperature was calculated.

Table 1. Subassembly History for Temperature Calculations

Subassembly	Grid Position	Total MWD in Grid Position	Runs Considered for Temperature Estimates
S1951	8D6	122000	139A, 165A
S1952	8A4	9525	166A

A method was developed to extrapolate the results from the run 165A analysis to other reactor runs and subassembly grid positions. Examination of the SUPERENERGY-2 results for run 165A revealed that because of the low power generation in reflector subassemblies, the duct wall temperatures are approximately equal to the fluid temperature in the subassembly. In addition, 30% to 70% of the heat transfer to the subassembly fluid is due to intersubassembly heat transfer. The extrapolation was, thus, based upon the power generated in the subject subassembly and that in the surrounding six subassemblies.

The total subassembly heat gain, G, is the sum of the power generated in the subassembly and the net heat to the subassembly due to intersubassembly heat transfer as given by:

$$G = P + P_{HT} \tag{1}$$

where P is the subassembly power generation
P_{HT} is the net heat transfer due to inter-subassembly heat transfer.

The intersubassembly heat transfer is assumed to be directly proportional to the average power of the six surrounding subassemblies. The subassembly power and the power in the six surrounding subassemblies can be obtained from the EBR-II run files.

The fluid temperature rise in a subassembly can be calculated from a thermal energy balance as:

$$\Delta T = \frac{G}{wc_p} \tag{2}$$

where G is the total heat gained by the fluid
c_p is the fluid specific heat
w is the subassembly fluid mass flow rate
ΔT is the subassembly temperature rise.

The fluid temperature rise for subassemblies in runs other than 165A can be calculated from the known value of ΔT from run 165A and with a constant specific heat as:

$$\frac{\Delta T_2}{\Delta T} = \frac{G_2}{G}\frac{w}{w_2} \tag{3}$$

where the subscripted and un-subscripted values are the extrapolated and the known (run 165A) value respectively.

Assuming the intersubassembly heat transfer to be directly proportional to the average power of the six surrounding subassemblies the total heat gain in the extrapolated subassembly is:

$$G_2 = P_2 + \frac{P_{av_2}}{P_{av}} P_{HT} \tag{4}$$

where P is the subassembly power and Pav is the average power in the six surrounding subassemblies.

Or for P_{HT}=G-P :

$$G_2 = P_2 + \frac{P_{av_2}}{P_{av}} (G - P) \tag{5}$$

The EBR-II reactor operated at a constant core temperature rise. The total reactor flow was, thus, directly proportional to total reactor power and we can write:

$$\frac{w}{w_2} = \frac{\text{Power}}{\text{Power}_2} \tag{6}$$

where Power is the reactor power during run 165A.
Power_2 is the reactor power during the extrapolated run.

The EBR-II run files were used to obtain the subassembly power and the power in the surrounding subassemblies for each of the runs in Table 1. Flow corrections were made to the input file for SUPERENERGY-2 for the run 165A calculation. The calculation provided a set of reference duct wall temperatures at selected axial positions and the value of G for each subassembly. With this known information an EXCEL spreadsheet was used to solve equations 3, 4, and 5 for the desired duct wall temperatures as a function of time and position. The variation in flat temperatures is always within 5°C of the average for the axial location. Thus, no attempt was made to calculate temperatures for specific flats.

1.2 Sample Selection

Seven types of analysis were performed in this study: tensile, fractography, hardness, density, microstructure, grain boundary segregation, and annealing. For each analysis, a description of the number of samples, sample doses and temperatures, and the reason for performing the test is provided.

1.2.1 Tensile Tests

4 conditions, 8 samples.
Damage : 1, 20, 30, 47 dpa.
Test Temperature : 370º C.
Strain Rate : 4×10^{-5} s^{-1}
Two samples at the each damage level were tested.

To investigate the relationship between mechanical properties and damage, we performed tensile tests at approximately the temperature of irradiation, 370º C. At this temperature, the yield stress is expected to increase up to 20 dpa and then be almost constant beyond 20 dpa [5]. These tests are valuable because tensile properties of highly damaged specimens, irradiated for a relatively long period at low dose rate, are limited. Damage levels of 1, 20, 30 and 47 dpa were selected. A specimen of 55 dpa was not tested because samples with irradiation temperatures of <390°C were desired for this test program and the 55 dpa position had a temperature greater than 390°C. To compare the results to those in Reference [6], the strain rate used for Reference [6] was chosen for this study.

1.2.2 Fractography

2 samples.
Damage : 30, 45 dpa.

Fractography was performed to determine if the highly damaged specimens might be brittle and show transgranular fracture. To investigate the fracture mode, the fracture surface of the tensile test specimens irradiated up to 30 and 45 dpa were examined.

1.2.3 Hardness Tests

8 conditions, 8 samples.
Damage: 1, 2, 10, 15, 20, 25, 30, 56 dpa.
Test temperature: 370º C.
In each sample 4 indents were performed.

To investigate the relationship between yield stress and damage, hardness tests were performed. In general, yield stress should correlate with the hardness. To interpolate the yield stress data obtained from tensile tests, a wide variety of damage conditions was selected. The tests were performed at room temperature and at approximately the temperature of irradiation, 370º C.

1.2.4 Density Measurements

8 conditions, 8 samples.
Damage: 1, 2, 10, 15, 20, 25, 30, 56 dpa.
Test temperature: Room temperature.

To investigate swelling, density measurements were performed. The swelling results are discussed in relation to the results of mechanical property tests and transmission electron microscopy (TEM) observations. Eight damage conditions were selected to correspond with the damage conditions of each tensile test except 47 dpa.

1.2.5 Microstructure and Grain Boundary Chemical Segregation

3 samples.
Damage : 1, 20, 30 dpa.

Microstructure and radiation-induced segregation at grain boundaries should affect mechanical properties. Specimens irradiated to the same damage level as some of the tensile test specimens were selected for TEM observation and grain boundary analysis. From the microstructure, dislocation density and size distribution of voids or bubbles was evaluated. Precipitates were identified and analyzed, including determination of the size distribution of the precipitates. Measurements of grain boundary chemistry distribution were performed at a spacing of 2 nm for twenty points across the grain boundary (approximately 10 nm on each side of the boundary).

1.2.6 Annealing

2 samples.
Damage : 1, 30 dpa.

To investigate effects of welding on microstructure of reactor structural material and microstructural evolution during the hardness and tensile tests, annealing tests were performed in TEM using a heating specimen holder. The plan was for specimens to be annealed for 1 hour at 370º C, 450º C, 500º C, 550º C, 600º C, 650º C, 700º C and 750º C. Because of sample damage at higher temperatures, some higher temperature anneals were not performed. After each annealing step, microphotographs were taken. The microstructure was observed after cooling down the specimens to room temperature. From the microstructure, dislocation density dislocation loop size distribution, and void size distribution was evaluated. Precipitates were identified and analyzed where they existed.

2.0 Results and Discussion

In the following section, the results and discussion for each type of analysis performed in this study (tensile, fractography, hardness, density, microstructure, annealing, and grain boundary segregation) are provided.

2.1 Tensile Properties

In this study, the tensile properties were measured on samples taken from hexagonal cans that were irradiated in row 8 of EBR-II. The results will be reported and compared to the results of samples irradiated in row 2 and reported by Fish et al [6].

2.1.1 Row 8 Tensile Properties

Eight rectangular coupons were prepared by milling from the two hex cans at selected locations. This work was performed at the Hot Fuel Examination Facility at ANL-W. Table 2 shows the sampling locations and irradiation conditions of the eight specimens. The coupons were then machined into test specimens using a traveling-wire electric discharge machine in the Irradiated Materials Laboratory at ANL-E. The design of the tensile specimen, shown in Figure 6, conforms to both the ASTM-E8 and the Japan Industrial Standard (JIS) specifications for tensile testing. The overall specimen length is 60 mm, with a gauge length of 19 mm and a gauge width of 3.0 mm. The thickness of the specimens is 1.0 mm, corresponding to the thickness of the reflector hex cans.

Figure 7 shows the traveling-wire electric discharge machine (EDM). The width and thickness of each machined specimen were confirmed with a micrometer. The appearance of a representative specimen before and after the EDM cutting is shown in Figure 8.

Table 2. Sampling Locations and Irradiation Conditions of Tensile Test Specimens

Specimen	Reflector Subassembly	Flat No.	Distance[(1)] (mm)	Damage (dpa)	Damage Rate ($x10^{-7}$ dpa/s)	Irr. Temp. (°C)
S1T1	U1951	3	472	20	1.2	375
S1T2	U1951	6	472	20	1.2	375
S1T3	U1951	1	521	30	1.8	376
S1T4	U1951	3	541	30	1.8	376
S1T5	U1951	3	655	47	2.8	385
S1T6	U1951	6	655	47	2.8	385
S2T1	U1952	3	401	1	0.76	371
S2T2	U1952	6	401	1	0.76	371

(1) Measured from the bottom of the hex can. The "core" of EBR-II extends from 588 to 932 mm.

A screw-drive Instron tensile-testing machine was used. Both the crosshead displacement and speed were verified before the tests. These verifications are important because the crosshead

displacement was used to determine gauge deformation. (Due to hot-cell constraints, no attached extensometers were used.) The response of the load cell was also verified before the tests. As the tensile tester has a stiff frame relative to the specimen's size, frame relaxation during test was minimal. Figure 9 shows the load frame in the hot cell.

A set of grips that utilize serrated jaws in addition to clevis pins for gripping the tensile specimens was used. The design allowed the specimen to be mounted onto the grips on a tabletop before transfer to the load frame to reduce the risk of dropping the specimen during remote loading. Transferring the mounted specimen/grips assembly to the load frame was performed with a holder equipped with a pair of electromagnets. The electromagnets, when energized, firmly lock on both grip sections, allowing the assembly to be moved as a unit to avoid damaging the specimen gauge.

The specimen temperature for all tests was 370°C. This temperature was achieved with a resistance furnace installed on the tensile machine. To avoid affecting the specimen with a welded thermocouple, thermocouples mounted on the specimen grip and furnace were used to infer the gauge temperature. Prior thermal benchmark tests established the relationship between the grip and gauge temperatures. Because both the test temperature and duration were modest, no inert-gas atmospheric protection was employed. The target test temperature was typically reached in approximately 120 minutes after the start.

To form a direct comparison with a prior study [6] on irradiated 20% cold-worked Type 316 stainless steel irradiated at higher dose rate, the strain rate for the present tests was 4×10^{-5}/s, the same as the prior study. The required crosshead speed (0.456 mm/min for the 19-mm gauge) was verified in a number of trial runs.

The engineering stress-strain plots for the 8 tests are included in Appendix A. From the data, 0.2% offset yield strength, ultimate tensile strength, uniform elongation and total elongation were derived. Table 3 shows the summary results from the 8 tests. The method of deriving these four quantities is illustrated in Figure 10 for sample S1T1.

Table 3. Summary Engineering Tensile Properties[(1)] for the Eight Tests[(2)]

Specimen	Damage (dpa)	Damage Rate ($\times 10^{-7}$ dpa/s)	Test Temp. (°C)	YS (MPa)	UTS (MPa)	UE (%)	TE (%)
S2T1	1	0.76	370	511	628	10.2	16.5
S2T2	1	0.76	370	473	597	12.0	15.4
S1T1	20	1.2	370	677	810	2.9	5.3
S1T2	20	1.2	370	680	824	3.5	6.6
S1T3	30	1.8	370	767	805	2.3	4.8
S1T4	30	1.8	370	676	805	2.3	5.1
S1T5	47	2.8	370	741	790	0.9	2.8
S1T6	47	2.8	370	770	787	0.5	1.9

(1) YS: 0.2% offset yield strength; UTS: ultimate tensile strength; UE: uniform elongation; and TE: total elongation.
(2) All tests were conducted at a strain rate of 4×10^{-5}/s.

Figure 11 displays the measured yield and ultimate tensile strengths from the 8 tests as a function of dose. The strength increases with irradiation with the ultimate tensile strength reaching

approximately 800 MPa at approximately 20 dpa. Beyond that, hardening appears to be saturated. The yield strength curve also increases with increasing irradiation dose. The narrowing separation between the UTS and YS curves at higher dose suggests the work-hardening capability of the material is decreasing with increasing dose.

Ductility of the specimens is shown as a function of dose in Figure 12. Consistent with the strength data, both the uniform elongation and total elongation decrease with dose in relationship to irradiation hardening. Unlike the strength data, however, ductility reduction showed no signs of abating at approximately 20 dpa. While the material retained respectable ductility at approximately 20 dpa, the uniform and total elongations decreased to <1 and 3%, respectively, at 47 dpa.

2.1.2 20% Cold-worked Type 316 Stainless Steel from Fish et al.

The tensile properties for the samples tested in this study can be compared to those of 20% CW Type 316 stainless steel irradiated in the high dose rate regions of EBR-II. Fish et al., measured the tensile properties of 20% CW Type 316 irradiated in row 2 of EBR-II [6-8]. Table 4 lists the tensile properties, fluence, and approximate dose for the samples from the Fish et al. study. The reported fluences were converted to doses using 1.5×10^{21} n/cm^2=1 dpa. This conversion is consistent with the dose/fluence calculations for the samples reported in section 2.1.1. As pointed out in Section 1.0, the dose rate in row 2 is approximately an order of magnitude larger than that of row 8.

Table 4. Tensile Properties of 20% CW Type 316 Stainless Steel, Row 2 of EBR-II [6-8]

Fluence (E>0.1 MeV, 10^{22} n/cm^2)	Approxi-mate dose (dpa)	Irrad. temp (°C)	Test Temp (°C)	YS (MPa)	UTS (MPa)	Uniform Elon-gation (%)	Total Elon-gation (%)
0.0	0.0	371	371	575	710	7.8	9.7
0.9	6.1	371	371	678	792	10.7	12.8
1.5	10.1	371	371	765	847	4.3	6.0
2.0	13.5	371	371	823	891	4.5	6.4
3.0	20.3	371	379	836	891	3.0	4.8
3.5	23.6	371	371	805	867	2.1	3.7
6.0	40.5	388	371	888	938	1.5	2.0
8.1	54.7	377	371	854	906	1.3	2.7

2.1.3 Effect of Irradiation Conditions on Tensile Properties

Few studies have attempted to determine the effect of dose rate on mechanical properties. Brager et al. examined the effect of displacement rate on tensile properties of annealed Type 316 stainless steel [9]. For samples irradiated from 371-424°C with a dose rate range of $0.8\text{-}8.4 \times 10^{-7}$

dpa/s and tensile tested at 385°C, no effect of dose rate on yield strength was noted. For samples examined in the TEM, microstructural features were significantly different between samples irradiated at $1.0x10^{-7}$ and $8.4x10^{-7}$ dpa/s to 3.3 dpa. The higher dose rate samples had a larger precipitate density while the lower rate samples had a higher void density. In the same study, an effect of dose rate on yield strength was noted for Type 304 stainless steel. Brager concluded that the lack of effect of dose rate on yield strength of Type 316 was a "fortuitous situation in which a loss in strength contribution from precipitates as the displacement rate is decreased is offset by a concurrent gain in the strength contribution from the voids."

A French study on solution-annealed Type 316 stainless steel fuel cladding irradiated in the Rapsodie and Phenix reactors indicated that the saturation yield stress was greater in material irradiated in Phenix. The material irradiated in Phenix was irradiated at twice the dose rate of material irradiated in Rapsodie [10].

The effect of dose rate on mechanical properties can be examined by comparing the data from this study to the data from the work of Fish et al. The irradiation temperatures and doses are similar for the samples irradiated in row 8 in this study and the samples irradiated in row 2 in the Fish study, but the dose rate differs by an order of magnitude. A comparison of the row 8 to row 2 tensile property data may elucidate the effect of dose rate on the tensile properties.

The row 8 yield strength data is compared to the row 2 tensile data in Figure 13. The comparison of yield strength indicates that, even though both sets of data come from nominally 20% cold-worked Type 316 stainless steel, the row 8 material has a yield strength at 1 dpa lower than the row 2 material at 1 dpa. The yield strength increases similarly as a function of dose for both sets of data beyond 1 dpa. The lower yield strength at 1 dpa in the row 8 samples could come from two sources. First, at the low dose rate of the row 8 samples, a significant portion of the dislocation network may have annealed out between 0 and 1 dpa. At the low temperature of 370ºC, this annealing is not expected. As will be noted in section 2.5, the dislocation density in the row 8 samples after 1 dpa is consistent with other studies of 20% cold-worked Type 316.

Alternately, the material irradiated in row 8 may have had lower yield and ultimate tensile strengths in the unirradiated state than the row 2 material. Because these ducts underwent standard quality assurance procedures prior to going into the reactor, the cold-work is not likely to differ significantly from the goal of 20%. The ducts from this study and that of Fish came from different lots of steel and the compositional differences may have caused a difference in yield and ultimate tensile strength. Table 5 compares the 1 dpa yield strength from three different experiments, the 20% cold-worked material irradiated in row 8 of EBR-II in this study, the 20% cold-worked material irradiated in row 2 of EBR-II in the Fish study, and 12% cold-worked material irradiated in row 9 of EBR-II [11]. The difference between the largest and smallest yield strength in Table 5 is about 80 MPa. Carson et al., measured the hardness at room temperature of Type 316 stainless steel as a function of cold-work [12] for various lots of material. For the material measured in Carson's study, the concentration of Cr varied from 16-18, Ni from 12-14, Fe from 64-69, and Mo from 2-3 wt%. For 12% cold-work, the room temperature hardness ranged from about 235-285 HV. Using the hardness-yield strength correlation developed by Higgy and Hammad [13], $\Delta\sigma_y=3.27\Delta H_v$ to convert the hardness data of Carson et al. to yield strength, the range of yield strength as a function of composition for 12% cold-work is about 164 MPa. At 20% cold-work, the range of hardness converts to a range in

yield strength of about 195 MPa. The difference in yield strengths noted in Table 5 is bounded by the hardness measured by Carson. Because of the large variability of strength with composition, a direct comparison of yield strength as a function of dose between the row 2 and row 8 results cannot indicate if the irradiation dose rate has a significant effect on tensile properties.

Table 5. Yield Strength for Various Cold-work Conditions

Cold-work/Irradiation Position	Yield Strength (370ºC) at low dpa (MPa)
12% Row 9	~580 (1 dpa)
20% Row 8	~500 (1 dpa)
20% Row 2	~575 (0 dpa)

The uniform elongation as a function of dose for the row 8 and row 2 samples is plotted in Figure 14. No significant difference in the uniform elongation is noted between the two data sets.

During irradiation at all reasonable irradiation temperatures, stainless steels harden compared to the solution annealed state, with the yield strength approaching the ultimate tensile strength and the uniform elongation decreasing. Lucas [14] has noted the following relationship between uniform elongation, yield strength, and ultimate tensile strength:

$$\varepsilon_u = 0.5\left(1 - \frac{\sigma_y}{\sigma_u}\right) \tag{7}$$

As the yield strength approaches the ultimate tensile strength, the uniform elongation decreases. Figures 15 and 16 plot the uniform elongation versus $\left(1 - \frac{\sigma_y}{\sigma_u}\right)$ for the row 8 and row 2 data, respectively. In both cases, within the 95% band of uncertainty, the uniform elongation follows the relationship of equation 7. Figure 17 displays the hardening as a function of dose. The higher dose rate row 2 samples lose work hardening capability faster with increasing dose than the lower dose rate row 8 samples, even though there was no significant difference in the uniform elongation. Although no microstructural or fractography data is available from the Fish study, the loss of work hardening capacity may correspond with establishment of dislocation channeling as the primary deformation mechanism. If dislocations are free to travel through the material in slip bands, then less work hardening will occur.

The comparison of the strength and elongation of 20% cold-worked Type 316 stainless steel irradiated at different dose rates in EBR-II indicate the following:

- The row 8 samples have lower yield strength at 1 dpa than the row 2 samples. This difference is likely to be caused by compositional differences between the lots of Type 316 used in each study.
- No significant difference in uniform elongation is seen between the row 8 and row 2 samples.

- The higher dose rate row 2 samples lose work hardening capability faster than the lower dose rate row 8 samples. This may indicate that the deformation mode is dominated by dislocation channeling. This difference could be caused by either compositional differences or dose rate differences.

2.2 Fractography

Posttest fractography was performed on two representative samples, S1T4 (30 dpa) and S1T5 (47 dpa), to elucidate fracture modes. The examination was performed with a scanning electron microscope.

Frontal and side views of the fracture of the 30-dpa S1T4 specimen are shown in top picture of Figure 18. Necking of the gauge section of this specimen is evident. For the higher-dose S1T5 specimen, however, necking is almost imperceptible, as shown in the bottom picture of Figure 18. This contrasting behavior is consistent with the measured elongation data, which showed further reduction of ductility during irradiation from 30 to 47 dpa. Because necking constitutes a sizable fraction of the gauge deformation after the maximum load (uniform elongation) is attained before fracture, it reflects to a large extent the difference between the uniform and total elongation. In this respect, the differences of 2.8% for the 30-dpa S1T4 and 1.9% for the 47-dpa S1T5 appear to be consistent with the observed necking behavior.

Fracture in the 30 dpa specimen is mainly ductile but with local regions of mixed-mode failure. The ductile fracture, illustrated in Figure 19, consists mainly of dimples and microvoids. Among the dimples, there are facet features that suggest flow localization and slip band decohesion. Figure 20 shows one of the few areas on the 30 dpa specimen with mixed mode fracture - the brittle failure appears as a transgranular shear along active slip planes. The side surface of the S1T4 specimens, Figure 21 shows steps from the tensile deformation; such features are typically associated with dislocation channeling.

The fracture surface of the higher-exposure 47 dpa specimen displays significantly more brittle features, as shown in Figure 22. The fracture consists mainly of small facets and slip bands that suggest channel fracture. Dimples and microvoids are far less abundant than in the lower-exposure S1T4 specimen. Noticeable steps are also found on the side surfaces of the specimens, Figure 23. Recall from Figure 17 that at the higher doses, the hardening $\left(1-\frac{\sigma_y}{\sigma_u}\right)$ is similar between the row 2 and row 8 samples. In each case, the deformation may be dominated by channel fracture along slip bands.

2.3 Microhardness

To study the mechanical property changes of 20% cold-worked Type 316 stainless steel irradiated at low dose rate, Vickers hardness was measured using a Nikon QM hardness tester on eight samples taken from reflector hex cans retrieved from EBR-II. Each sample consists of a 3 mm disk punched from a subassembly hex can. Samples were punched from two different subassemblies, S1951 and S1952. The hardness of each of the sample was measured at 25°C and at 370°C. Four indents were made on each sample. The indents were made with a 1000g load.

Tables 6 and 7 list the hardness measurements of samples from reflectors S1951 and S1952. Also listed are the punching location, core position, temperature, dose, and dose rate for each sample.

Table 6. Hardness for Samples from Hex Can S1951

Sample ID	Flat	Distance from Core Centerline (cm)	Temperature (°C)	Dose (dpa)	Dose Rate (dpa/s)	Vickers Hardness (HV) 25°C	Vickers Hardness (HV) 370°C
S1P1	1	-42.9	373	10	5.9E-08	330±17	245±12
S1P2	1	-35.8	374	15	8.9E-08	341±20	267±12
S1P3	1	-31.3	375	20	1.2E-07	357±21	273±14
S1P4	1	-27.8	376	25	1.5E-07	367±20	277±15
S1P5	5	-21.7	379	30	1.8E-07	362±19	277±13
S1P6	1	-10.3	385	56	3.3E-07	356±21	260±13

Table 7. Hardness for Samples from Hex Can S1952

Sample ID	Flat	Distance from Core Centerline (cm)	Temperature (°C)	Dose (dpa)	Dose Rate (dpa/s)	Vickers Hardness (HV) 25°C	Vickers Hardness (HV) 370°C
S2P1	4	-36.5	373	1	7.6E-08	257±13	197±9
S2P2	4	-25.8	375	2	1.5E-07	294±14	199±9

Figure 24 plots the hardness as function of dose. The hardness reaches its maximum value by around 25 dpa for the room temperature tests and by around 15 dpa for the 370°C tests. Figure 25 compares the 370°C hardness tests from S1951 and S1952 to the yield strength. The increase in hardness and yield strength appear to occur roughly over the same range of dose.

2.4 Immersion Density

To determine the swelling characteristics of 20% cold-worked Type 316 stainless steel irradiated at low dose rate, immersion density was measured on eight samples taken from reflector hex cans retrieved from EBR-II. Each sample consists of a 19mm disk milled from a reflector hex can. Samples were produced from two different reflectors, S1951 and S1952. The density of each of the samples was measured five separate times.

Tables 8 and 9 list the density measurements of samples from subassemblies S1951 and S1952. Also listed are the punching location, temperature, dose, and dose rate for each sample. The swelling listed in Tables 8 and 9 assumes an unirradiated density of 7.96 g/cm^3. The calculated swelling as a function of assumed unirradiated density is discussed later in this section.

Table 8. Density for Samples from Hex Can S1951

Sample ID	Flat	Distance from Core Centerline (cm)	Temperature (°C)	Dose (dpa)	Dose Rate (dpa/s)	Density (g/cm^3)[1]	Swelling (%) ($\rho_{unirrad}$=7.96 g/cm^3)
S1P1	1	-42.9	373	10	5.9E-08	7.8694±0.0150	1.14
S1P2	1	-35.8	374	15	8.9E-08	7.8915±0.0350	0.86
S1P3	1	-31.3	375	20	1.2E-07	7.9274±0.0150	0.41
S1P4	1	-27.8	376	25	1.5E-07	7.8906±0.0410	0.87
S1P5	5	-21.7	379	30	1.8E-07	7.8751±0.0200	1.07
S1P6	1	-10.3	385	56	3.3E-07	7.7529±0.0280	2.60

[1]Uncertainty is the standard deviation of the multiple density measurements

Table 9. Density for Samples from Hex Can S1952

Sample ID	Flat	Distance from Core Centerline (cm)	Temperature (°C)	Dose (dpa)	Dose Rate (dpa/s)	Density (g/cm^3)[1]	Swelling (%) ($\rho_{unirrad}$=7.96 g/cm^3)
S2P1	4	-36.5	373	1	7.6E-08	7.9054±0.0140	0.69
S2P2	4	-25.8	375	2	1.5E-07	7.9304±0.0140	0.37

[1]Uncertainty is the standard deviation of the multiple density measurements

Because of the unexpected large scatter in the density measurements in some of the samples (typical scatter in these types of density measurements is ≤ 0.02 g/cm^3), the density of three of these samples (S1P1, S1P2, and S1P4) was re-measured following thinning and punching of 3mm disks. The re-measured densities are listed in Table 10 along with the measurement on the original 3/4-inch punch. The uncertainties in the densities are much greater in the thinner, punched samples. Because the accuracy of the density measurements is far worse after thinning, the other 5 samples were not re-measured and the original density measurements were used in the analysis.

Table 10. Density from Re-measured Samples

Sample ID	Density of 3/4 inch punch (g/cm^3)[1]	Density of polished and thinned 3/4-inch punch (g/cm^3)[1]
S1P1	7.8694±0.0150	8.0954±0.1150
S1P2	7.8915±0.0350	8.1507±0.2120
S1P4	7.8906±0.0410	8.3444±0.0720

[1]Uncertainty is the standard deviation of the multiple density measurements

Archive material for these reflectors is not available for density measurement. To estimate the swelling, we can use the nominal non-irradiated density for 20% cold-worked Type 316 stainless steel, which ranges from 7.96-7.99 g/cm^3 or we can use the 1 and 2 dpa values since little swelling is expected at these low doses. Table 11 indicates the calculated swelling using 7.91 (corresponding to the 1 dpa sample) and 7.96 g/cm^3.

Table 11. Swelling Values Assuming Various Values of Unirradiated Density

Sample ID	Temperature (°C)	Dose (dpa)	Dose Rate (dpa/s)	Swelling (%) ($\rho_{unirrad}$=7.91 g/cm^3)	Swelling (%) ($\rho_{unirrad}$=7.96 g/cm^3)
S2P1	373	1	7.6E-08	0.00±0.18	0.69±0.18
S2P2	375	2	1.5E-07	-0.32±0.18	0.37±0.18
S1P1	373	10	5.9E-08	0.46±0.19	1.14±0.19
S1P2	374	15	8.9E-08	0.18±0.44	0.86±0.44
S1P3	375	20	1.2E-07	-0.28±0.19	0.41±0.19
S1P4	376	25	1.5E-07	0.19±0.52	0.87±0.52
S1P5	379	30	1.8E-07	0.38±0.25	1.07±0.25
S1P6	385	56	3.3E-07	1.93±0.35	2.60±0.35

[1]Uncertainty is the standard deviation of the multiple density measurements

Figure 26 plots the swelling as function of dose for using both 7.91 and 7.96 g/cm^3 as the unirradiated density. Using 7.96 g/cm^3 as the unirradiated density, at 56 dpa the swelling reaches 2.6%. The curve in Figure 26 is the best fit second-order polynomial to the swelling measurements. Using 7.96 g/cm^3 , the extrapolated swelling at 100 dpa is 7.5%. Also plotted is the swelling equation for 20% cold-worked Type 316 stainless steel determined in the U.S. fast reactor cladding development program [15]. The equation takes the form:

$$\text{Swelling}(\%) = 0.01R\left\{\phi t + \frac{1}{\alpha}\left[\ln\left(\frac{1+\exp\left[\alpha(\tau-\phi t)\right]}{1+\exp(\alpha\tau)}\right)\right]\right\} \quad (8)$$

The data from this study indicates greater swelling at high dose than the swelling model predicts, regardless of the assumed value of the density in the unirradiated condition. Three things could contribute to the greater swelling in this study: differences in cold-work, differences in swelling due to differences in bulk composition, or differences in swelling due to the displacement rate.

The swelling difference is unlikely to be caused by cold-work. The quality assurance requirements associated with reactor ducts would ensure that the cold-work was per specification and 20% cold-worked ducts in row 2 and 8 would have similar dislocation densities in the unirradiated state. As discussed in section 2.2.3, the differences in unirradiated strength are likely to be caused by differences in composition.

Published data indicates that at a fluence of $10x10^{22}$ n/cm^2 (E>0.1MeV), differences in composition can change the swelling by a factor of three [15]. At the highest dose in this study (56 dpa), the swelling is a factor of three greater than the model predictions. The differences in swelling are consistent with those previously noted to be caused by compositional differences. Comparing the swelling measured in this study to swelling in 12% cold-worked Type 316 stainless steel [16] irradiated in row 9 of EBR-II, the swelling of the 20% cold-worked material is greater, an unexpected result since swelling normally is inhibited by cold-work. Compositional differences between the different lots of the 20% CW material could lead to the greater than expected swelling.

The data used to build equation 8 was built using samples irradiated at higher displacement rates than those used in this study. Although displacement rate has been shown to affect swelling in 304 stainless steel [17], displacement rate has not been shown to significantly affect swelling in Type 316 stainless steel [16]. Although differences in displacement rate may contribute to greater than expected swelling, displacement rate is probably less of a contributor than composition.

2.5 Microstructure

Microstructural analysis for samples irradiated to 1, 20 and 30 dpa was carried out in a JEOL 2010 transmission electron microscope (TEM) equipped with an energy dispersive x-ray detector and a scanning transmission electron detector attachment. The microscope was operated at an accelerating voltage of 200 kV. The following sections will describe the analysis techniques used and detail the experimental results.

2.5.1 Microstructural Analysis Procedure

Several 3 mm TEM discs were punched from each of the 1.9 cm density discs. The discs were punched using a custom disc-punch located inside the Hot Fuel Examination Facility (HFEF) hot cell. The TEM discs were then ground out of cell to approximately 150 microns thick and thinned to electron transparency using either a Taylor Engineering twin jet electropolisher or a South Bay Technology single jet electropolisher (flipping the sample half way through polishing). The electrolyte used was a solution of 95% methanol/ 5% perchloric acid at polishing temperatures between -45^{o} and $-30°C$. The measured radioactivity of the electropolished TEM disks ranged between approximately 10 and 200 mr/hr β/γ, a level which allowed routine radiological handling of the samples.

To perform defect density measurements, it was necessary to determine sample thickness in the analysis regions. This was accomplished using convergent beam electron diffraction (CBED) with an electron probe size on the order of 10 to 15 nm. Pixel intensity profiles across the scanned CBED disk image were used to measure fringe spacing. The spacings were then converted to a thickness value as described in Reference [18]. An example of the Excel® spreadsheet developed to make these calculations is shown in Figure 27. Both magnification and camera length were calibrated on the TEM prior to making quantitative measurements.

Microstructural analysis was carried out in 2 or 3 grains, analyzing several fields of view in each grain. Void number densities were counted using a freeware image analysis program entitled

NIH image. Void diameters were also measured in several regions to determine the void size distribution. In taking images of the voids, a large deviation from the Bragg condition was used in order to minimize contrast from the dislocation structure.

Because of the high density of radiation-produced defects, details of the dislocation structure could not be discerned under bright-field (BF) imaging conditions, therefore, weak-beam darkfield (WBDF) imaging conditions were used. Under WBDF, imaging with a <111> type g vector reveals all of the variants of the Frank loops while 3 of the 6 variants of the perfect dislocations are visible. Loop sizes and densities were measured using procedures similar to those used in measuring the void size distributions. Measurements of loops less then 5 nm although included, are subject to greater error than those on larger loops due to complexities arising from WBDF imaging conditions.

For the network dislocations, the line length per volume (Λ) was determined by measuring the number of dislocations in an area and using the stereological equation developed by Schoeck [19]:

$$\Lambda = 2 * P_A \tag{9}$$

where P_A is the number of intersecting points (dislocations) divided by the area. This value was then multiplied by an additional factor of 2 to take into account the fact that with g_{111} one half of the dislocations will be invisible.

A majority of the precipitate identification was performed using extraction replicas. Many of the grain boundary precipitates could not be extracted, so they were identified in the bulk by electron diffraction. It was not possible to obtain compositional information in the bulk because the high activity of the samples overloaded the energy dispersive x-ray (EDX) detector.

Extraction replicas were prepared by first etching electropolished TEM discs. The etching process dissolved a layer of the austenite matrix, leaving the second phase precipitates in relief on the sample surface. Carbon was then evaporated onto the sample which produced a continuous film overlaying the etched surface. Precipitates protruding from the surface were thus partially embedded within the carbon film. The disc was then etched further until the carbon film with the embedded precipitates floated off. The film was then rinsed in ethanol and collected onto a copper grid. Precipitate identification was performed using techniques of selected area diffraction, microdiffraction and EDX. Precipitate compositions were determined using both conventional TEM using a highly converged electron beam, and with the microscope operating in scanning transmission electron microscopy (STEM) mode.

Identification of the phases was performed using a commercial software package entitled Desktop Microscopist©. A list of phases which have been found in unirradiated and irradiated Type 316 stainless steels was compiled from literature resources. The crystal structures and atomic positions of these phases were then entered into Desktop Microscopist© in order to generate a search database for identifying the possible phases present in the hex ducts. Digitally scanned images of the precipitate electron diffraction patterns were then matched to patterns generated from the entered phases for positive phase identification.

2.5.2 Microstructural Analysis Results

Images of the microstructure of the 1 dpa sample are provided in Figure 28. At this low dose, there appears to be only minor precipitation and no void formation. The network or line dislocation density is estimated to be ~2 x 10^{15} m^{-2}. There was no unirradiated archive material available for TEM examination. The density of network dislocations in the 1 dpa sample was less than that measured in unirradiated 20% CW Type 316 SS alloy by Maziasz et al. and Johnson et al. [20-21]. Johnson et al., note that at elevated temperature the dislocation density quickly reaches a value lower than that of room temperature 20% cold-worked material. At 370°C, the dislocation density is around 3x10^{15} m^{-2}. The difference between the dislocation density measured in this study and that of Johnson are close enough to support a similar amount of cold-work in the two pieces of 20% cold-worked material.

A small population of perfect and faulted loops has also formed at 1 dpa which can be more clearly discerned in the weak-beam dark-field image (WBDF) shown in Figure 28. The loops ranged in size from ~6 nm to ~50 nm with the average loop diameter being ~22 nm. Figure 29 shows the loop diameter distribution for the 1 dpa sample. Faulted loops form from the clustering of interstitial atoms and grow in size with increasing dose. When they reach a critical radius, they tend to unfault and become perfect loops. The perfect loops are mobile on the glide plane and can interact with other dislocations to form dislocation networks.

A few larger (> 100nm) precipitates are scattered randomly throughout the grain interiors, and these were identified as $M_{23}C_6$ and Ti-rich MC in the extraction replicas (Figure 30). Typical compositions of the observed precipitates are listed in Table 12. The grain boundaries in the 1 dpa sample are relatively precipitate free.

Table 12. Typical Precipitate Compositions in the Type 316 SS Hexagonal Duct Material

	Chemical Composition (Wt%)							
Dose	Si	Ti	Cr	Mn	Fe	Ni	Mo	Phase
1 dpa	0.1	0.0	68.5	1.03	16.2	2.2	12.0	$M_{23}C_6$
	0.2	84.2	8.3	0.0	3.4	0.0	4.5	TiC
20 dpa	0.56	0.0	66.36	1.13	15.94	2.68	13.32	$M_{23}C_6$
	8.4	0.0	40.3	1.8	17.2	27.5	4.9	M_6C (η)
30 dpa	1.11	0.0	53.07	1.25	26.92	4.9	12.75	$M_{23}C_6$
	12.92	0.0	36.21	0.77	19.22	27.48	1.66	M_6C (η)

Table 13. Cavity, Precipitate, and Dislocation Data for 20% CW Type 316 SS Hexagona Duct Material

	Voids		Precipitates		Frank Loops		Network Dislocations
Dose	Density, m^{-3}	Diameter, nm (range)	Density, m^{-3}	Diameter, nm (range)	Density, m^{-3}	Diameter, nm (range)	Density, m^{-2}
1 dpa	N/A	N/A	$< 1.0 \times 10^{20}$	> 50	6.0×10^{20}	22(8-51)	1.5×10^{15}
20 dpa	1.2×10^{21}	9.9 (3-26)	3.4×10^{21}	13 (6-33)	3.4×10^{21}	26 (9-48)	2.9×10^{15}
30 dpa	1.0×10^{21}	11.1(2 –22)	7.3×10^{21}	15 (5-53)	2.1×10^{21}	27 (6-54)	2.0×10^{15}

A table of all the measured microstructural data for the 3 samples examined is provided in Table 13. Irradiation to 20 dpa led to the formation of a high density of cavities, dislocations and precipitates. A BF image of the cavity and precipitate structure in the 20 dpa sample is shown in Figure 31 along with a WBDF image that reveals the dislocation microstructure. Void and loop size distribution graphs for the sample are shown in Figure 32. The density of cavities in the 20 dpa sample was on the order of 1.2×10^{21} m^{-3} with an average cavity diameter of 9.9 nm. Faceting of the cavities with increasing size is an indication of a transition from gas stabilized bubbles to vacancy driven void growth [22]. The swelling due to the cavities can be calculated from the density and size parameters using the following equation:

$$\frac{\Delta V}{V} = \frac{(4/3)\pi R^3 N}{1 - (4/3)\pi R^3 N} \tag{10}$$

where R is the void radius and N is the density. From this equation, bulk swelling due to void formation is approximately 0.07% at 20 dpa. The amount of bulk swelling will be different (see section on immersion density measurements) than this value due to the evolving dislocation structure and the formation of the high density the second phase precipitates, however, the low level of void swelling suggests the hex duct material has not yet reached the 1%/dpa steady-state level of swelling commonly cited for austenitic stainless steel [5].

The density of matrix precipitates is about three times that of the voids, and the precipitates range in size from about 5 nm up to 50 nm. The high density of precipitates less than 10 nm in size were identified as M_6C type (Ni and Si rich), while larger precipitates (> 50 nm) were identified as Cr-rich $M_{23}C_6$ type as shown in Figure 30. Additionally, in the both the 20 and 30 dpa samples, a substantial amount of grain boundary precipitation occurred (Figure 33) with many of the boundaries being continuously decorated with $M_{23}C_6$ type carbides. Unlike observations in Type 316 SS irradiated at higher flux and/or higher temperatures, there was no evidence of γ' precipitation in the Type 316 SS hex ducts [23, 24]. Many of the cavities that formed in the material are associated with the precipitates. The development of precipitate cavity associations has been observed in several other studies [19, 25, 26] and has been linked to enhanced nucleation of helium bubbles at the precipitate interface. The density of precipitates doubles from 20 to 30 dpa with the concentration of the precipitates having greater Ni and Fe concentration at the higher dose. Since greater bulk Ni concentration is known to reduce swelling [5] , removing the Ni from the matrix in the form of precipitates should correspond with

greater swelling. As seen in figure 26, the swelling also starts to increase between 20 and 30 dpa.

A representative BF image of the radiation-induced dislocation structure present in 20 dpa sample is shown in Figure 31. Dislocation loops, the majority of which are of the Frank type (1/3 <111>) are seen to populate the microstructure along with a high density of network dislocations. The number density of perfect loops has decreased from what was observed in the 1 dpa sample. The network dislocation density is about a factor of two greater than the 1 dpa sample, suggesting that dislocation loop growth and unfaulting has occurred. Loops diameters range from approximately 6 to 50 nm with the average being around 27 nm.

Further irradiation to 30 dpa did not result in a substantial change of the microstructure (Figure 34). Both the void density and void diameter were similar to the 20 dpa sample as well as the dislocation loop density and diameter as illustrated in the size distribution graphs of Figure 35. The microstructure indicates that the transient regime for swelling extends to a dose greater than 30 dpa, and the increasing precipitate density with dose suggests the changing matrix composition plays an important role in the onset of the 1%/dpa steady-state swelling level.

2.6 Annealing

Two of the Type 316 hexagonal duct TEM samples, irradiated to 1 and 30 dpa (S2T1 and S1T3), were annealed as thin foils in the JEOL 2010 TEM with a Gatan Model 652 heating stage. Initially, an annealing schedule ranging in temperature between 370^{o} and 800°C was chosen with ~50°C temperature increments and an annealing time of 1 hour at each temperature. However, during the experiments it was discovered that at ~550°C what appeared to be sublimation of the sample began to occur at the edge of the thin foil. The sample began to dissipate leaving only a thin transparent film (possibly an oxide). The rate of sublimation increased with increasing temperature and following annealing at 650°C the experiment was halted due to concern over excessively contaminating the interior of the microscope.

After each annealing phase, the sample was cooled to ambient temperature for analysis. Three areas were selected for analysis and the stage position and tilt recorded for each area. Images were taken of the same area and nominally the same tilt following each annealing phase. Because of sample drift and slight sample distortion during heating and cooling, the tilting conditions changed during annealing, and therefore the sample tilt conditions could not be duplicated exactly. For each area, CBED measurements were taken prior to annealing to determine sample thickness. BF images were taken slightly underfocused to analyze changes in the precipitate and void structure, while WBDF images were taken to detail the changes in the dislocation structure.

2.6.1 Annealing Results

1 dpa sample

As mentioned in the earlier section on microstructural analysis, the sample irradiated to 1 dpa had a low density of dislocation loops, no voids and a few scattered precipitates. The annealing tests of the Type 316 SS irradiated to 1dpa were carried out at temperatures of 370°, 450°, 500°,

550°, 600°C for 1 hour and 650°C for 0.5 hours in the TEM. The annealing time at the highest temperature of annealing (650°C) was limited to 0.5 hours to avoid contamination of the TEM due to sublimation was observed at the edge of thin foil sample.

Figure 36 shows the microstructures of the matrix after annealing as a function of annealing temperature. There are populations dislocation networks and loops before annealing. After annealing at 370°C, which corresponds to irradiation temperature, there is no recovery of the dislocation networks and loops. Some recovery of the dislocation can be observed at 500°C, but most of loops do not change up to 550°C. The loops begin to disappear at the temperatures above 600°C. The dislocation density also decreases markedly at 650°C.

Figure 37 shows the microstructures near the grain boundary after annealing as a function of annealing temperature. Some precipitates begin to be generated in the matrix at a temperature of 450°C. However, there are no precipitates and cavities generated on the grain boundary at the temperatures of up to 650°C.

30 dpa sample

For the 30 dpa sample, comparing the microstructure of the unannealed sample and that of the sample annealed at 370°C for 1 hour reveals that no significant change in the cavity and dislocation structure occurs (Figure 38). Further annealing at 450°C for 1 hour led to the formation of small bubbles. Some of these bubbles were observed to form on the grain boundaries (Figure 39). The bubbles on the grain boundaries began to form during annealing at 370°C (below the temperature at which they formed in the matrix) and persisted throughout all of the annealing temperatures. Further annealing at 500, and 550°C led to an increase in the bubble density, but not a substantial increase in size. By 600°C, oxide formation (discussed below) began to obscure the microstructure. Typically, the cavities that existed prior to annealing shrank and became spherical with annealing time and temperature.

Because of changes in sample contrast and difficulty in maintaining identical tilts for subsequent annealing stages, precipitates which look like they have disappeared or formed during annealing, may have just gone in and out of contrast. Careful examination of the micrographs indicates that the precipitates that existed prior to annealing change very little in response to the annealing, although at a temperature of 450°C some of the grain boundary precipitates begin to dissolve (see Figure 39). The images suggest that a few small precipitates begin to form during annealing above 450°C. The small size of the precipitates precluded identification in the bulk sample.

The dislocation loop and network structure appeared to be unchanged following annealing at 370°C (Figure 40). Further annealing at 450°C led to the disappearance of some of the loops, and an increase in the network dislocation density. With each subsequent phase of annealing, a few more of the loops disappeared. After annealing at 550°C all of the loops had disappeared. In general, loop morphology changed very little below the annealing temperature at which they disappeared.

At the same time that sublimation is observed, selected area diffraction patterns show the formation of a polycrystalline ring pattern (Figure 38). A search of the diffraction database nominally identified the pattern as that of δ-Fe_2O_3 (HCP). The pattern persists during higher

temperature annealing, and the ring intensity increases. It appears that at the higher annealing temperatures, the surface contamination leads the formation of polycrystalline iron oxide. Consequently, as observed in the bright field image of Figure 38 taken following annealing at 650°C, the sample appears mottled and the underlying microstructure is obscured. Because of this, although it may seem that the voids in the material have disappeared at this annealing temperature, they may just be obscured by the oxide.

2.6.2 Annealing Discussion

The absence of cavity formation in the 1 dpa sample suggest that the formation of cavities results from precipitation of transmutation-induced helium into bubbles during annealing, rather than precipitation of supersaturated vacancies during the fairly rapid cool down phase of the experiment. Similar formation of bubbles during *in situ* annealing of 304 SS hex ducts has also been observed [27]. In addition, cavities which form during annealing at lower temperatures do not dissolve and re-precipitate during further annealing stages at higher temperature. An increase in cavity density, rather than growth of existing cavities, indicates that the cavities have a critical radius due to internal gas pressure. This critical radius is below that of the pre-existing voids, which tended to shrink during annealing.

Formation of small bubbles following annealing was not observed in several other studies on bulk 304 SS [28-31] and void shrinkage did not occur until higher annealing temperatures (>700°C). Calculations in these earlier studies also revealed that when the voids did shrink, they shrank to the point were the total cavity volume was comparable to the amount of transmutation-induced He [30]. Small bubble nucleation has been observed in irradiated steels with high helium generation rates at lower irradiation temperatures [32]. It is quite likely that there are many existing He-atom clusters prior to annealing, which are too small to observe in the TEM. Upon annealing the existing He bubbles act as sinks for the He in solution and thus they grow to a size observable in the TEM. In addition, the nature of the TEM thin foil may enhance the nucleation of the small He bubbles at the sample surface.

Comparing these results to that of Holmes et. al. [30] on 304 SS reveals that in the Holmes study, there was not a reduction in dislocation loop size or density during annealing for 1 hour at 480°C while in this study loops began to disappear at 450°C after annealing for 1 hour. The reason for the decrease in loop density upon may be due to loop unfaulting and gliding to the foil surface. Surface image effects may accelerate this process. An additional study conducted by Busby [28], indicates that small black spot loops formed by irradiating at lower temperature are also stable (loop density remains unchanged) after 1 hour of annealing at 500°C. In order to clarify the impact of the thin foil on annealing behavior, further studies will have to be performed to compare differences between annealing behavior in bulk samples compared to *in situ* studies with thin foils.

Consequences of the observed microstructural changes to alloy properties may be significant. Because faulted dislocation loops are among the strongest barriers to plastic deformation [19], a reduction in their density should improve alloy ductility. Tensile tests on irradiated and annealed 304 SS [31] indicate that this is true. The impact the formation of a large density of small bubbles has on mechanical properties should be to provide a moderate increase in tensile strength, but studies suggest that small bubbles are much less effective strengtheners than the

larger voids. Overall, one would expect that annealing of irradiated structural materials in this temperature range could provide an improvement in alloy ductility.

2.7 Grain Boundary Segregation

Grain boundary compositions were measured for three irradiation doses, 1, 20, and 30 dpa using the CM200 FEG at Oak Ridge National Laboratory. Details of the analysis and results of the measurements are listed below.

2.7.1 Data Collection

Grain boundary measurements were taken by placing the beam in a position such that portions of the diffraction patterns on both sides of the grain were visible. Characteristic X-rays were counted for fifty seconds of live time.

Grain boundary profiles were taken using the line scan mode with drift correction. Each point in the spectra was measured for twenty seconds of live time. Drift correction was applied for every two points measured. Spectra were taken at a spacing of 2nm for twenty points surrounding the grain boundary.

Prior to calculating the intensity of each x-ray peak, the background counts must be subtracted. For all measured peaks, a linear fit of the background was used for background subtraction. For Cr, Fe, and Ni, a linear fit was used between the background spectra at energies less than the Cr K_α and energies greater than the Ni K_β. For Si and Mo, a linear fit was used between the background spectra at energies less than the Si K_α and energies greater than the Mo K_β.

To compensate for background radiation from the column and for radioactive decay from the samples themselves, a count of the x-rays generated with the electron beam in the sample hole was taken. Prior to calculating concentrations, the "hole count" was subtracted from the acquired spectra. Hole-counts for the grain boundary compensation measurements were 50 seconds long and hole-counts for the grain boundary profiles were 20 seconds. These times correspond with the live time counting intervals for grain boundary measurements and grain boundary profiles respectively.

The intensity of each characteristic x-ray peak was calculated by defining a window around each peak using a 0.3 keV wide band. The peak intensity used in composition calculations is the number of counts in this 0.3 keV window, minus the background and "hole-count" in the region.

Compositions were calculated from intensity spectra using k-factors. The ratio of the concentration of two atoms is proportional to the ratio of the measured intensities, with the proportionality constant known as the k-factor:

$$\frac{C_A}{C_B} = k_{AB}\frac{I_A}{I_B} \qquad \text{and} \qquad \frac{C_B}{C_C} = k_{BC}\frac{I_B}{I_C}\text{, etc.} \tag{11}$$

Assuming that

$$C_A + C_B + C_C + \ldots = 1, \tag{12}$$

(no other elements exist), the concentrations are calculated by simultaneously solving equations 11 and 12 for Fe, Cr, Ni, Mo, and Si. To calculate the k-factors, concentrations in the bulk of the material, away from the grain boundary, are measured. The k-factor is chosen such that this bulk concentration measurement corresponds to the bulk concentration as measured by electron microprobe:

$$k_{AB} = \frac{C_A^{microprobe}}{C_B^{microprobe}} \frac{I_B^{STEM/EDS}}{I_A^{STEM/EDS}}. \quad (13)$$

The k-factors used were those calculated by Busby using Type 316 SS on the ORNL CM 200. Busby measured the concentration of Cr, Fe, Ni, Si, and Mo in Type 316 and calculated the k-factors using the concentrations measured in the same Type 316 alloy measured using electron microprobe. The k-factors calculated by Busby are shown in Table 14 [33].

Table 14. k-factors used in Composition Calculations

Elements	k-factor
Cr-Ni (k_{CrNi})	0.85
Cr-Fe (k_{CrFe})	0.91
Cr-Si (k_{CrSi})	1.49
Cr-Mo (k_{CrMo})	0.79

In addition to grain boundary measurements and grain boundary profiles, another new technique was also used to measure composition profiles. This technique is known as spectrum imaging. The difference between a spectrum image and profile is shown in the Figure 41. A spectrum image averages multiple profile lines to get the grain boundary profile. The advantage of the spectrum image is that, since less time is spent with the beam focused on any individual area, less damage is done to the sample by the electron beam. Additionally, the spectrum image provides an average over the length of the boundary. The disadvantage is that a spectrum image profile will average out differences in profiles along the length of the boundary. Some spectrum images were taken using a 20x20 grid while others were taken using a 10x10 grid.

2.7.2 Segregation Data

All segregation profile plots, spectrum-image plots, and grain boundary and matrix measurements are contained in Appendix B.

2.7.2.1 Grain Boundary Segregation at 1 dpa

A single sample from hex can S1952 irradiated to 1 dpa at 373°C and displacement rate of 7.6E-08 dpa/s was analyzed. The sample designation was S2T1-5. Three grain boundary profiles and one grain boundary composition measurements are reported. All measurements were taken on a single boundary.

2.7.2.1.1 Grain Boundary Profiles

The three measured grain boundary profiles are plotted in Figures B1-B3. The data away from the grain boundary in Figure B2 (spectra 006) is less reliable because the sample drifted toward the hole during acquisition. The erratic measurements near +18 and +20 nm are caused by this drift. The average profile, calculated using the data from Figures B1-B3 is plotted in Figure B4.

2.7.2.1.2 Grain Boundary Measurement

Spot measurements were taken both on the grain boundary and in the matrix away from the boundary. The concentrations calculated from these measurements are listed in Table B1.

2.7.2.1.3 Discussion of 1 dpa Segregation Data

The average segregation (combining all profile and spot measurement data) for the 1 dpa condition is contained in Table 15. The maximum segregation (largest difference between grain boundary and matrix for 1 dpa) is listed in Table 16.

Table 15. Average Segregation at 1 dpa

Dose (dpa)	Δ Fe (at%)	Δ Cr (at%)	Δ Ni (at%)	Δ Mo (at%)	Δ Si (at%)
1	-4.0	+1.7	-0.1	+2.4	+0.1

Table 16. Maximum Segregation at 1 dpa

Dose (dpa)	Δ Fe (at%)	Δ Cr (at%)	Δ Ni (at%)	Δ Mo (at%)	Δ Si (at%)
1	-8.3	+2.5	+0.3	+4.9	+1.5

At 1 dpa, Fe is depleted at the grain boundary, while Cr and Mo are enriched. Ni and Si do not show consistent depletion or enrichment. These measurements are consistent with other studies [34, 35] that have indicated certain heat treatments will leave Cr and Mo enriched and Fe depleted in 300 series stainless steels. The mechanism driving this segregation is not completely understood but is suspected to be related to bonding between Cr and Mo and another grain boundary impurity such as C, B, or P [35-37].

2.7.2.2 Grain Boundary Segregation at 20 dpa

Grain boundary compositions were measured in sample S1T3 irradiated to 20 dpa at 375°C and at a displacement rate of 1.2E-07 dpa/s. In sample S1T3, two separate grain boundaries were analyzed. Grain boundary composition, grain boundary composition profiles, and spectrum image profiles were measured. Composition measurements in the bulk, away from the boundary were also taken.

For all of the samples analyzed, Si and Mo x-ray peaks were generally only slightly greater than background. The quantitative composition calculations were quite susceptible to the background

subtraction and therefore the uncertainty in Si and Mo concentrations is greater than for Fe, Cr, Ni.

2.7.2.2.1 Grain Boundary Profiles

The measured grain boundary profiles are plotted in Figures B5-B12. The uncertainty bars on the averaged profiles are the standard deviation of the four profile measurements at each distance from the boundary. To compare grain boundary profiles with spectrum image profiles, Figure B13 compares the measured Cr and Ni concentrations for an average of the four profiles and for the spectrum image. The spectrum image profile shows much greater Ni, Mo, and Si segregation than the grain boundary profiles. For this grain boundary, the spectrum image was in a thinner area of the sample, so the greater measured segregation is expected.

2.7.2.2.2 Grain Boundary Measurements

Spot measurements were taken both on the grain boundary and in the matrix away from the boundary. The concentrations calculated from these measurements and from the profiles are listed in Tables B2-B4. The measured Fe, Cr, and Ni segregation are greater in grain boundary 2. In grain boundary 2, Mo is depleted, while in grain boundary 1, Mo is enriched. The grain boundary character apparently determines the rate of segregation.

Thickness played a significant role on the grain boundary composition measurements. In thicker areas of the sample, beam broadening of the nominal 1.4 nm beam will cause greater averaging of the measured profile (where a typical profile is 5-10 nm in width). As expected, the composition measurements in thinner areas consistently show greater segregation. Although thickness was not directly measured, the relative thickness can be estimated from the total counts in the k_α peaks (Si+Cr+Ni+Fe+Mo). For sample S1T3 grain boundary 1 (Table B 2), the difference in thickness is estimated to be 23% between the second (Cr=13.8 at%) and third (Cr=15.8 at%) boundaries. For sample S1T3 grain boundary 2, the difference in thickness is estimated to be 69% between the third (Cr=11.5 at%) and fourth (Cr=11.5 at%) boundaries.

The calculated Mo concentrations for many profiles are unexpectedly large. Bulk Mo levels of 6-9 at% were calculated from the spectra taken at distances far from the boundary. Two possible possibilities could cause this overestimation of the Mo concentration: inappropriate k-factors and excess background counts. For this sample, a spacer that contained some Mo was used in the TEM sample holder. The spacer was not used for sample S1T5.

While the spectrum image measures about the same Cr concentration as the grain boundary profiles, the grain boundary Ni concentrations as measured using the spectrum image technique are larger.

2.7.2.2.3 Discussion of 20 dpa Segregation Data

The average segregation (combining all profile and spot measurement data) for the 20 dpa condition is contained in Table 17. The maximum segregation (largest difference between grain boundary and matrix for 20 dpa) is listed in Table 18. Cr, which was enriched at 1 dpa, is now depleted. Fe, which was depleted at 1 dpa, is less depleted at 20 dpa. Mo, which was enriched at

1 dpa, is essentially the same as the bulk Mo composition. The average Mo includes data from grain boundary 1 where Mo is still enriched and grain boundary 2, where Mo is depleted.

Table 17. Average Segregation at 20 dpa

Dose (dpa)	Δ Fe (at%)	Δ Cr (at%)	Δ Ni (at%)	Δ Mo (at%)	Δ Si (at%)
20	-1.9	-3.9	+5.5	-0.3	+0.6

Table 18. Maximum Segregation at 20 dpa

Dose (dpa)	Δ Fe (at%)	Δ Cr (at%)	Δ Ni (at%)	Δ Mo (at%)	Δ Si (at%)
20	-9.4	-6.4	+11.3	-1.9	+2.1

2.7.2.3 Grain Boundary Segregation at 30 dpa

Sample S1T5 was irradiated at 379°C, at a displacement rate of 1.8E-07 dpa/s, to a dose of 30 dpa. In sample S1T5, a single grain boundary was analyzed. For sample S1T5, grain boundary 1, one grain boundary measurement, three grain boundary profiles, and two spectrum image profiles were taken.

2.7.2.3.1 Grain Boundary Profiles

The measured grain boundary profiles are plotted in Figures B14-B18. To compare grain boundary profiles with spectrum image profiles, Figure B19 compares the measured Cr and Ni concentrations for an average of three profiles and for the Spectrum Image 002. The uncertainty bars on the averaged profiles is the standard deviation of the three profile measurements at each distance from the boundary.

2.7.2.3.2 Grain Boundary Measurement

Spot measurements were taken both on the grain boundary and in the matrix away from the boundary. The concentrations calculated from these measurements are listed in Table B5.

2.7.2.3.3 Discussion of 30 dpa Segregation Data

The average segregation (combining all profile and spot measurement data) for the 30 dpa condition is contained in Table 19. The maximum segregation (largest difference between grain boundary and matrix for 30 dpa) is listed in Table 20. At 30 dpa, Cr continues to deplete and Ni continues to enrich. Fe has returned to bulk level while Mo has depleted.

Table 19. Average Segregation at 30 dpa

Dose (dpa)	Δ Fe (at%)	Δ Cr (at%)	Δ Ni (at%)	Δ Mo (at%)	Δ Si (at%)
30	0.1	-4.1	5.5	-1.3	-0.1

Table 20. Maximum Segregation at 30 dpa

Dose (dpa)	Δ Fe (at%)	Δ Cr (at%)	Δ Ni (at%)	Δ Mo (at%)	Δ Si (at%)
30	-1.9	-4.7	+7.4	-1.4	-0.1

Precipitation was more evident in the grain boundaries in sample S1T5. The composition was measured in three precipitates and is listed in Table B5. All are rich in nickel and silicon. Two of the three are rich in chromium. The effect of a precipitate on segregation can be seen in Figure B20. The profile taken between the precipitates is significantly different from those taken away form the precipitates.

The calculated Mo concentrations are more reasonable than in sample S1T3. For this sample, a Be spacer was used. The spectrum image profile is very similar to the grain boundary profiles for this sample. Grain boundary segregation can be altered significantly by the presence of precipitation.

2.7.3 Summary of Grain Boundary Segregation at 1, 20, and 30 dpa

Tables 21 and 22 indicate the average segregation and the maximum segregation as a function of dose for the 1, 20, and 30 dpa samples. In precipitate free boundaries, the average Cr and Ni segregation appears to have reached steady-state values by 20 dpa. The Mo and Fe still change between 20 and 30 dpa. The maximum segregation is greater in the 20 dpa sample than in the 30 dpa sample.

Table 21. Average segregation as a function of dose

Dose (dpa)	Δ Fe (at%)	Δ Cr (at%)	Δ Ni (at%)	Δ Mo (at%)	Δ Si (at%)
1	-4.0	+1.7	-0.1	+2.4	+0.1
20	-1.9	-3.9	+5.5	-0.3	+0.6
30	0.1	-4.1	5.5	-1.3	-0.1

Table 22. Maximum segregation as a function of dose

Dose (dpa)	Δ Fe (at%)	Δ Cr (at%)	Δ Ni (at%)	Δ Mo (at%)	Δ Si (at%)
1	-8.3	+2.5	+0.3	+4.9	+1.5
20	-9.4	-6.4	+11.3	-1.9	+2.1
30	-1.9	-4.7	+7.4	-1.4	-0.1

No phosphorous peak was seen at any boundaries analyzed in samples S1T3 and S1T5. The data from sample S2T1 was also reanalyzed, specifically looking for phosphorous. No phosphorous was seen at any boundary analyzed. In austenitic stainless steels where P enrichment is seen, grain boundary compositions of 1-2 at% are typical [34, 35]. In samples S1T3, S1T5, and S2T1, any grain boundary phosphorous is below the level of detectability and grain boundary P enrichment is not probable. Because Mo and Cr enriched in the 1 dpa sample, but no P was seen,

it is unlikely that preferential bonding between P and either Cr or Mo is responsible for the low dose enrichment.

2.8 Comparison of Microstructure and Tensile Properties

Dispersed hardening theory predicts that the total yield strength in an irradiated material is the sum of the yield strength in the unirradiated material plus the incremental increase due to irradiation induced microstructural features:

$$\sigma_i = \sigma_o + \Delta\sigma_y \tag{13}$$

The change in yield strength from microstructural obstacles (dislocation loops, voids, and precipitates) can be estimated from dispersed hardening theory [14]. The change in yield strength due to discrete obstacles is given by:

$$\Delta\sigma_y = M\alpha\mu b\sqrt{Nd} \tag{14}$$

where M relates the shear stresses on a slip plane in a single crystal to the applied tensile stress necessary to activate slip in a polycrystal, α is the barrier strength, μ is the shear modulus of the matrix, b is the Burgers vector of a moving dislocation, N is the number density, and d the average diameter. The inverse of the quantity $\sqrt{Nd}$ represents average obstacle spacing.

For dislocations, the yield strength increment is given by:

$$\Delta\sigma_y = M\alpha\mu b\sqrt{\rho_d} \tag{15}$$

where ρ_d is the dislocation density (line length per unit volume). In cold-worked material, the initial yield strength includes a component due to dislocations and therefore during the irradiation, the yield strength increment due to dislocations can either increase or decrease the total yield strength.

Different models exist for adding the contributions from each type of obstacle (loop, void, dislocation) [38]. A simple linear summation model would add the contributions as follows:

$$\sigma_i = \sigma_o + \Delta\sigma_y^{voids} + \Delta\sigma_y^{loops} + \Delta\sigma_y^{disl} \tag{16}$$

A more commonly accepted approach is to add the contribution from the shortrange obstacles (loops and voids) in a root mean square fashion and the longrange obstacles (dislocations) linearly [14]:

$$\sigma_i = \sigma_o + \Delta\sigma_y^{disl} + \sqrt{\left(\Delta\sigma_y^{voids}\right)^2 + \left(\Delta\sigma_y^{loops}\right)^2} \tag{17}$$

The strength increments caused by the microstructural evolution can be calculated using data from 3 microstructural samples. The microstructural strength increment will be compared to the yield strength measured in the tensile tests.

The increment in yield strength due to loops, voids, and loops plus voids can be calculated from eq. (17) and compared to the measured yield strength. This comparison is made in Figure 42 using the 1 dpa measurements as the reference. The sum of the microstructural contribution was calculated using the root-mean-square summation: ($\Delta\sigma_y = \Delta\sigma_y^{dislocations} + \sqrt{\left(\Delta\sigma_y^{voids}\right)^2 + \left(\Delta\sigma_y^{loops}\right)^2 \left(\Delta\sigma_y^{precipitates}\right)^2}$). The values of α and μ used to calculate the yield strength increment are taken from Reference [14] and listed in Table 23. The values of M and b used to calculate the yield strength increment are taken from Reference [39] and are also listed in Table 23. The unirradiated yield strength for 20% cold-worked Type 316 stainless steel tested at 370°C used in calculating the data in Figure 42 is 580MPa [6]. The estimated cold-work for 20% cold-worked Type 316 stainless steel is $3x10^{15}$ cm^{-2} [39].

Figure 42 indicates that the changes in measured yield strength generally track the changes in yield strength calculated from the microstructure using the inputs from Table 23.

Table 23. Constants for Yield Strength Increment Calculations

Parameter	Precipitates	Dislocations	Voids	Loops
M	3	3	3	3
α	0.33	0.11	1	0.33
μ	$6.7x10^{10}$ Pa	$6.7x10^{10}$ Pa	$6.7x10^{10}$ Pa	$6.7x10^{10}$ Pa
b	$2.5x10^{-10}$ m	$2.5x10^{-10}$ m	$2.5x10^{-10}$ m	$2.5x10^{-10}$ m

In section 2.1.3, it was noted that the unirradiated yield strength of the 20% cold-worked material in this study and that of Fish et al. varied by about 15%. From equation (17), assuming solution annealed Type 316 has a yield strength of about 180 MPa, an increase in dislocation density of around 50% is required to increase the yield strength by approximately 15%. Because these ducts went through stringent quality assurance programs, it is unlikely the cold-work actually differed by 50%. The difference is more likely to be based on differences in base composition.

REFERENCES

[1]. K.L. Basehore and N.E. Todreas, "SUPERENERGY-2 A Multiassembly, Steady-state Computer Code for LMFBR Core Thermal-Hydraulic Analysis", PNL-3379, COO-245-57TR, UC-72, dated August 1980

[2]. W. Yang, "Fortran 77 Version of SE2-ANL", ANL Intra-laboratory Memo, dated March 3, 1993

[3]. D. Meneghetti and D.A. Kucera, "Apparent Discrepancies between Calculated and Measured Peripheral Temperature in EBR-II Reflector Subassemblies", ANL Intra-laboratory Memo, dated January 14, 1992 and "Errata", dated March 25, 1992.

[4]. J.F. Koenig, "Summary of Reflector Temperature Measurements and Calculations", ANL Intra-laboratory Memo, dated May 19, 1992

[5]. F. A. Garner, in Materials Science and Technology: Nuclear Materials, Vol. 10, edited by B. R. T. Frost (VCH, New York, 1993) p. 422.

[6]. R. L. Fish, N. S. Cannon and G. L. Wire, ASTM STP 683, 1979, p. 450.

[7]. R.L. Fish, "Tensile Properties of 20% C.W. Type 316 Stainless Steel Irradiated to 6.0×10^{22} n/cm^2 (E>0.1 MeV)," Hanford Engineering Development Laboratory, TC-675-4, 1977, Vol. 1, pp. 1-1 through 1-16.

[8]. R.L. Fish, "Tensile Properties of Irradiated 20% Cold-Worked. AISI 316," Hanford Engineering Development Laboratory, TC-160-5, 1977, pp. 337-344.

[9]. H. R. Brager, L. D. Blackburn, and D. L. Greenslade, J. Nucl. Mater., 122123 (1984) 332-337.

[10] J. M. Dupouy, J. Erler, and R. Huillery, Proceedings of the International Conference on Radiation Effects in Breeder Reactor Structural Materials, American Institute of Mining, Metallurgical, and Petroleum engineers, 1977, p. 83.

[11]. T. Yoshitake, T. Donomae, S. Mizuta, H. Tsai, R. V. Strain, T. R. Allen, and J. Cole, "Tensile Properties of 12% Cold-Worked Type 316 Stainless Steel Irradiated in EBR-II under Low-Dose-Rate Conditions to High Fluence," Effects of Radiation on Materials: 20th International Symposium, ASTM STP 1405, S. T. Rosinski, M. L. Grossbeck, T. R. Allen and A. S. Kumar, Eds., American Society for Testing and Materials, West Conshohocken, PA, 2001, p. 469.

[12]. N. J. Carson Jr., C. Steves, C. J. Renken, K. J. Reinmann, and H. Berger, ANL-7982, December 1972.

[13]. H. R. Higgy, F. H. Hammad, J. Nucl. Mater., 55 (1975) 177.

[14]. G. E. Lucas, J. Nucl. Mat. **206** (1993) 287-305.

[15]. B. J. Makenas, J. F. Bates, J. W. Jost, Effects of Radiation on Materials: Eleventh Conference, ASTM STP 782, H. R. Brager and J. S. Perrins, Eds., American Society for Testing and Materials, 1982, pp. 17-29.

[16]. T. R. Allen, J. I. Cole, H. Tsai, S. Ukai, S. Mizuta, and T. Yoshitake, The Effect of Low Dose Rate Irradiation on the Swelling of 12% Cold-Worked 316 Stainless Steel, *Proceedings of the Ninth International Symposium on Environmental Degradation of Materials in Nuclear Power Systems-Water Reactors*, , S. Bruemmer, P. Ford, G,. Was Eds., Newport Beach, CA, TMS, Warrendale, PA, (August 1999), p.1035.

[17]. T. R. Allen, J. I. Cole, and E. A. Kenik, "Radiation-Induced Segregation and Void Swelling in 304 Stainless Steel," Effects of Radiation on Materials: 20th International Symposium, ASTM STP 1405, S. T. Rosinski, M. L. Grossbeck, T. R. Allen, and A. S.

Kumar, Eds., American Society for Testing and Materials, West Conshohocken, PA, 2002, p.427.

[18]. D. B. Williams and C. B. Carter, in Transmission Electron Microscopy: A Textbook for Materials Science, Plenum Press, NY 1996.

[19]. G. Schoeck, J. App. Phys., **33** (1962) pp. 1745-1747

[20]. P. J. Maziasz, J. A. Horak and B. L. Cox, in Phase Stability During Irradiation, edited by J. R. Holland, L. K. Mansur and D. I. Potter, The Metallurgical Society of AIME, Warrendale, PA 1981.

[21] Johnson, G. D., Garner, F. A, Brager, H. R., and Fish, R. L., Effects of Radiation on Materials: Tenth conference, ASTM STP 725, D. Kramer, H. R. Brager, and J. S. Perrin, Eds., American Society for Testing and Materials, 1981, pp. 393-412.

[22]. P. J. Maziasz and C. J. McHargue, Int. Mat. Rev., **32 (4)** (1987). p. 190

[23]. W. J. S. Yang, in Radiation-Induced Changes in Microstructure: 13th International Symposium, ed. F. A. Garner, N. H. Packan, and A. S. Kumar. (ASTM, 1987)) p. 628.

[24]. E. H. Lee and L. K. Mansur, J. Nucl. Mat., **278**, (2000) pp. 20-29.

[25]. D. F. Pedraza and P. J. Maziasz, in Radiation-Induced Changes in Microstructure: 13th International Symposium, ed. F. A. Garner, N. H. Packan, and A. S. Kumar. (ASTM, 1987)) p. 161.

[26]. H. R. Brager and F. A. Garner, in Effects of Radiation on Structural Materials, ed. J. A. Sprague, and D. Kramer, (ASTM, 1979)) p. 207.

[27]. J. 1. Cole and T. R. Allen, in Mat. Res. Soc. Symp. Proc. Vol. 540, (MRS, 1999) p. 433. A. J. Jacobs and S. Dumbill, in: Proceedings of the 7th International Symposium on Environmental Degradation of Materials in Nuclear Power Systems-Water Reactors (NACE International, Houston, TX, 1995) 1021-1031.

[28]. J. T. Busby, G. S. Was, and E. A. Kenik, in: Microstructural Processes in Irradiated Materials, Vol. 540, edited by S. J. Zinkle, G. E. Lucas, R. C. Ewing, and J. S. Williams (Materials Research Society, Boston, MA, 1999) 495-500.

[29]. D. L. Porter, G. L. McVay, and L. C. Walters, in *Effects of Radiation on Materials: Tenth Conference*, ASTM STP 725, edited by D. Kramer, H. R. Brager, and J. S. Perrin (American Society for Testing and Materials, 1981) 500-511.

[30]. J. J. Holmes, R. E. Robbins, J. L. Brimhall and B. Mastel, Acta Met. **16** (1968) 955-967.

[31]. J. O. Stiegler and E. E. Bloom, J. Nucl. Mat. **33** (1969) 173-185.

[32]. L. E. Thomas, Beeston, J. M., J. Nucl. Mat. **107** (1982) 159-167.

[33]. J. R. Busby, Private communication.

[34]. J. Walmsley, P. Spellward, S. Fisher, and A. Jenssen, "Microchemical characterisation of grain boundaries in irradiated steels," Proc. Seventh Int. Symp. on Env. Deg. of Materials in Nuclear Power Systems-Water Reactors, R.E Gold and E.P Simonen (Ed.), Breckenridge, CO (1995), p. 985.

[35]. C. C. Goodwin, R. G. Faulkner, J. C. Walmsley, and P. Spellward, Effects of Radiation on Materials: 19th International symposium, ASTM STP 1366, M. L. Hamilton, A. S. Kumar, S. T. Rosinski, and M. L. Grossbeck, Eds., American Society for Testing and Materials, West Conshohocken, PA 2000, p. 801.

REFERENCES
(Contd.)

[36]. E. P. Simonen and S. M. Bruemmer, Proc. Eighth Int. Symp. on Env. Deg. of Materials in Nuclear Power Systems-Water Reactors, Amelia Island, FL (1997), p. 751.
[37]. E. A. Kenik, J. T. Busby, M. K. miller, A. M. Thuvander, and G. S. Was, Mat. Res. Soc. Proc. Vol. 540, Materials Research Society, 1999, p. 445.
[38]. G. D. Johnston, F. A. Garner, H. R. Brager, and R. L. Fish, Effects of Radiation on Materials: Tenth Conference, ASTM STP 725, D. Kramer, H. R. Brager, and J. S. Perrin, Eds., American Society for Testing and Materials, 1981, pp. 393-412.

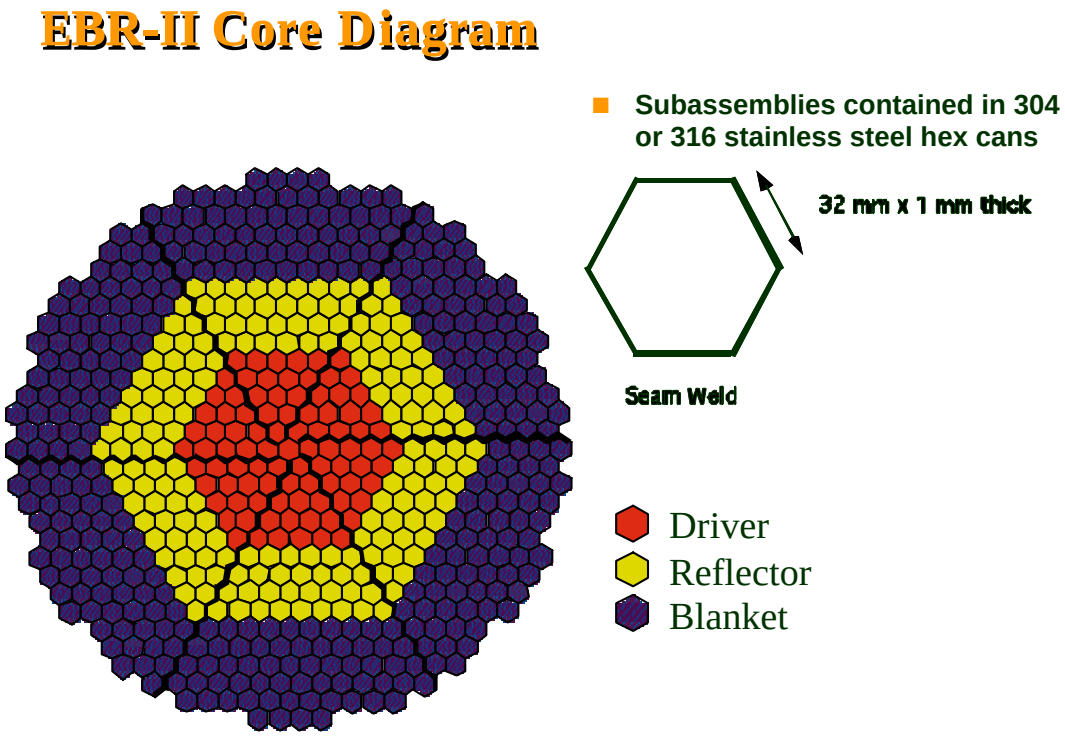

Figure 1. Core Configuration of the EBR-II Reactor

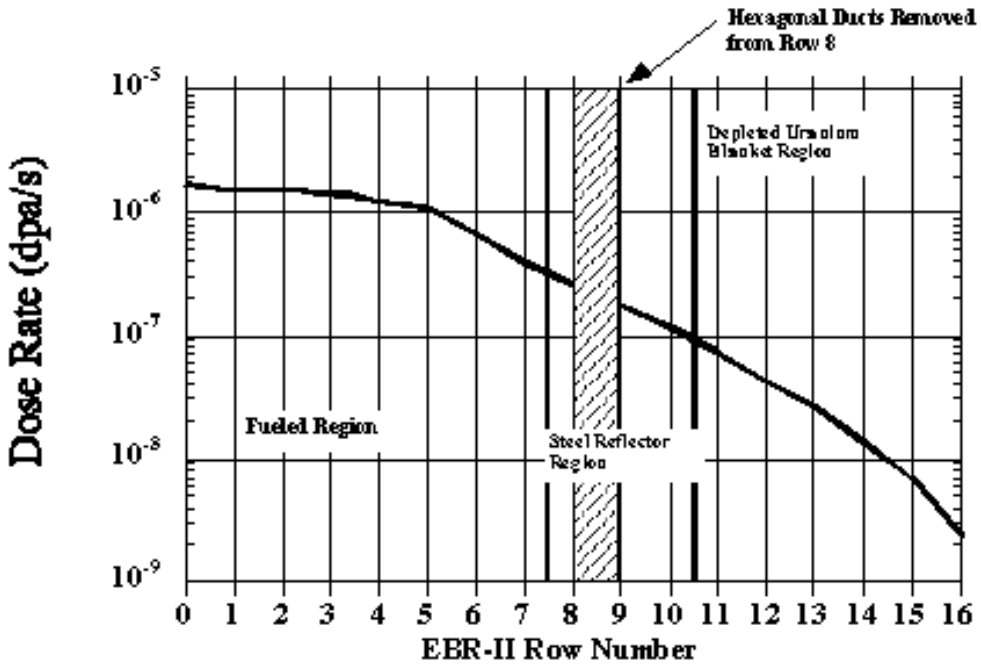

Figure 2. Dose Rate as a Function of Radial Position

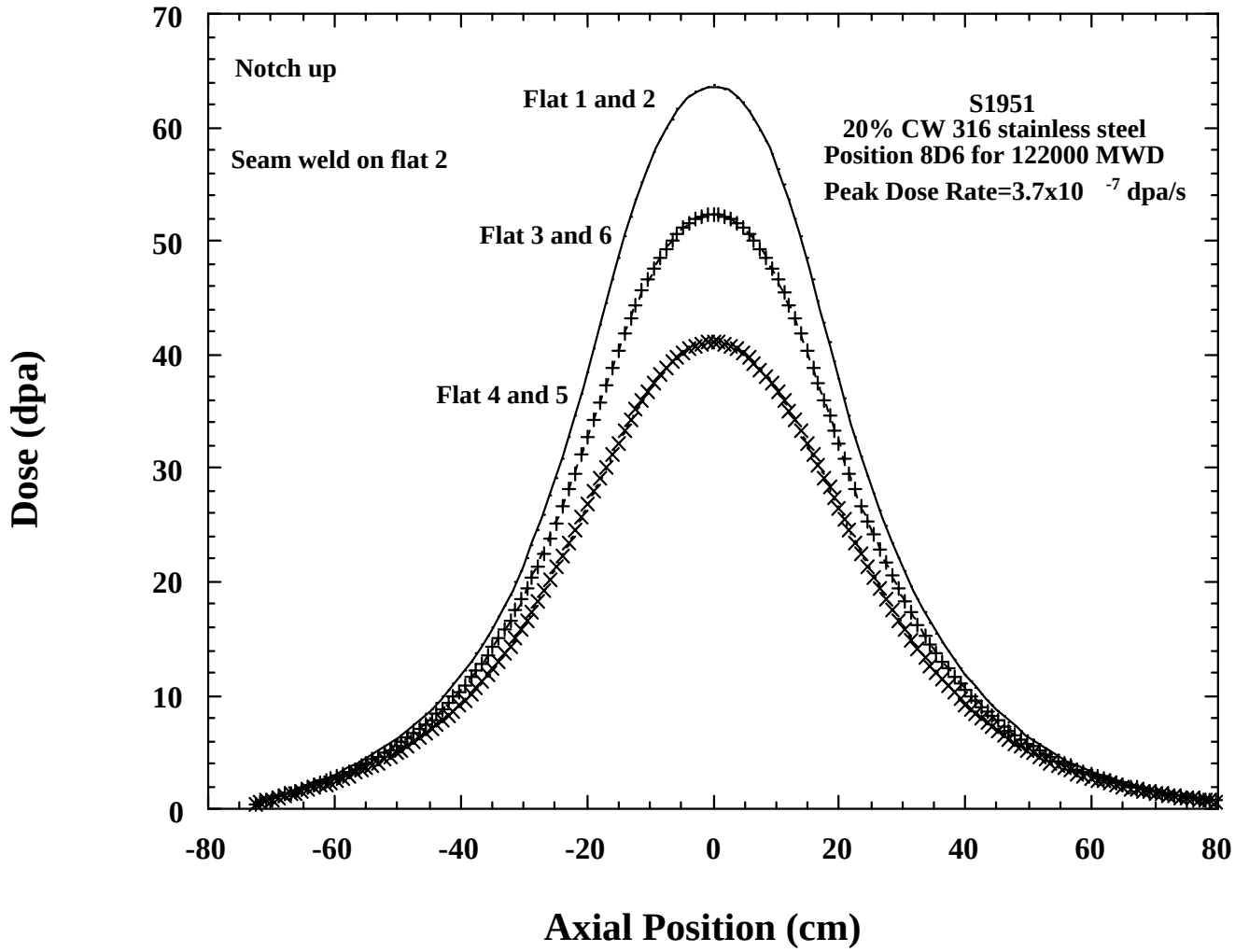

Figure 3. Dose as a Function of Axial Position for Hex Can S1951

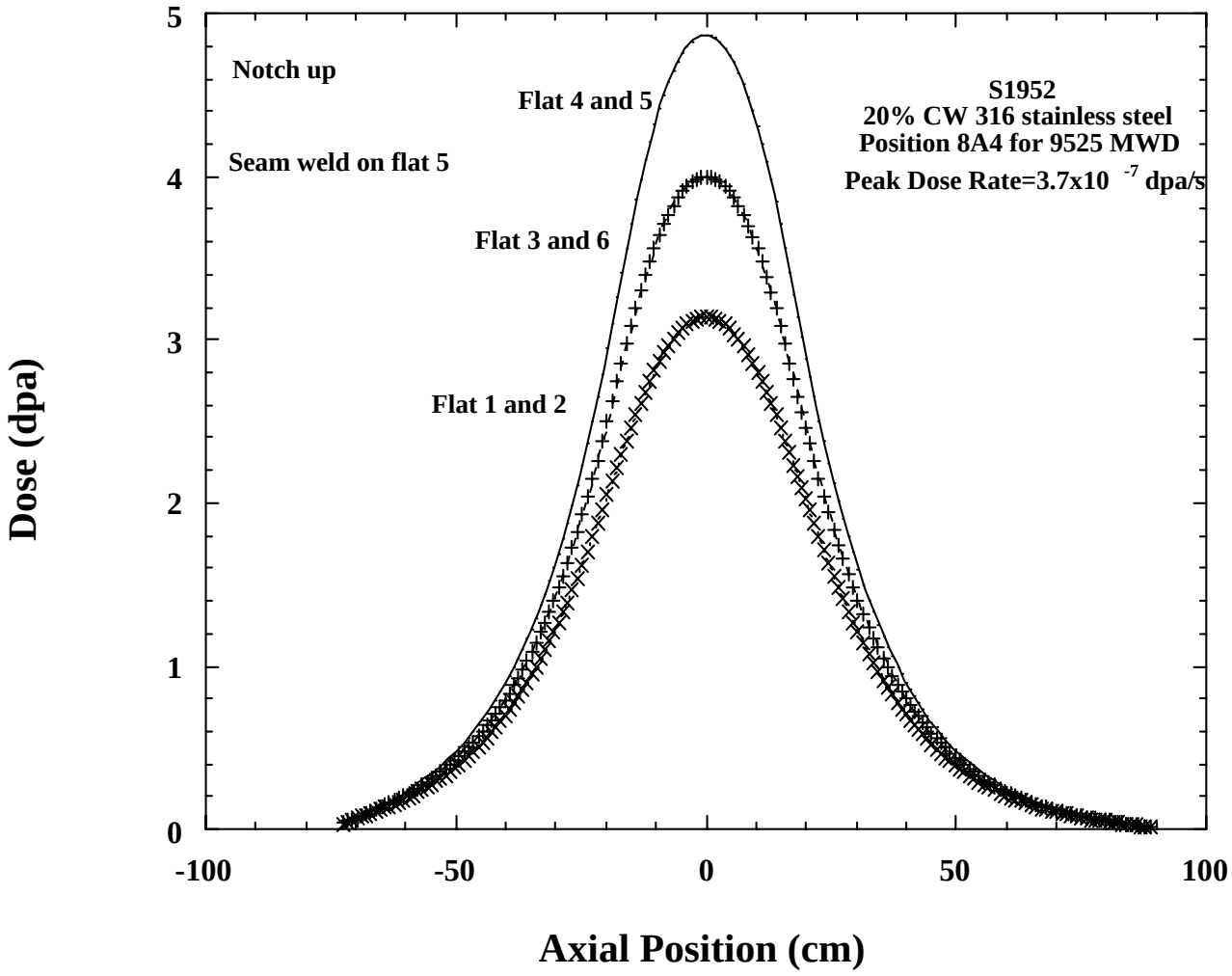

Figure 4. Dose as a Function of Axial Position for Hex Can S1952

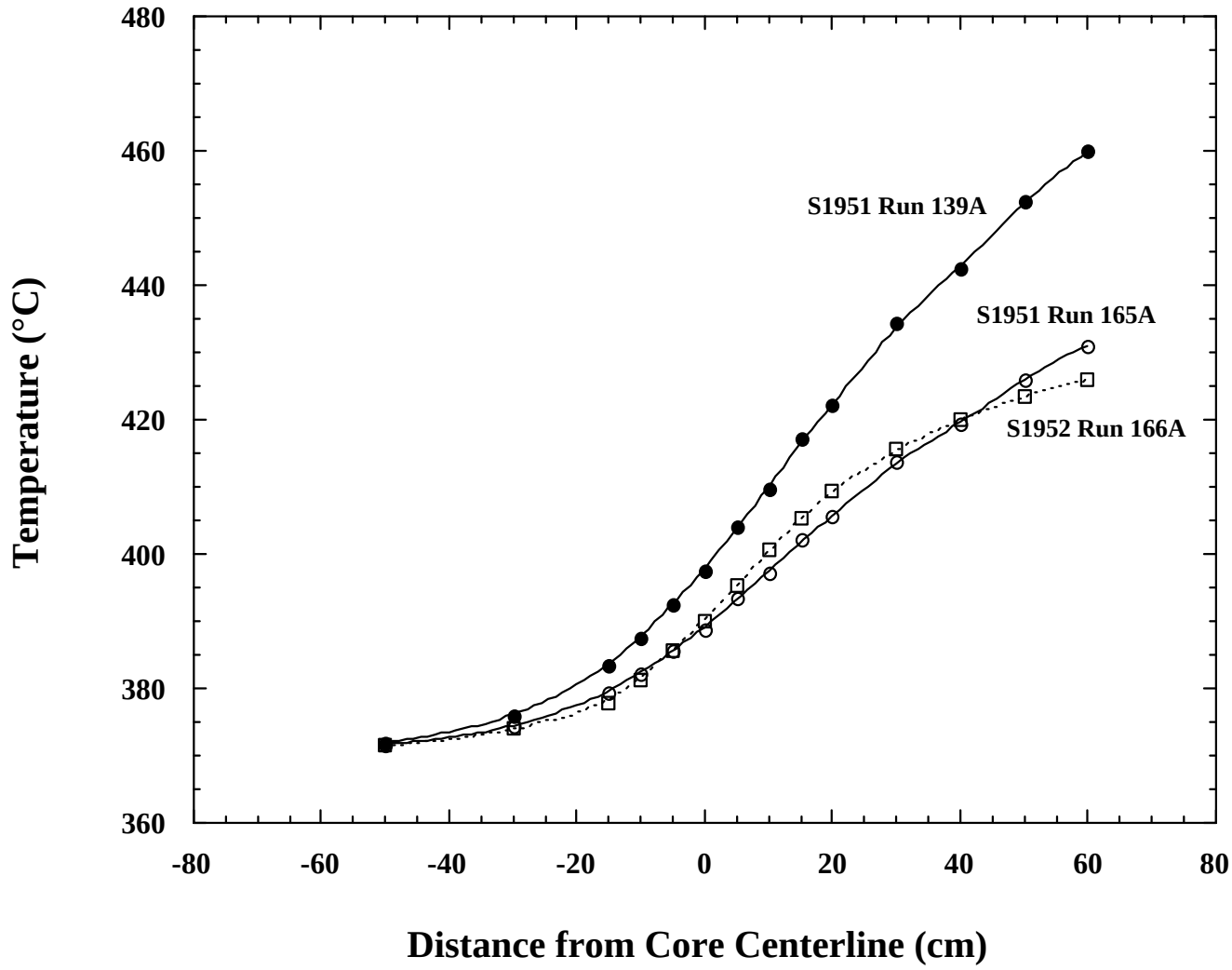

Figure 5. Temperature Distribution for Hex Cans S1951 and S1952

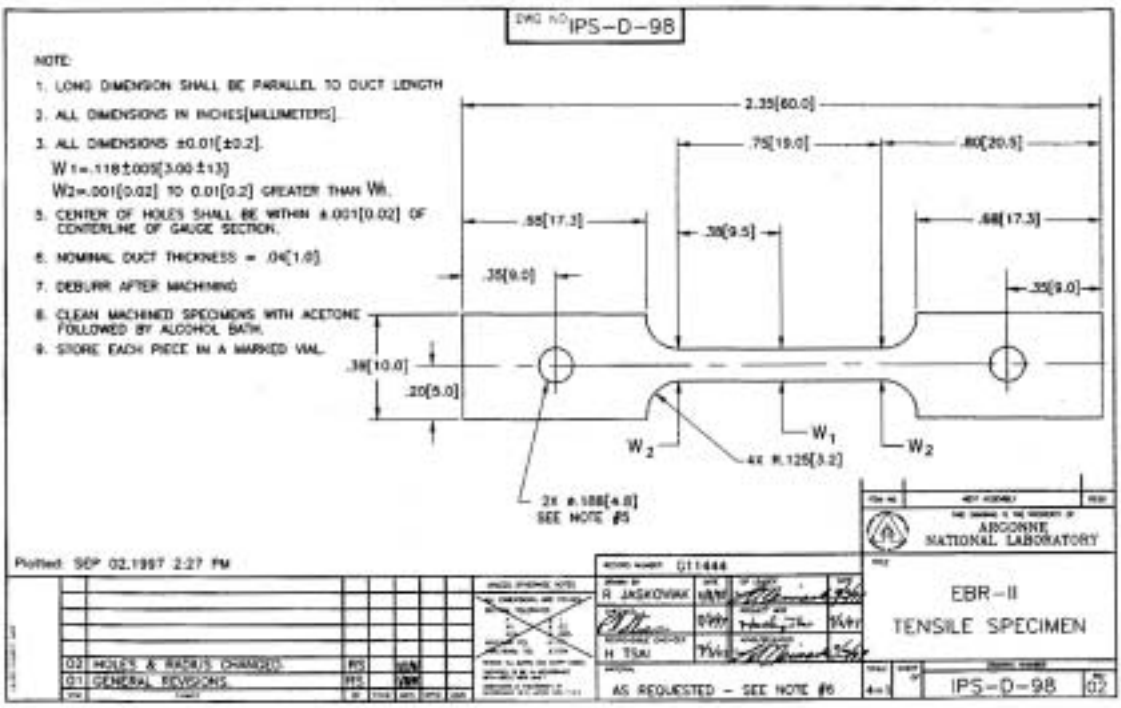

Figure 6. Design of the Tensile Specimen

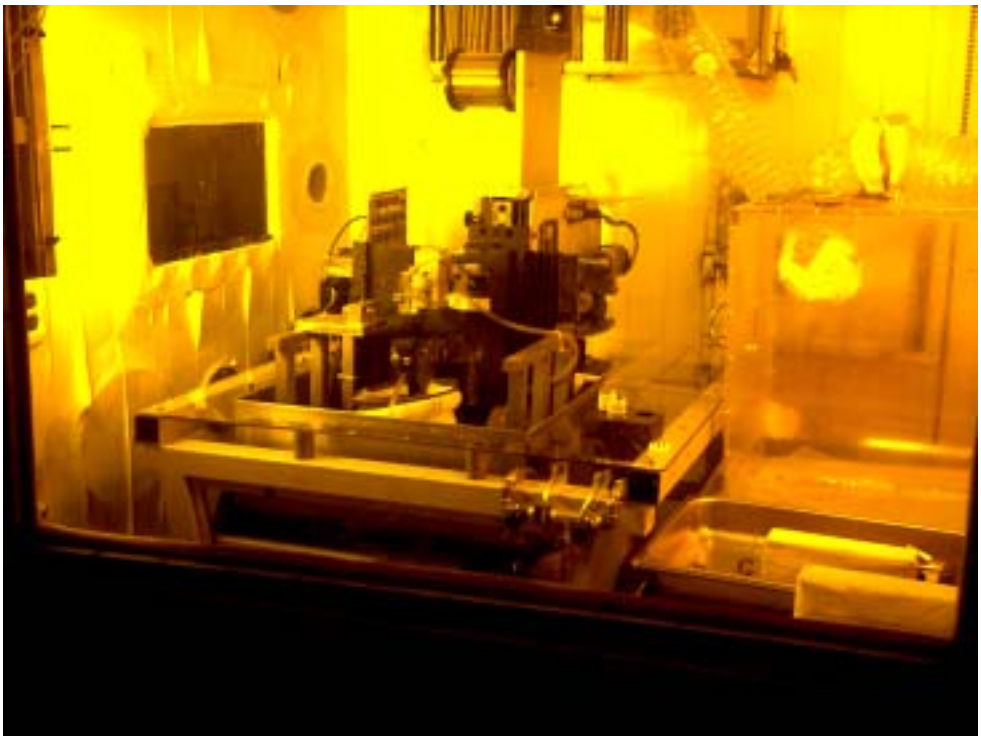

Figure 7. The Electric Discharge Machine Used to Prepare the Tensile Specimens (The machine is located inside a hot cell and the work was performed remotely.)

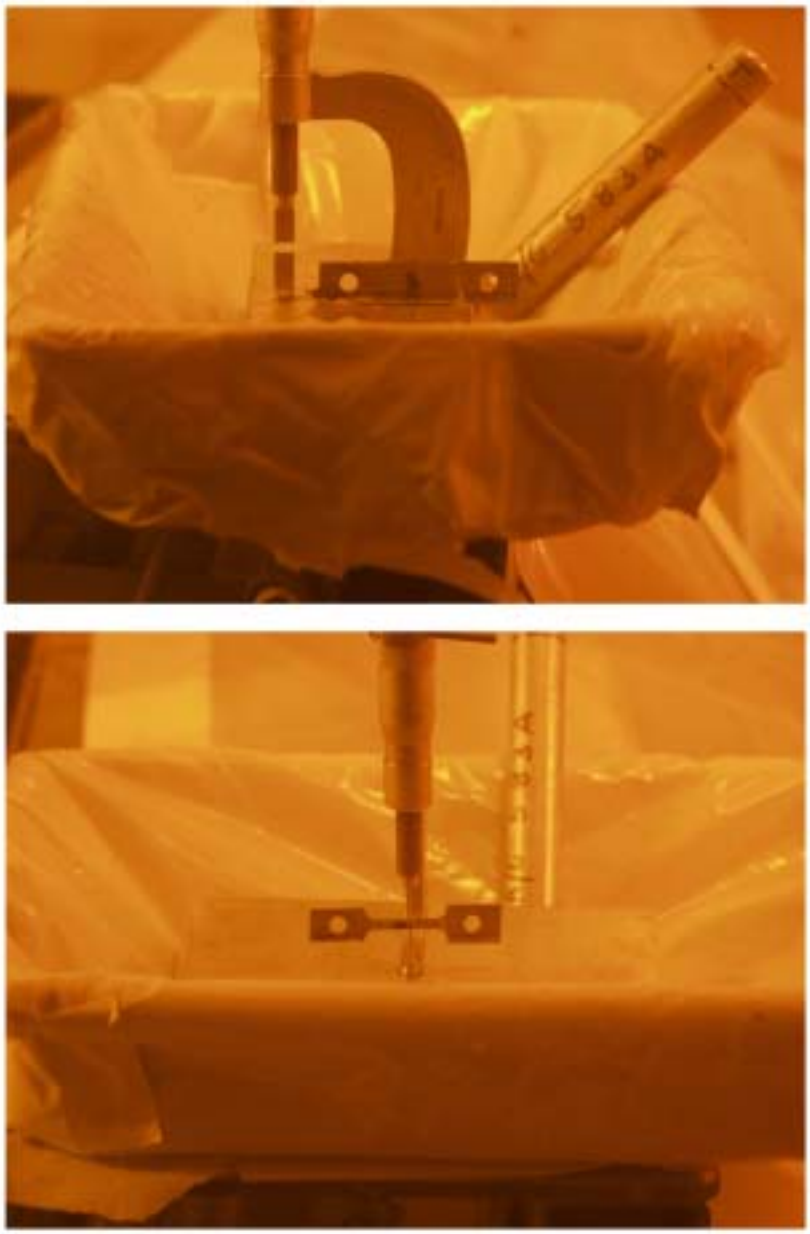

Figure 8. A Tensile Sample Before and After the Final Machining

(To minimize radioactive waste generation, only one grip section was machined, hence the difference in grip width. The difference did not impact the test conduct or tensile properties.)

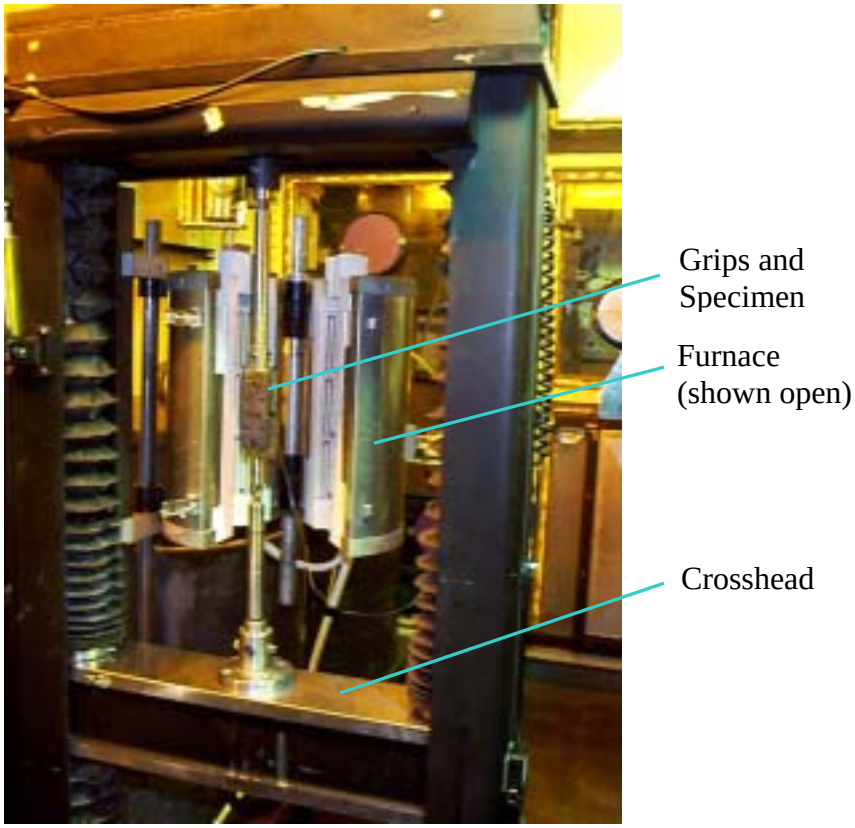

Figure 9. The Instron Tensile Tester in the Hot Cell

(The control console is located outside.)

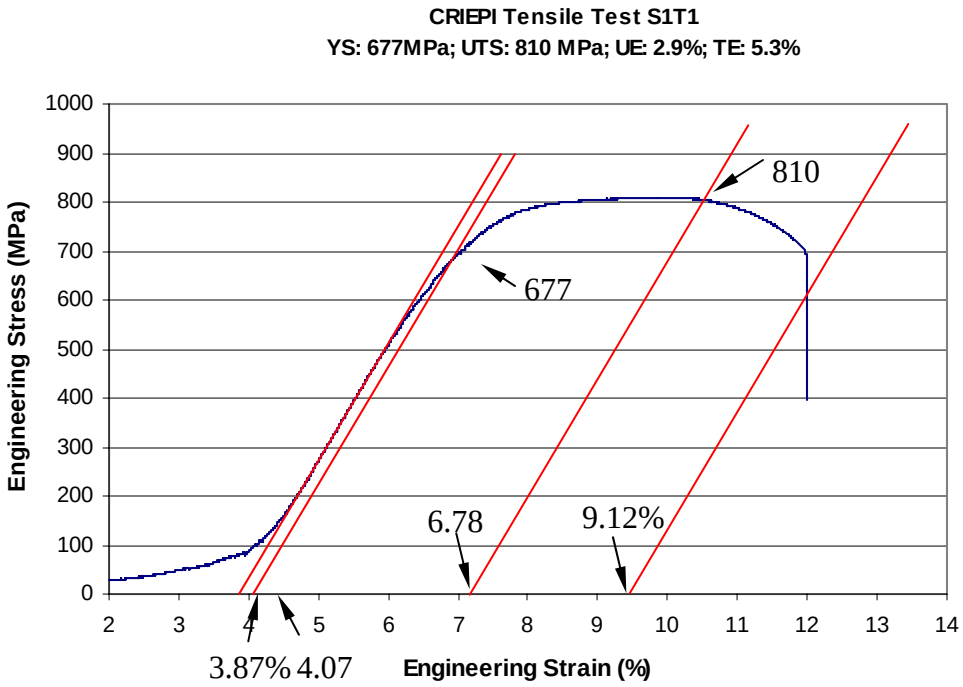

Figure 10. Method for Determining the Engineering Tensile Properties

(The four parallel lines were superimposed on the stress-stress curve for illustration. The elongations were: uniform elongation: 6.78% - 3.87% = 2.9%; total elongation: 9.12% - 3.87% = 5.3%.)

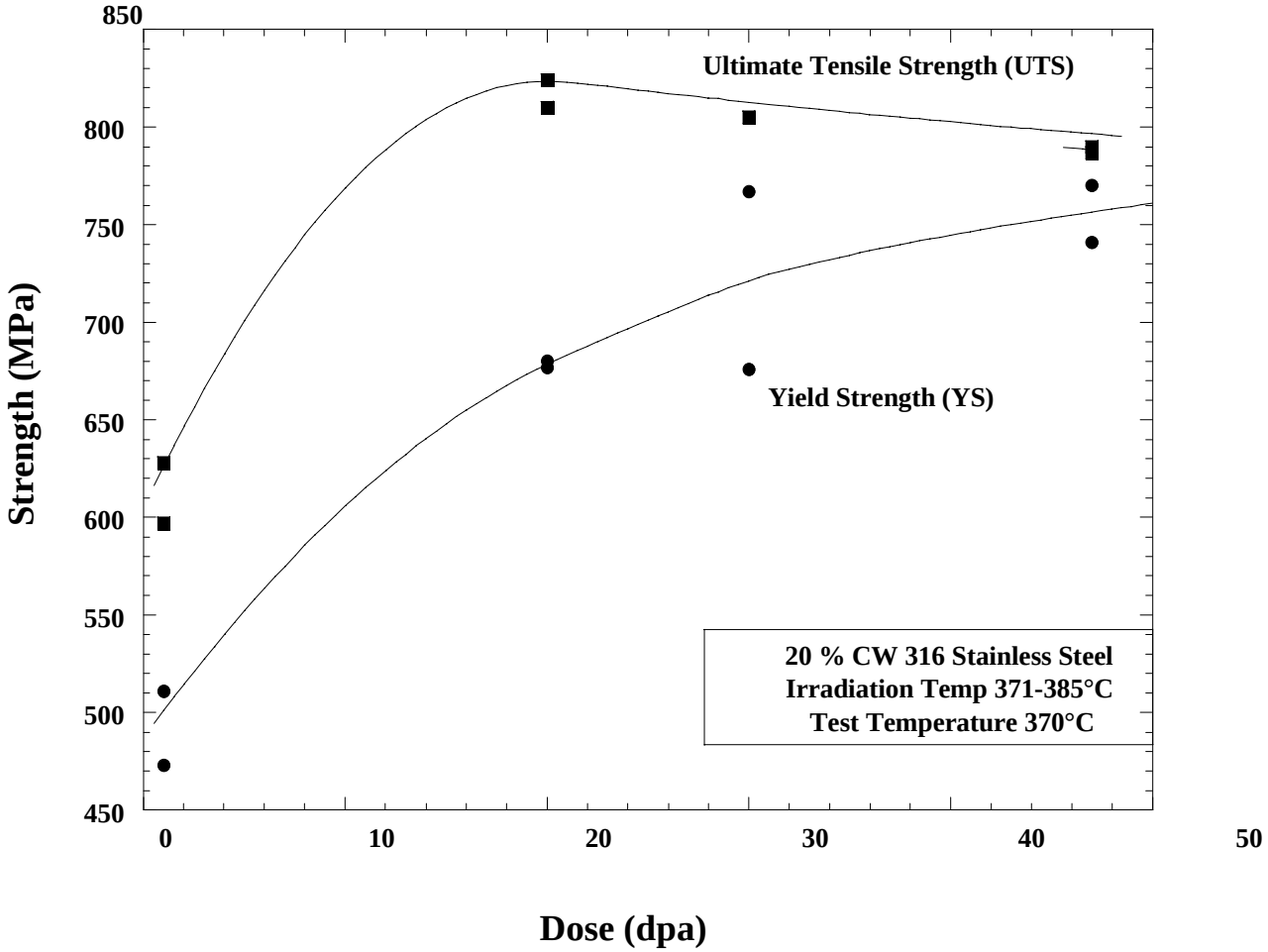

Figure 11. Ultimate Tensile Strength (UTS) and 0.2% Offset Yield Strength (YS) for 20% Cold-worked

(Type-316 stainless steel hex can duct materials irradiated in EBR-II. The irradiation temperatures were from 371 to 385°C and the test temperature was 370°C. The strain rate was $4x10^{-5}$/s.)

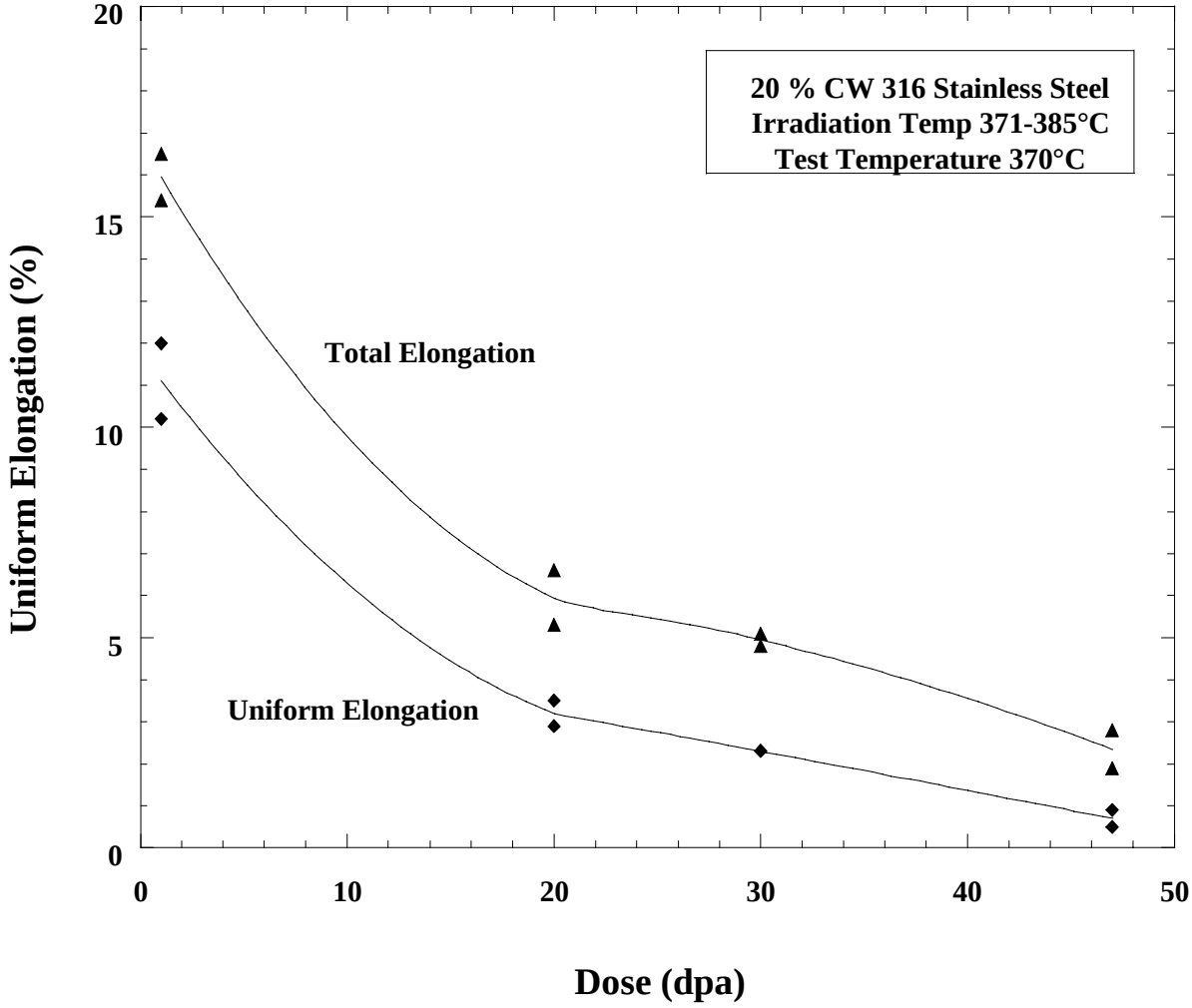

Figure 12. Total and Uniform Elongations for 20% Cold-worked Type-316 Stainless Steel Hex Can Duct Materials Irradiated in EBR-II

(The irradiation temperatures were from 371 to 385°C and the test temperature was 370°C. The strain rate was $4x10^{-5}$/s.)

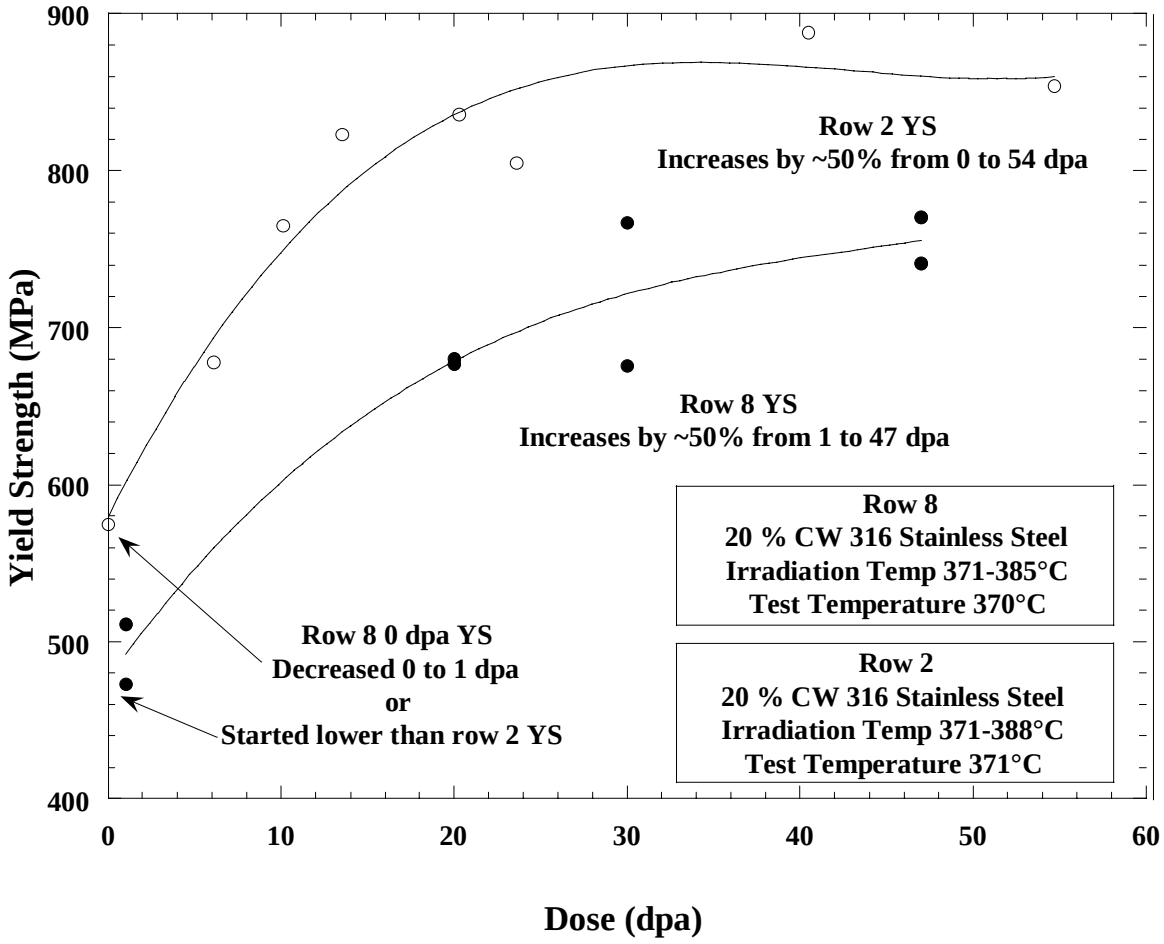

Figure 13. Yield Strength Versus Dose for Samples Irradiated in Row 8 and Row 2 EBR-II

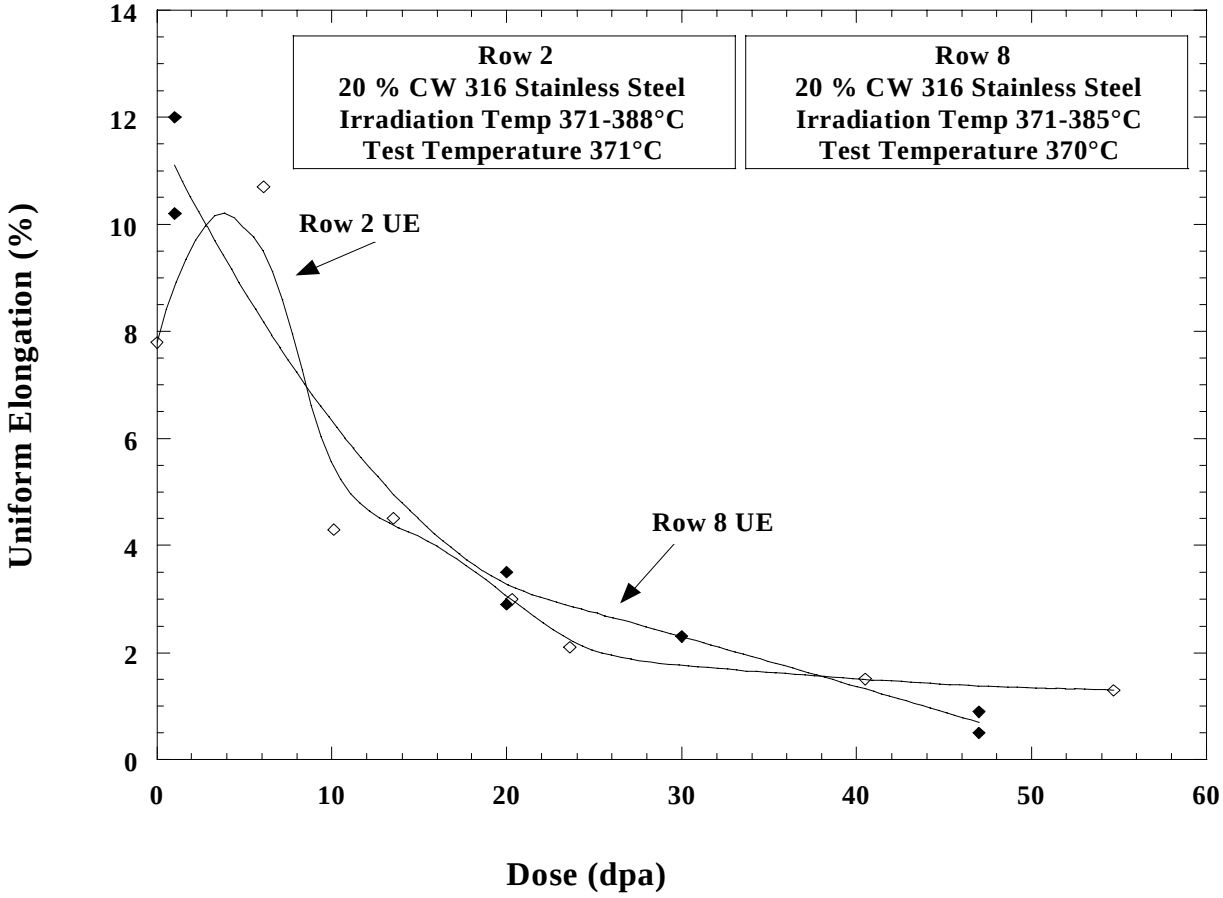

Figure 14. Uniform Elongation as a Function of Dose for samples Irradiated in Row 8 and Row 2 of EBR-II

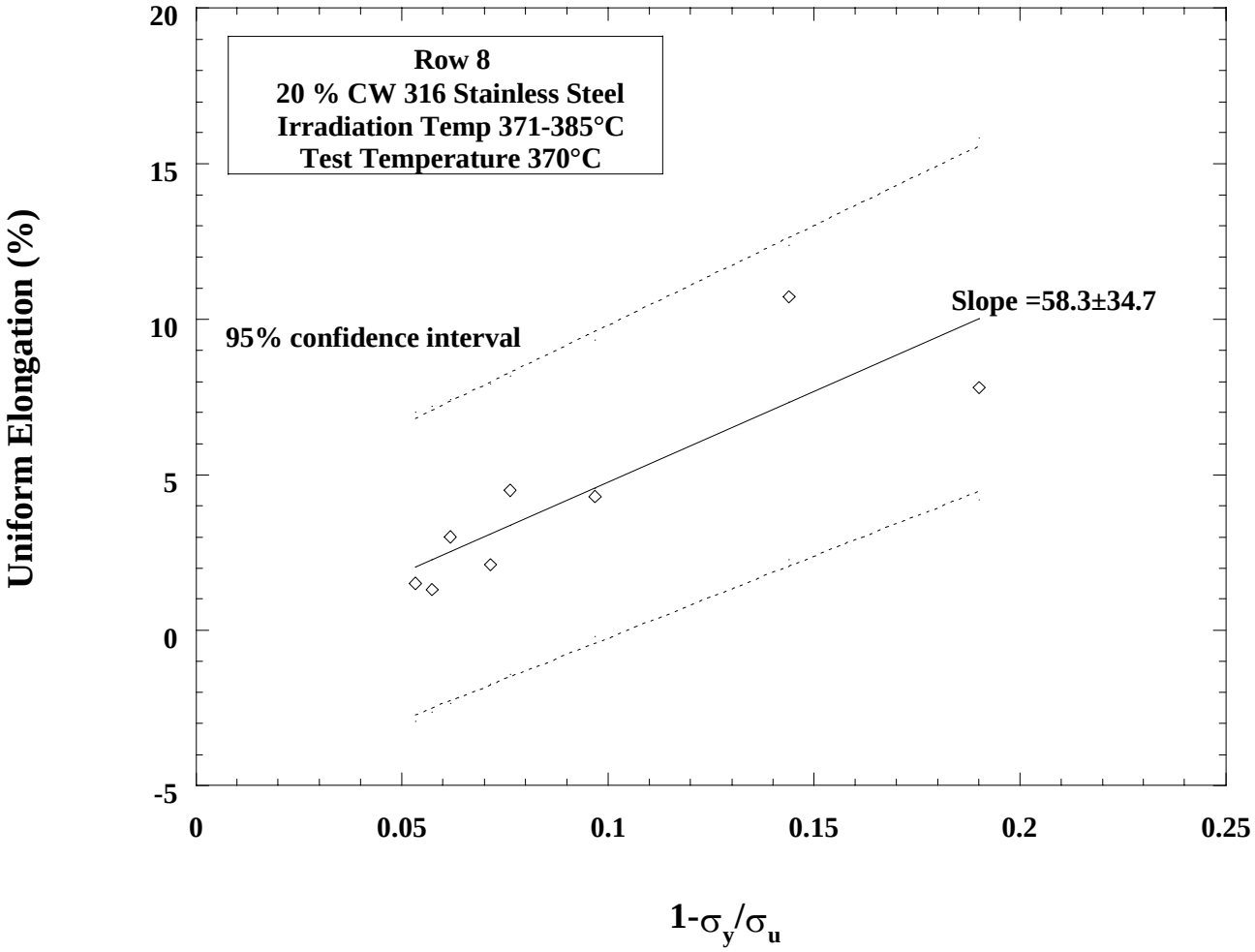

Figure 15. Uniform Elongation as a Function of Hardening for Samples Irradiated in Row 8 of EBR-II

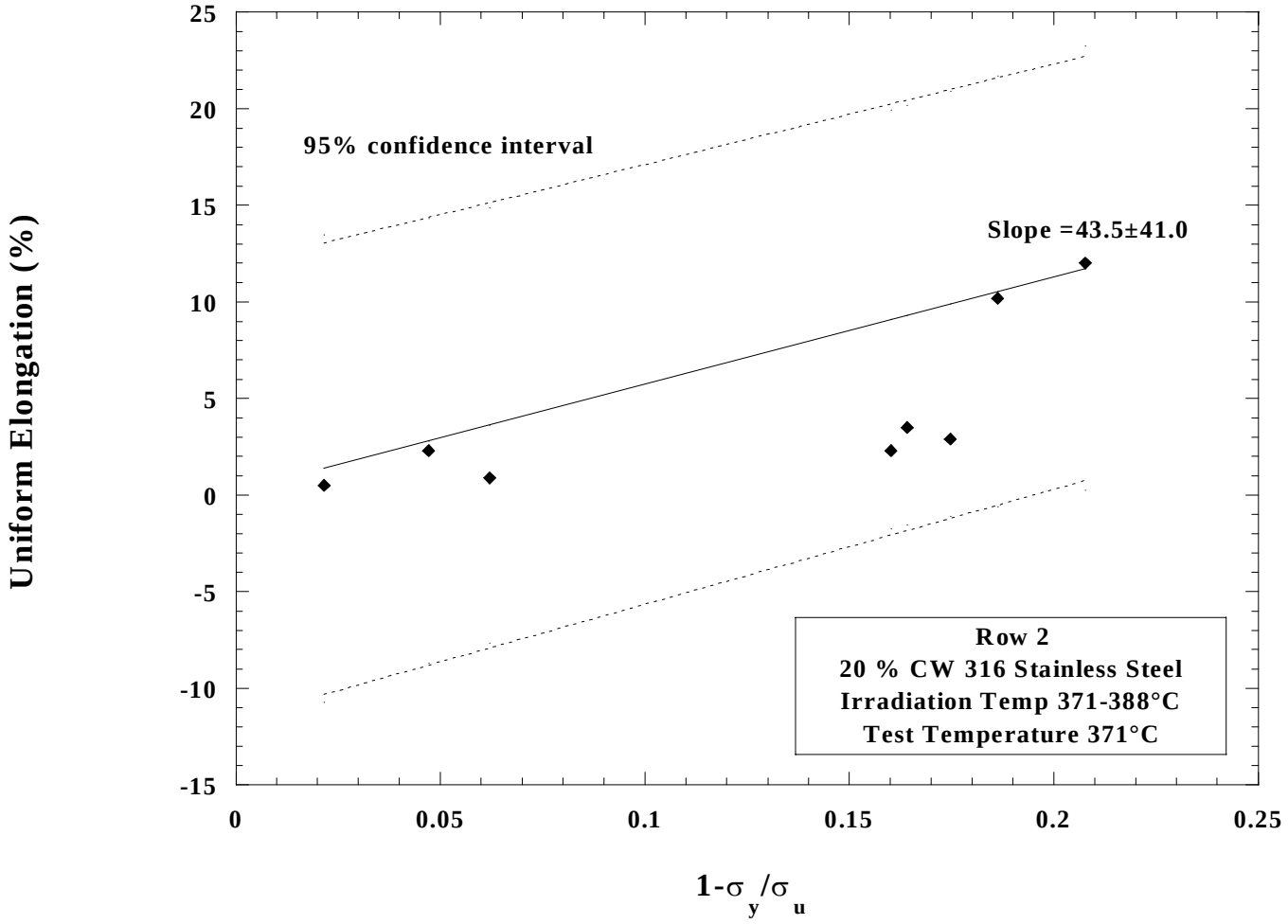

Figure 16. Uniform Elongation as a Function of Hardening for Samples Irradiated in Row 2 of EBR-II

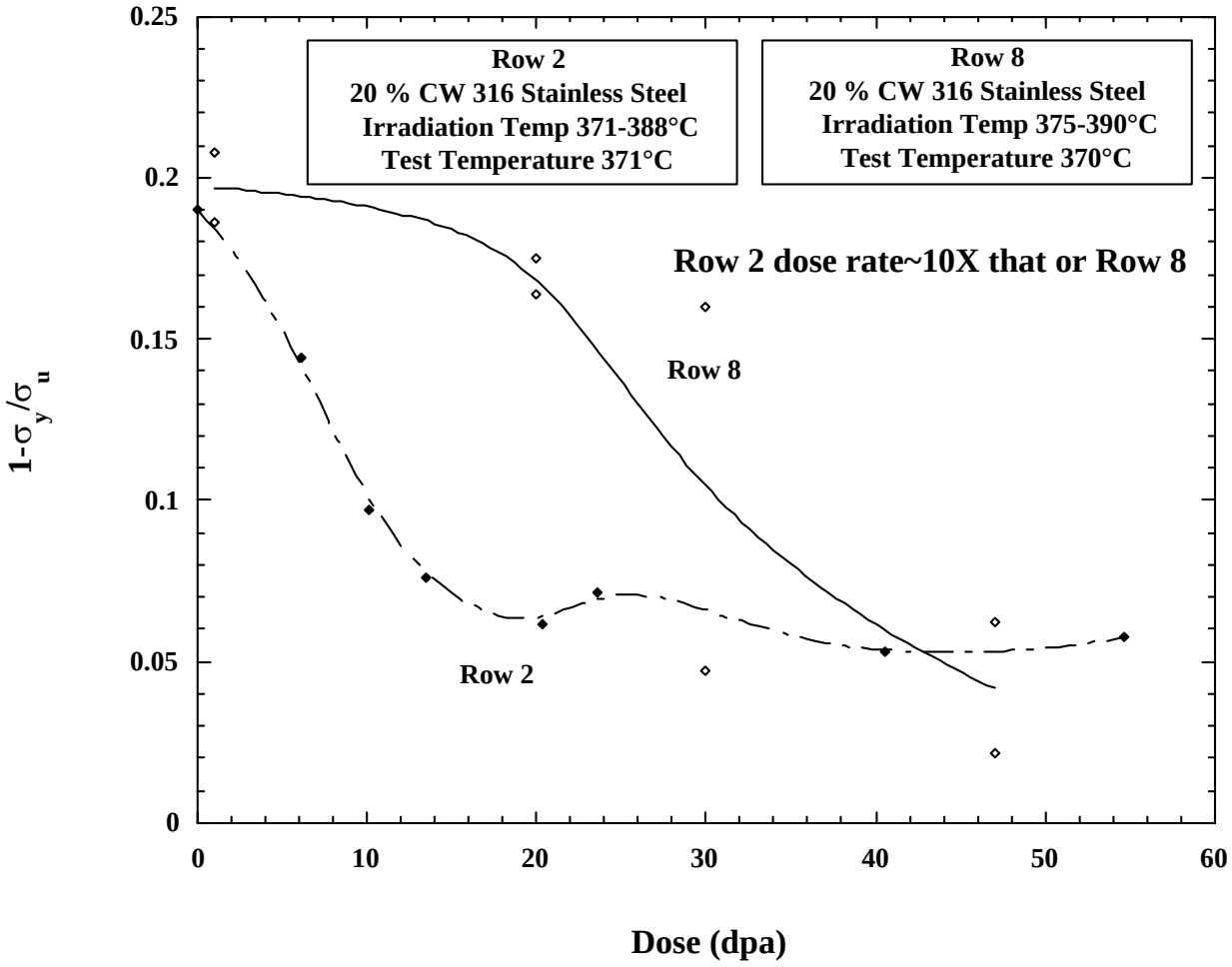

Figure 17. Hardening as a Function of Dose

(The higher dose rate row 2 samples lose work hardening capability faster.)

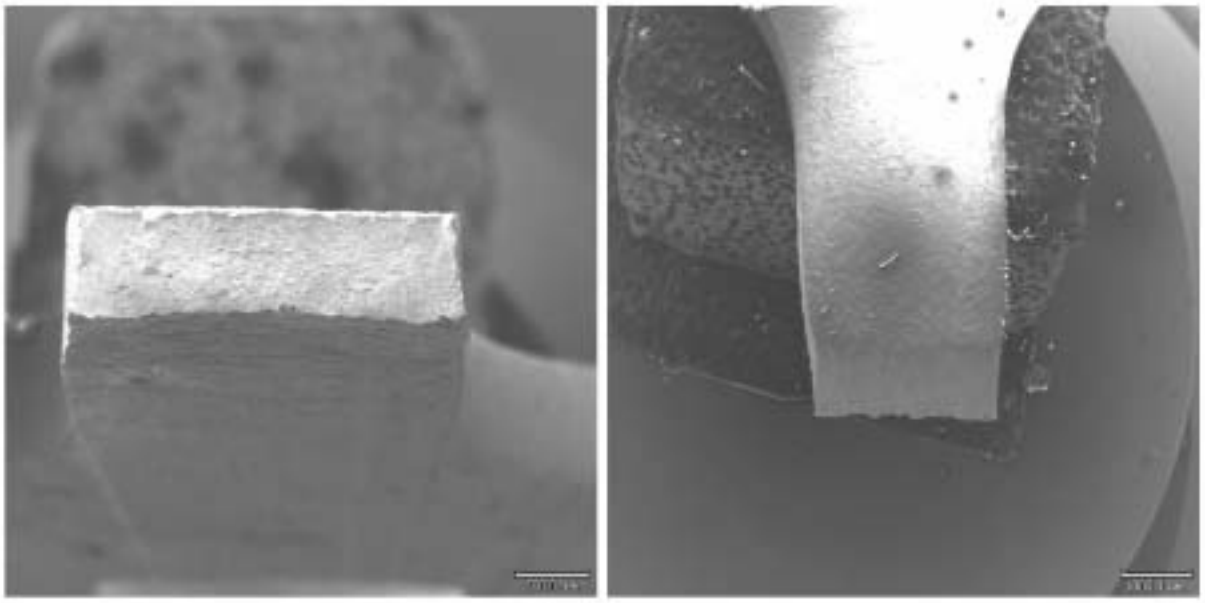

S1T4

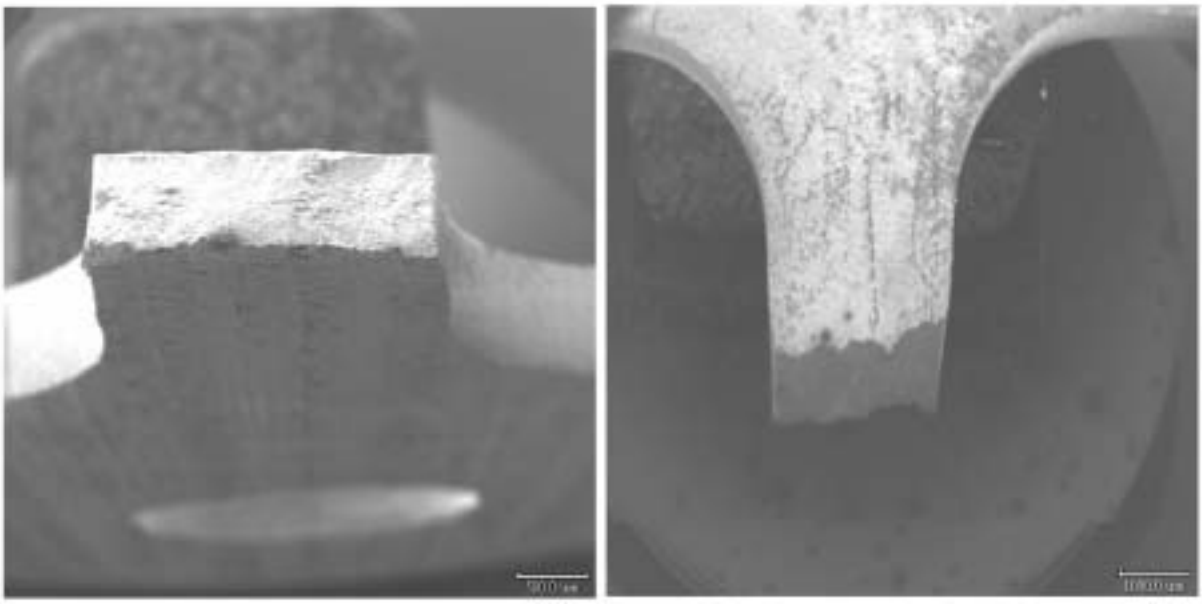

S1T5

Figure 18. Fracture Surfaces

(Top) Fracture tips showing discernible necking in the 30-dpa S1T4 specimen.
(Bottom) Necking is largely absent in the 47-dpa S1T5 specimen.

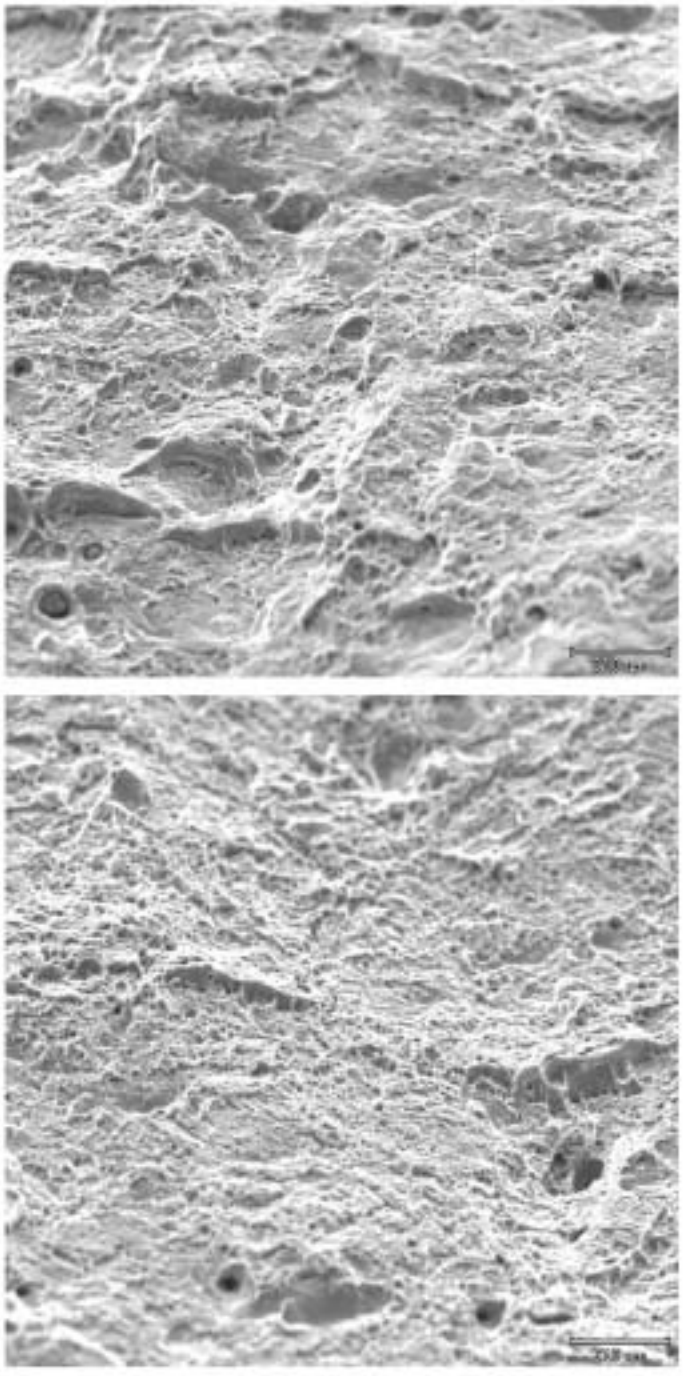

Figure 19. Areas of Fracture Surface of S1T4 Showing Ductile Dimples Mixed with Facets

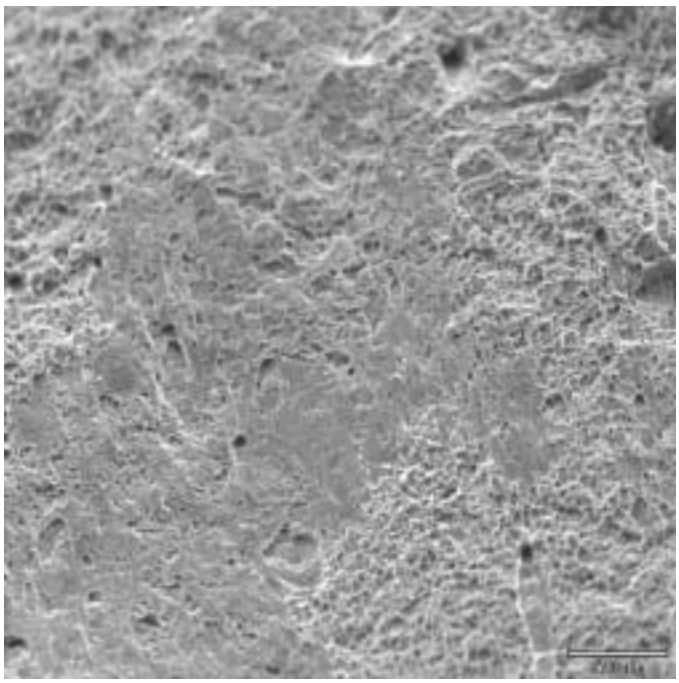

Figure 20. Area of Fracture on S1T4 showing Both Ductile dimples and Transgranular Shear Features

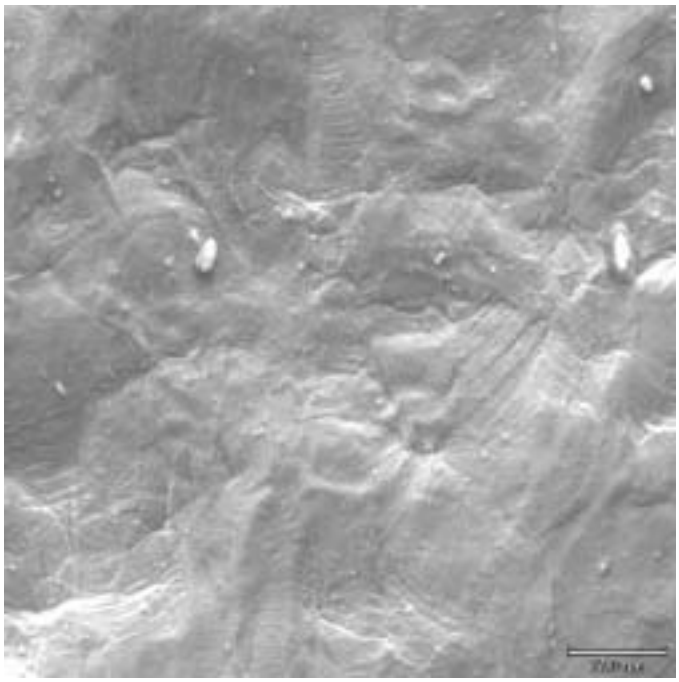

Figure 21. Step Pattern Found on the Sides of the S1T4 Specimen

(Suggesting dislocation channeling in the material.)

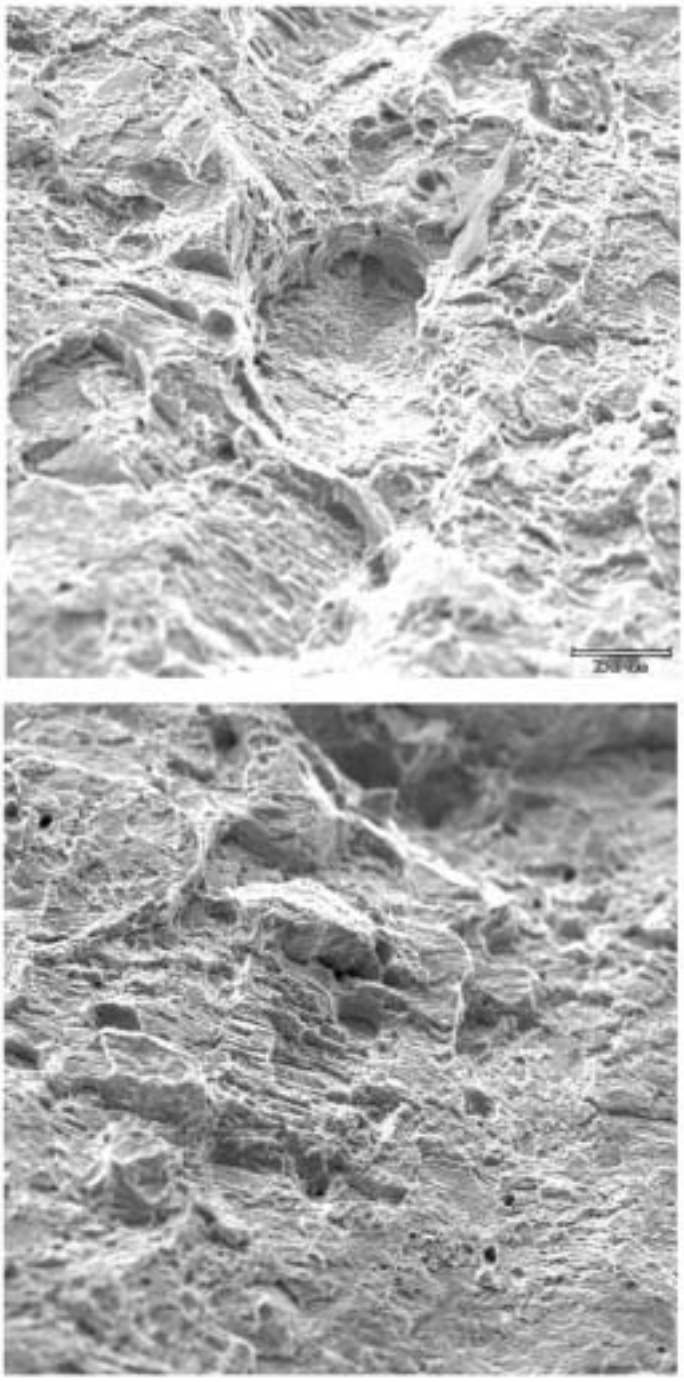

Figure 22. Fracture of the S1T5 Specimen Showing Channel Faceted Surface

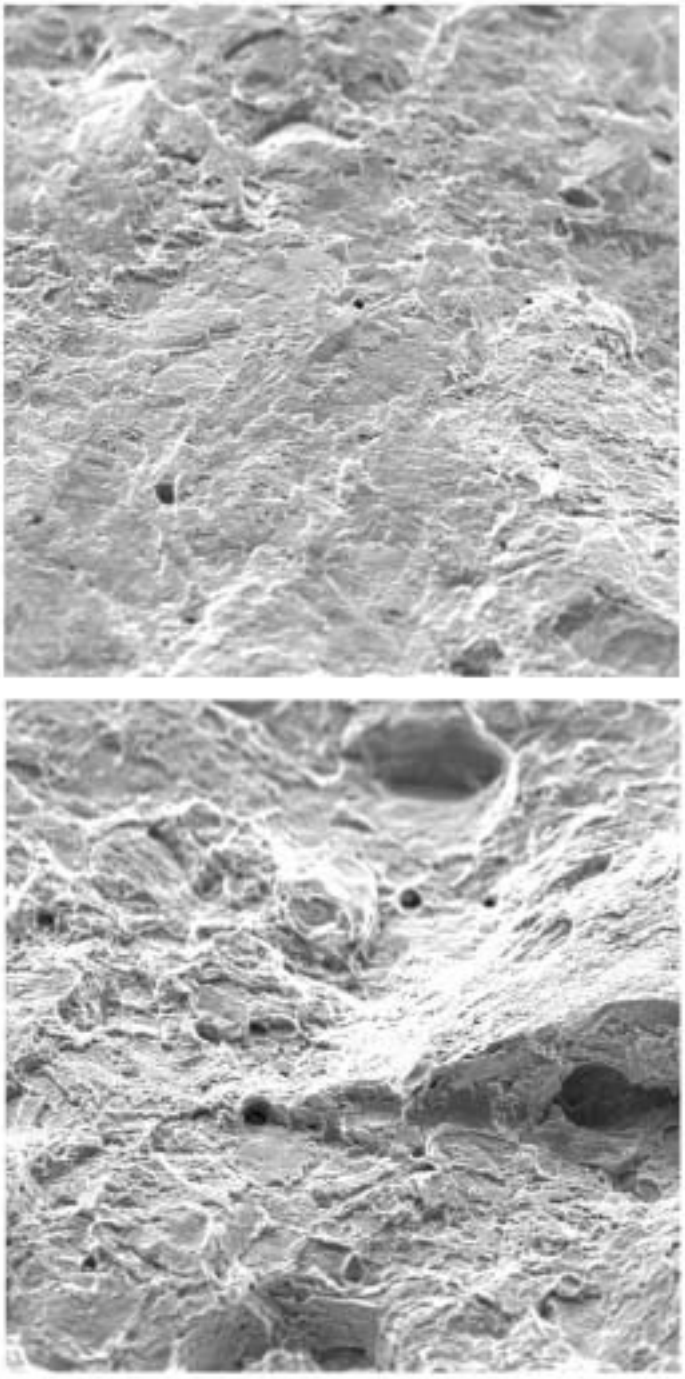

Figure 22 (continued). Fracture of the S1T5 Specimen Showing Channel Faceted Surface

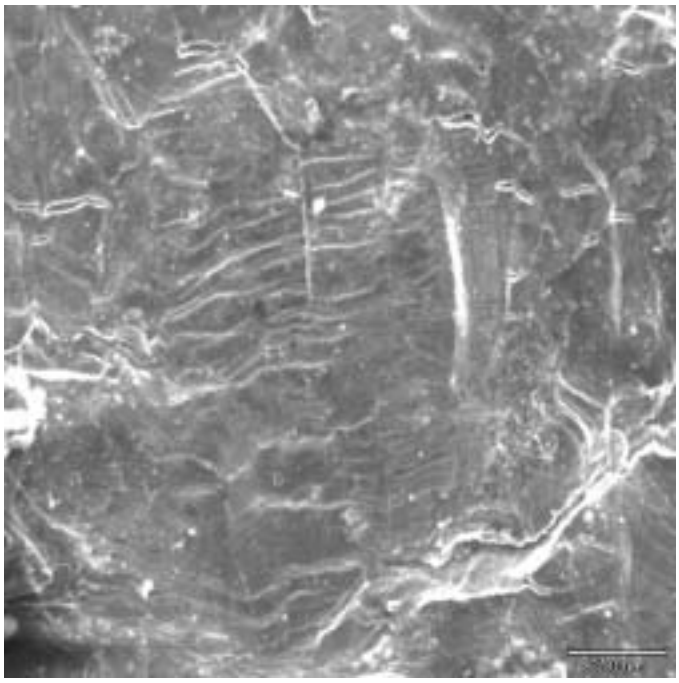

Figure 23. Steps on the Sides of the S1T5 Specimen

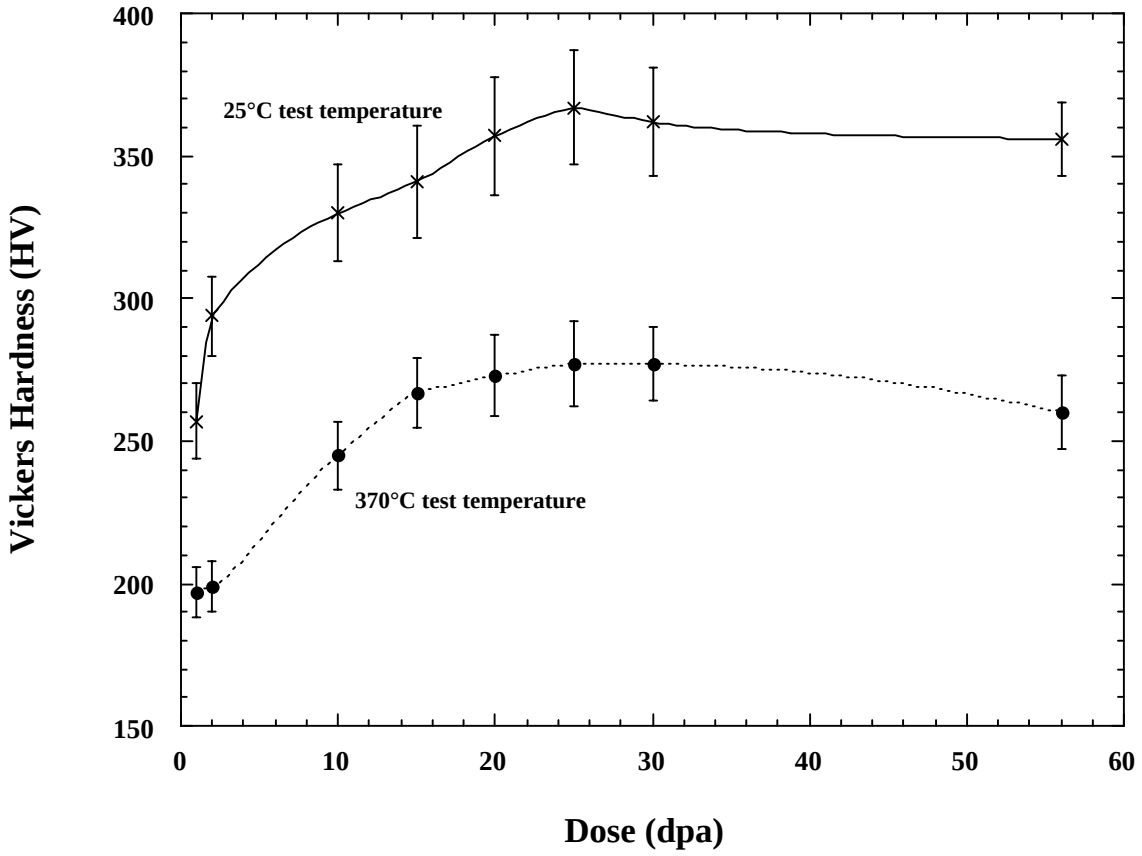

Figure 24. Hardness as a Function of Dose

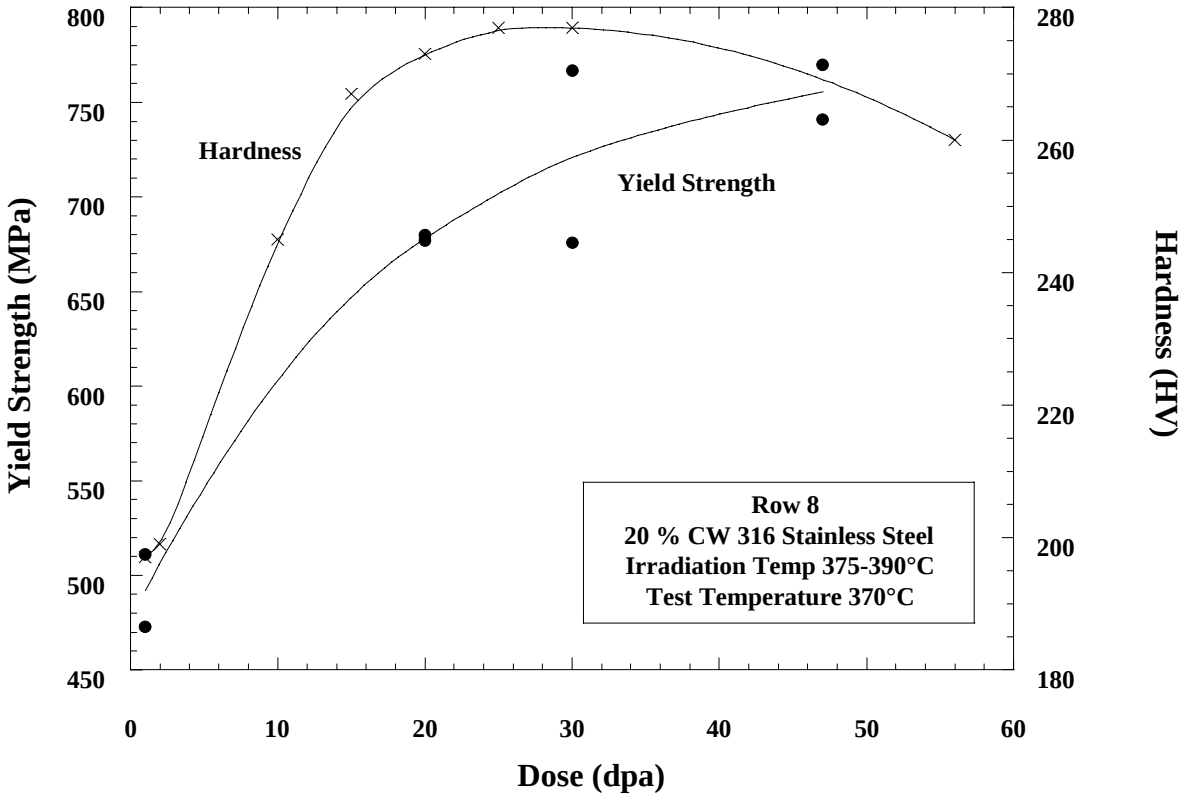

Figure 25. Comparison of Hardness and Yield Strength as a Function of Dose

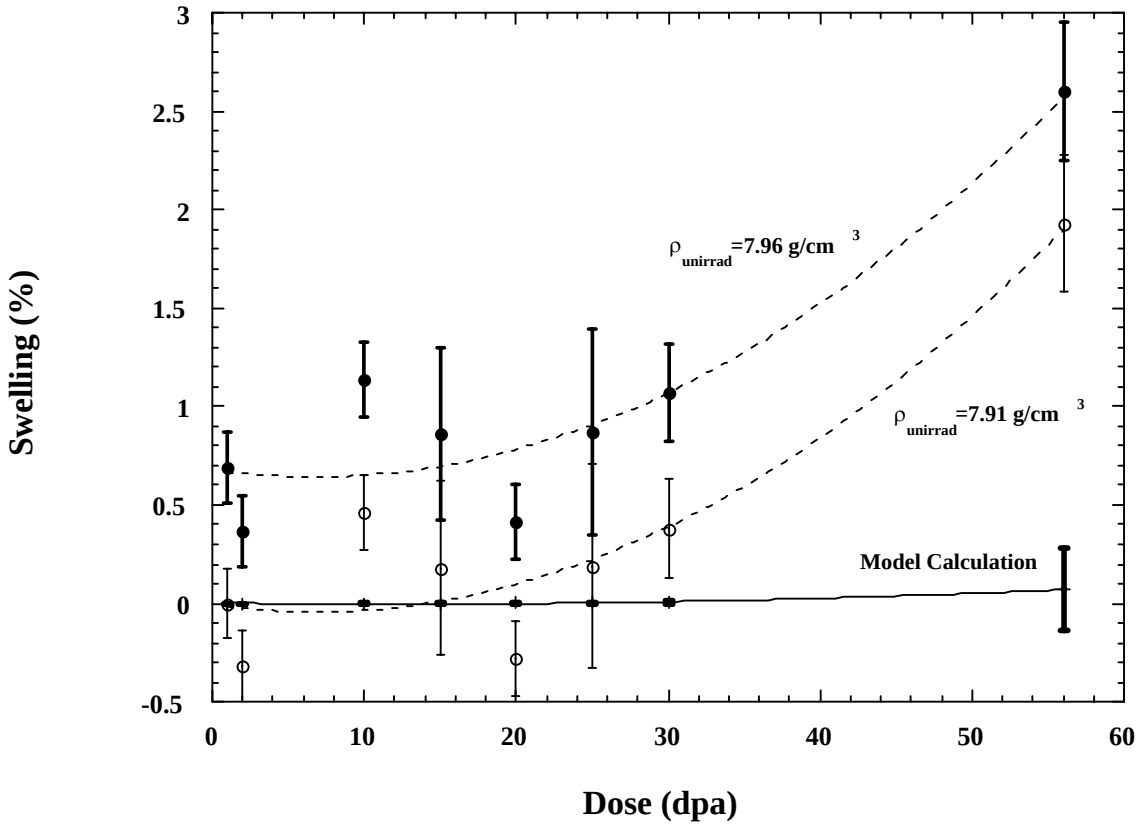

Figure 26. Swelling as a Function of Dose

(Error bars are the standard deviation of the measurements at each dose. Curve is best-fit polynomial.)

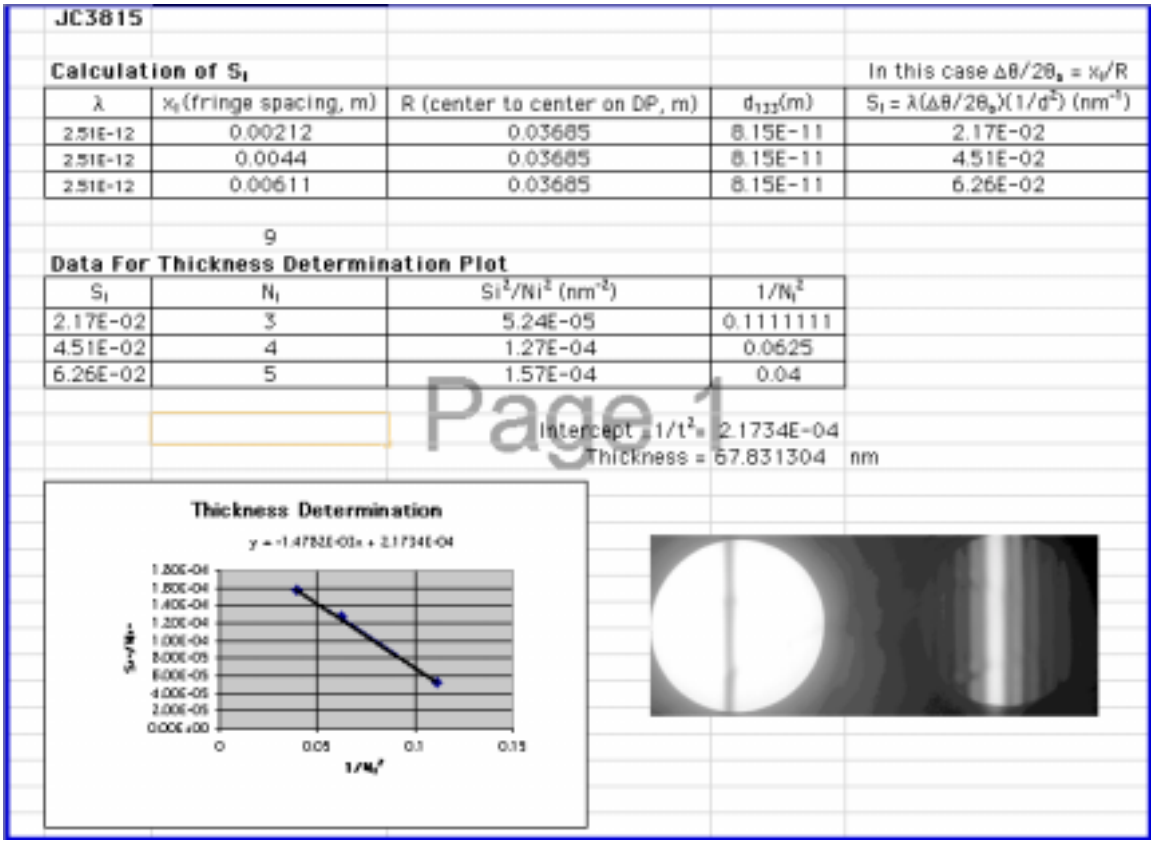

JC3815

Calculation of S_i

In this case $\Delta\theta/2\theta_B = x_0/R$

λ	x_0 (fringe spacing, m)	R (center to center on DP, m)	d_{111}(m)	$S_i = \lambda(\Delta\theta/2\theta_B)(1/d^2)$ (nm^{-1})
2.51E-12	0.00212	0.03685	8.15E-11	2.17E-02
2.51E-12	0.0044	0.03685	8.15E-11	4.51E-02
2.51E-12	0.00611	0.03685	8.15E-11	6.26E-02

9

Data For Thickness Determination Plot

S_i	N_i	Si^2/Ni^2 (nm^{-2})	$1/N_i^2$
2.17E-02	3	5.24E-05	0.1111111
4.51E-02	4	1.27E-04	0.0625
6.26E-02	5	1.57E-04	0.04

Intercept = $1/t^2$ = 2.1734E-04

Thickness = 67.831304 nm

Figure 27. Excel® Spreadsheet Used to Calculate Thickness from CBED Pattern

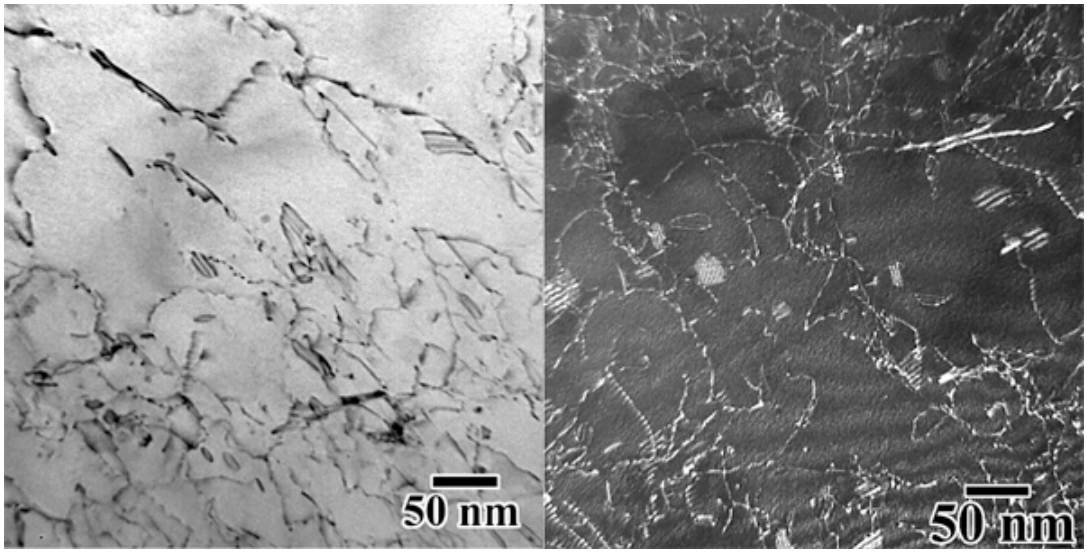

Figure 28. BF and WBDF Images of the Microstructure in the 316 SS Hex Duct Irradiated to 1 dpa at 370°C

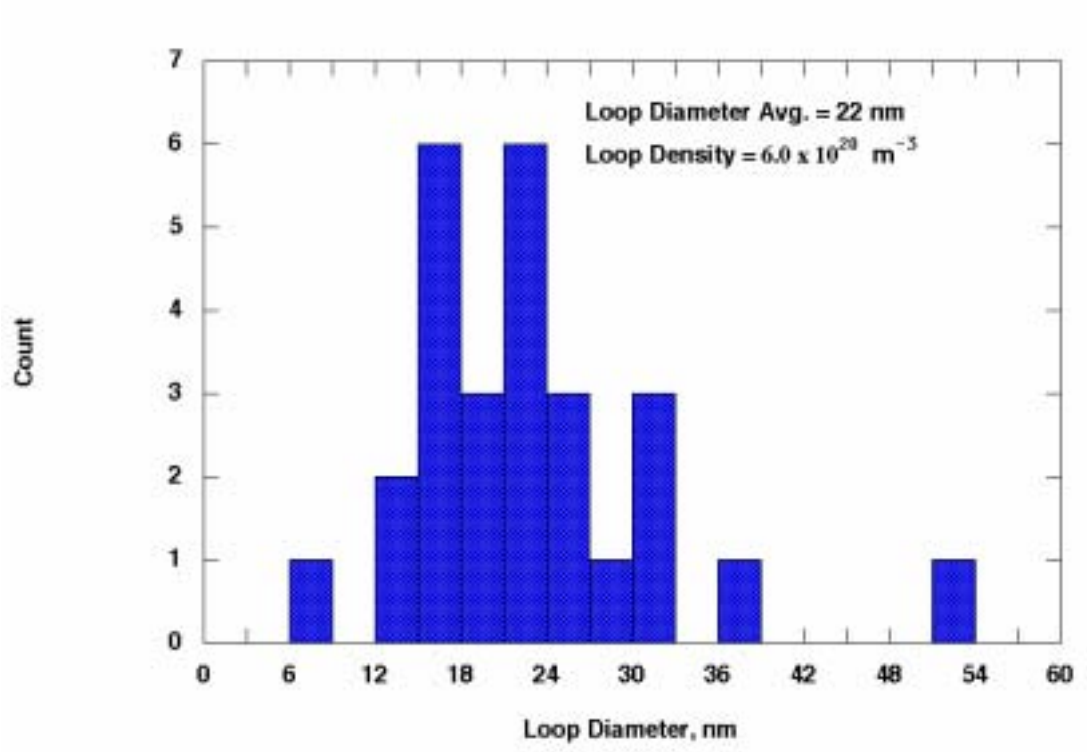

Figure 29. Dislocation Loop Diameter Distribution in the Microstructure of the 316 SS Hex Duct Irradiated to 1 dpa at 370°C

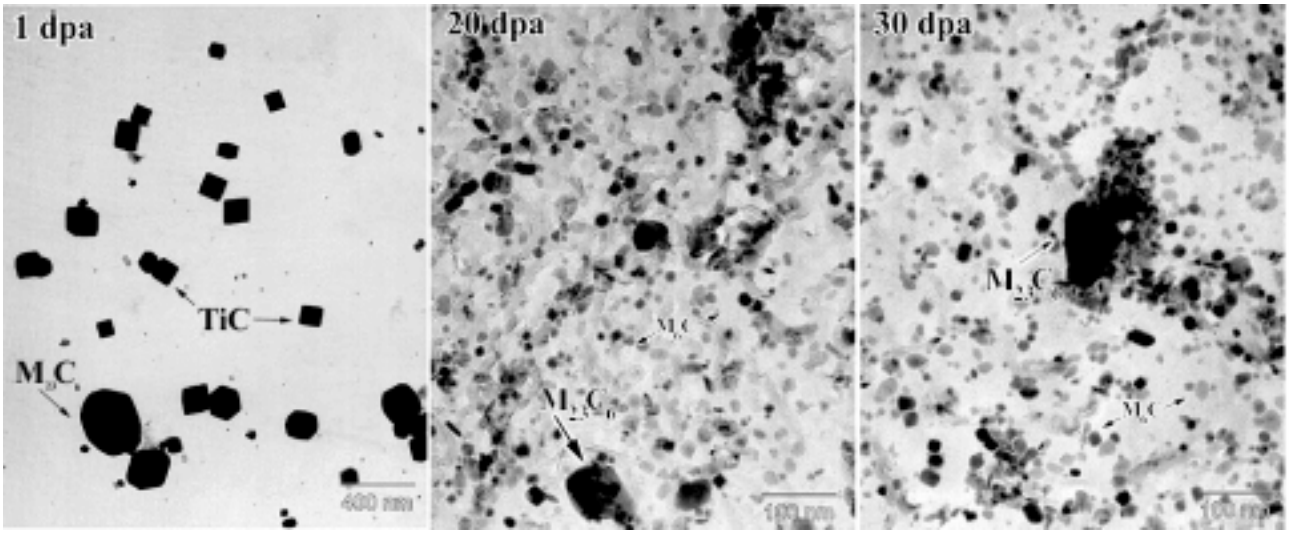

Figure 30. Extraction Replica Images of the 316 SS Hex Duct Material

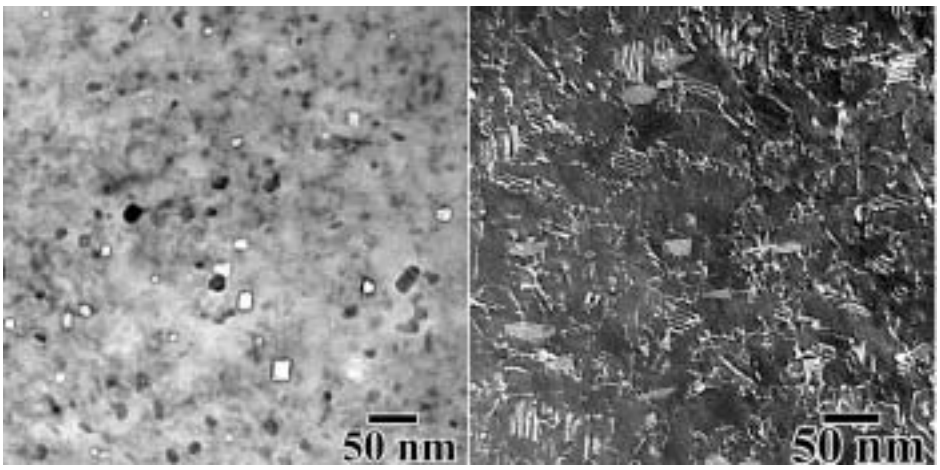

Figure 31. BF and WBDF Images of the Microstructure in the 316 SS Hex Duct Irradiated to 20 dpa

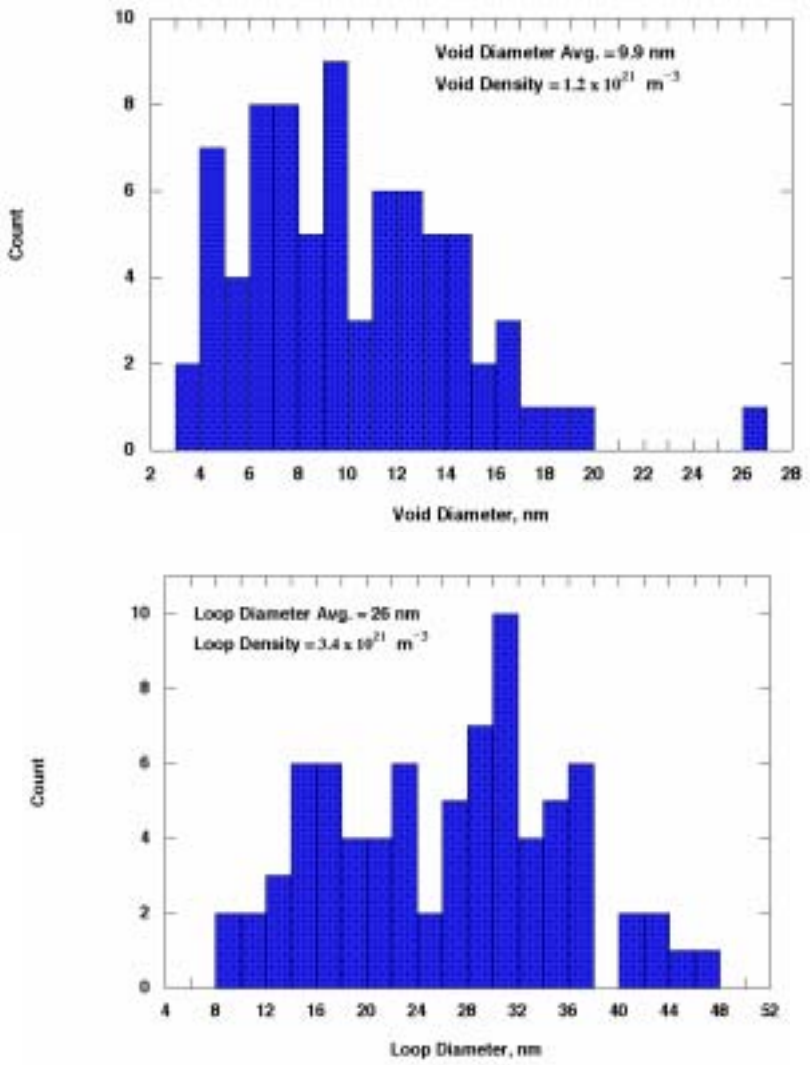

Figure 32. Void and Dislocation Loop Diameter Distributions in the Microstructure of the 316 SS Hex Duct Irradiated to 20 dpa

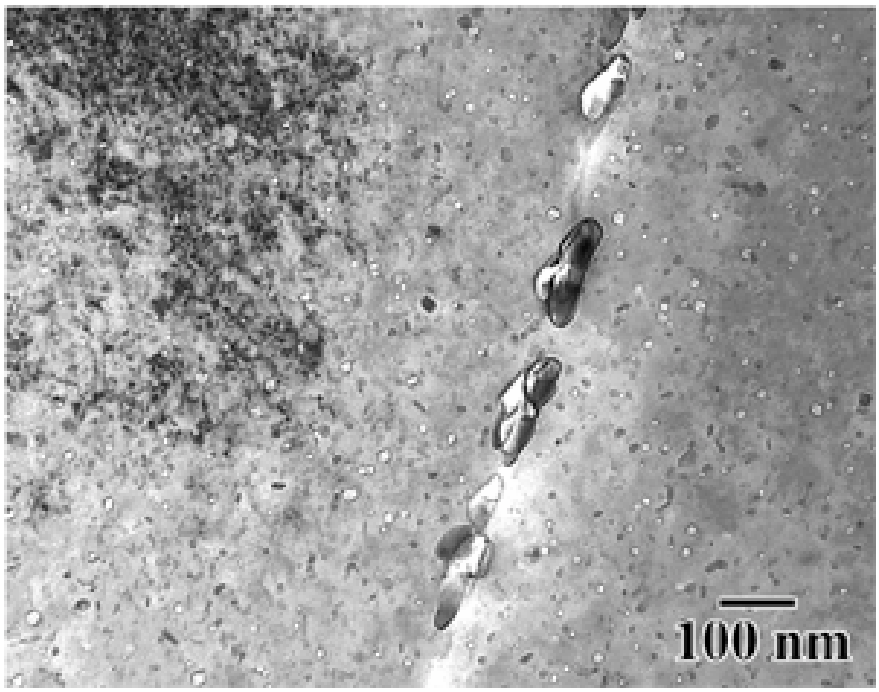

Figure 33. Grain Boundary Precipitates in 316 SS Hex Duct Irradiated to 20 dpa

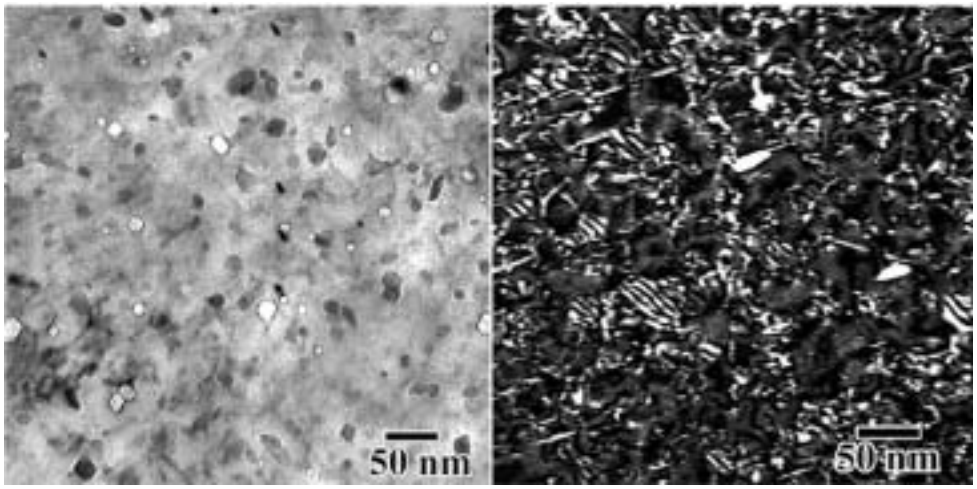

Figure 34. BF and WBDF Images of 316 SS Hex Duct Irradiated to 30 dpa

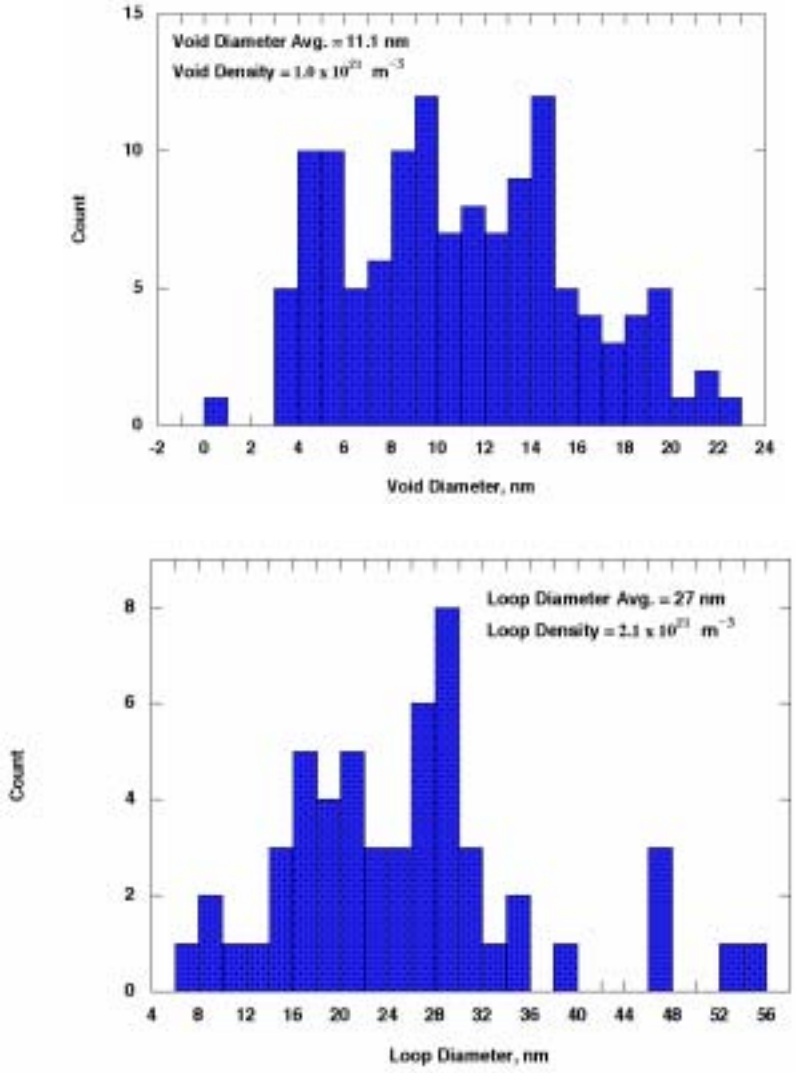

Figure 35. Void and Dislocation Loop Diameter Distributions in the Microstructure of the 316 SS Hex Duct Irradiated to 30 dpa

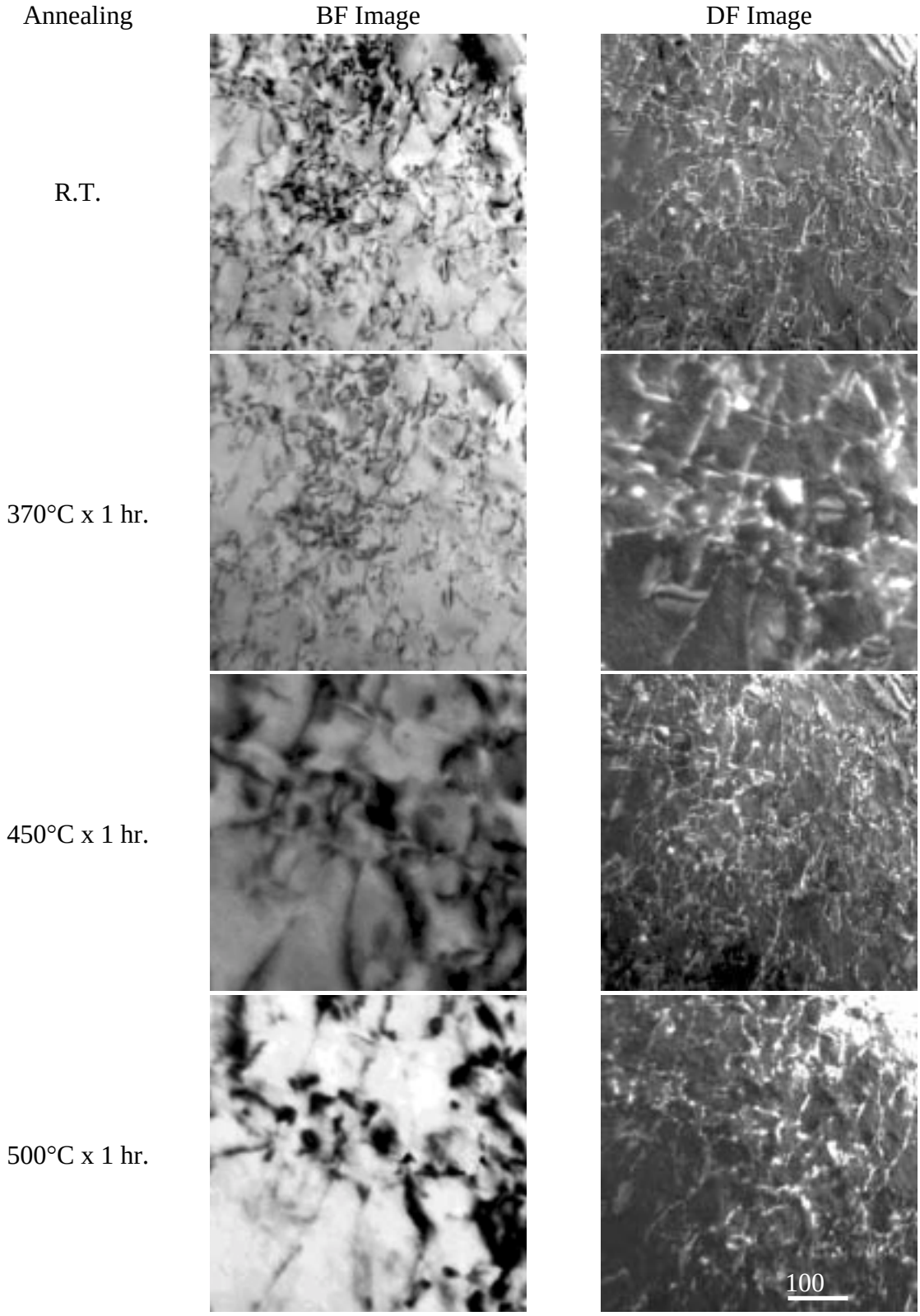

Figure 36. Microstructure of the Matrix after Annealing of 316SS Irradiated to 1 dpa

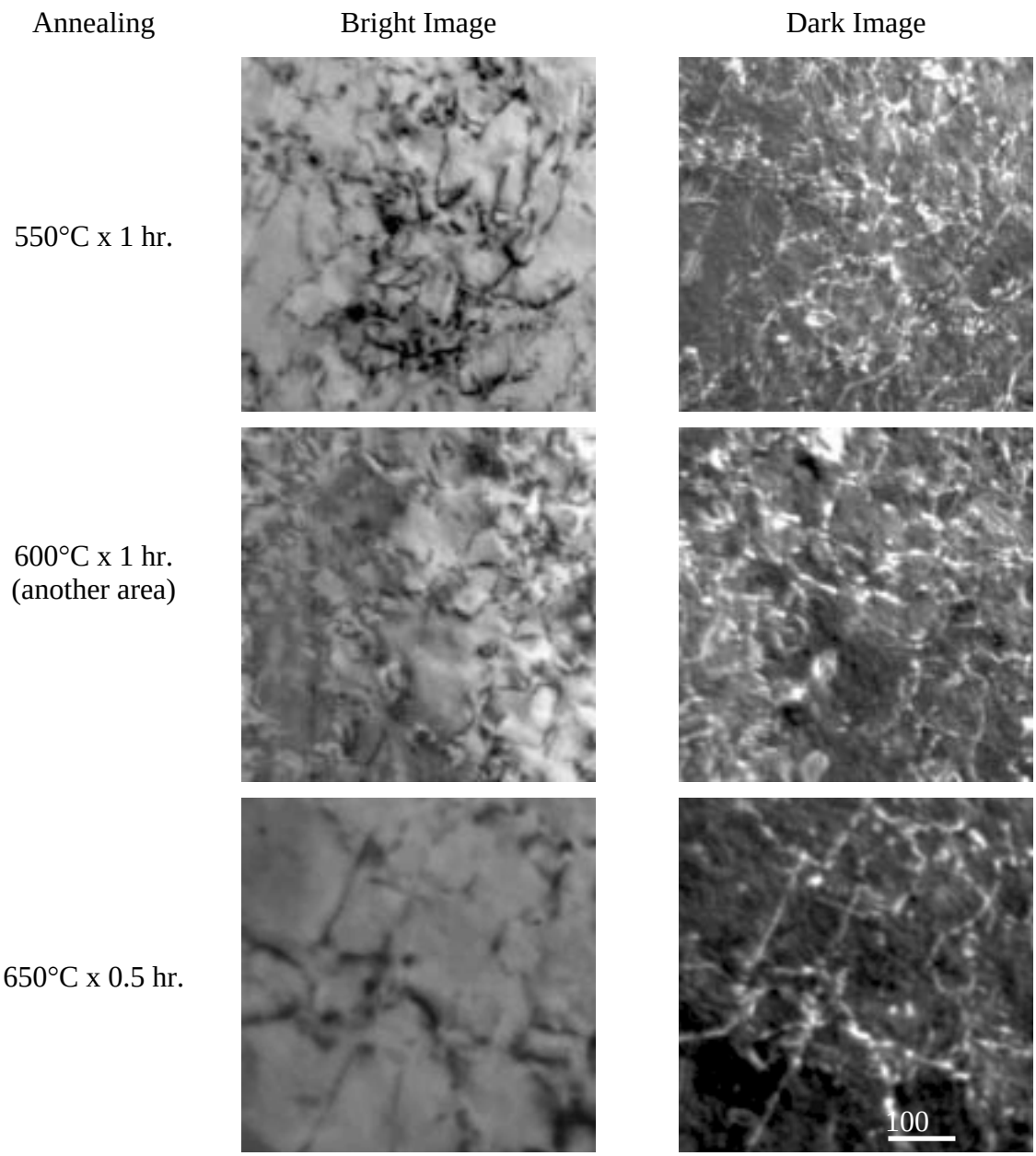

Figure 36 (continued). Microstructure of the Matrix after Annealing of 316SS Irradiated to 1 dpa

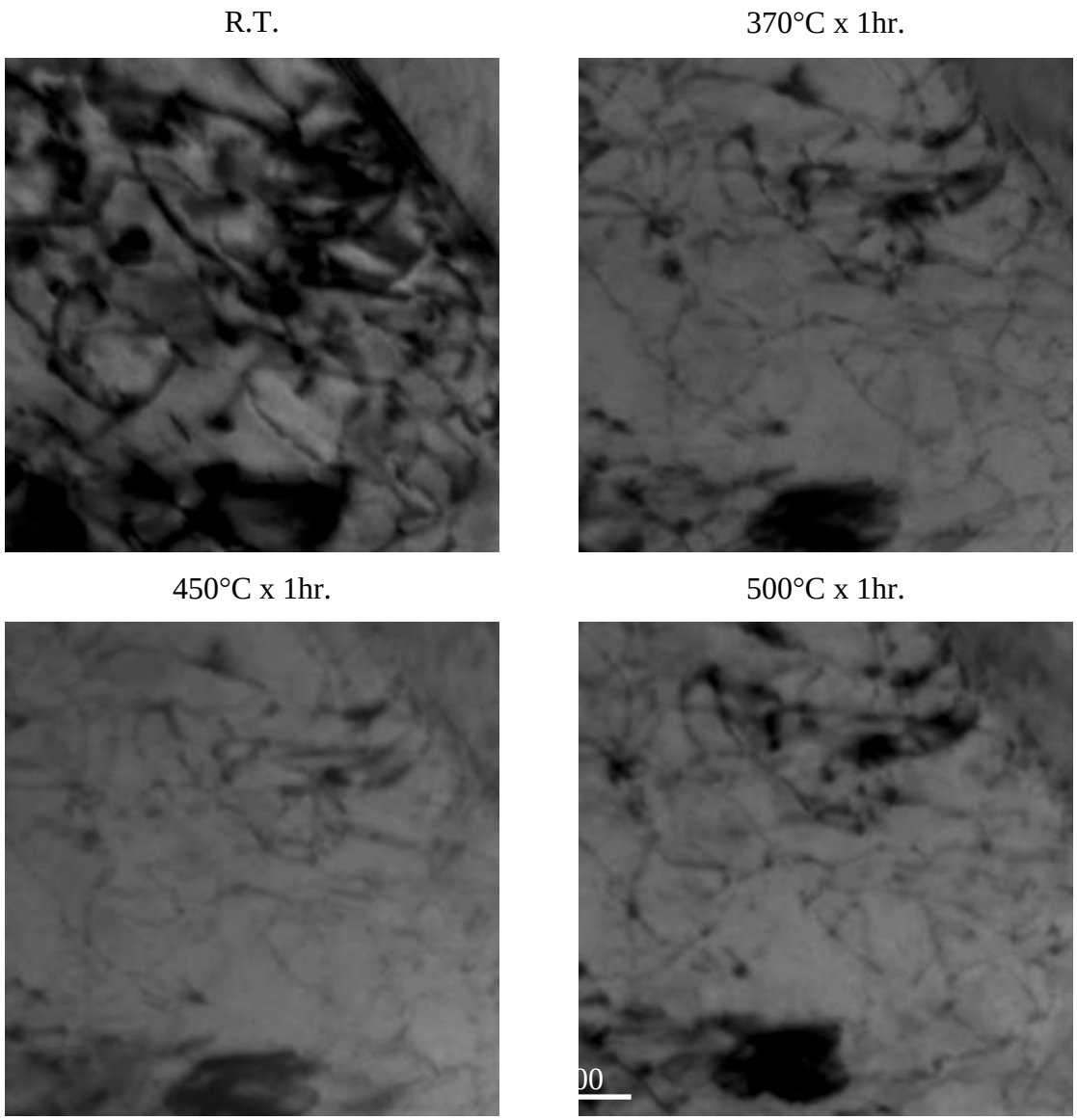

Figure 37. Microstructure Near the Grain Boundary after Annealing of 316SS Irradiated to 1 dpa

550°C x 1hr.

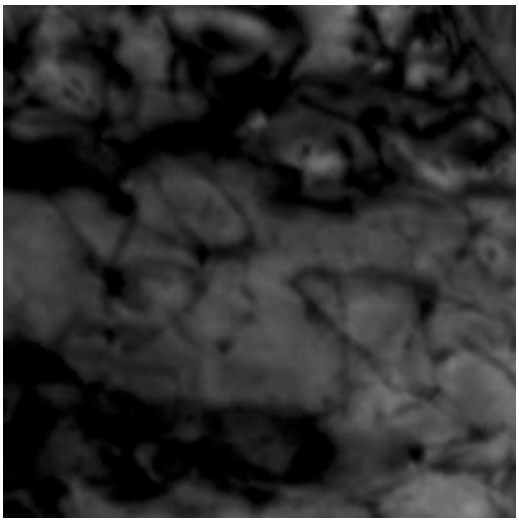

600°C x 1hr.

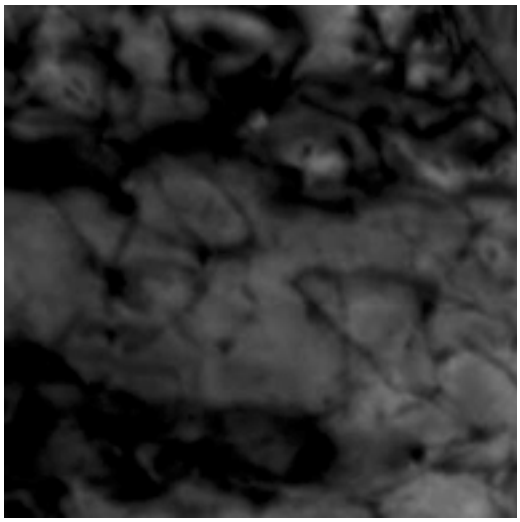

650°C x 0.5hr.

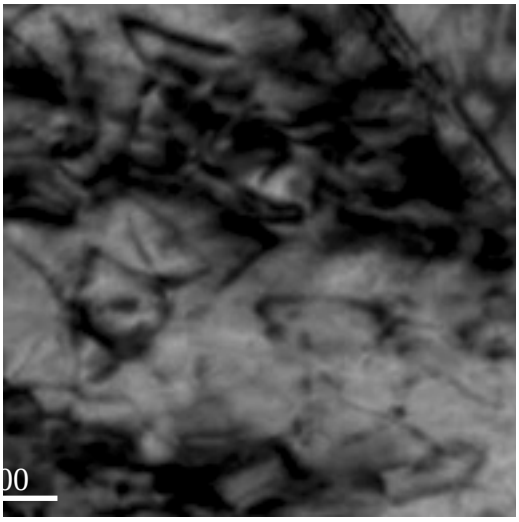

Figure 37 (continued). Microstructure Near the Grain Boundary After Annealing of 316SS Irradiated to 1 dpa

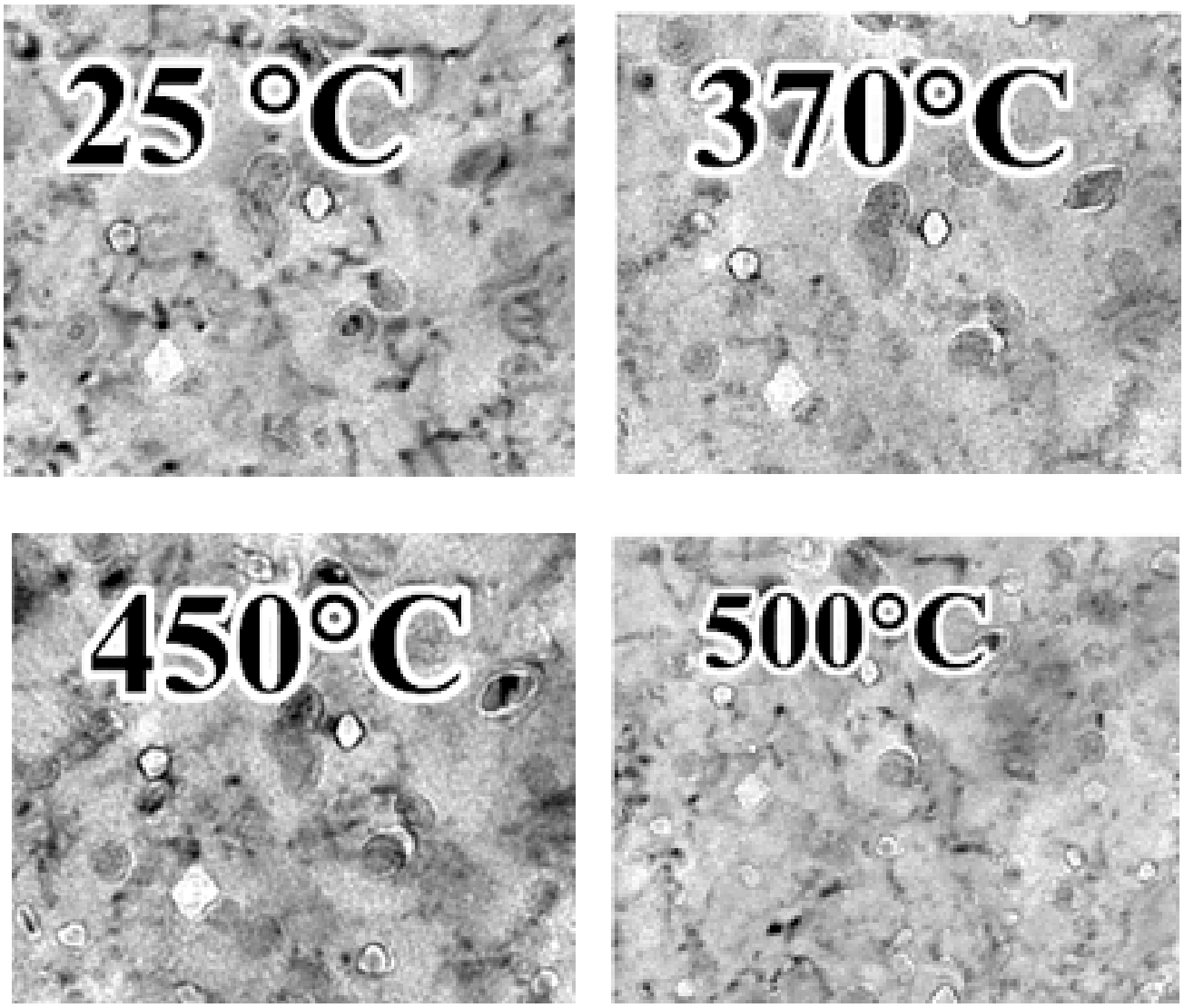

Figure 38. Microstructure as a Function of Annealing Temperature in the 316 SS Hex Duct Irradiated to 30 dpa

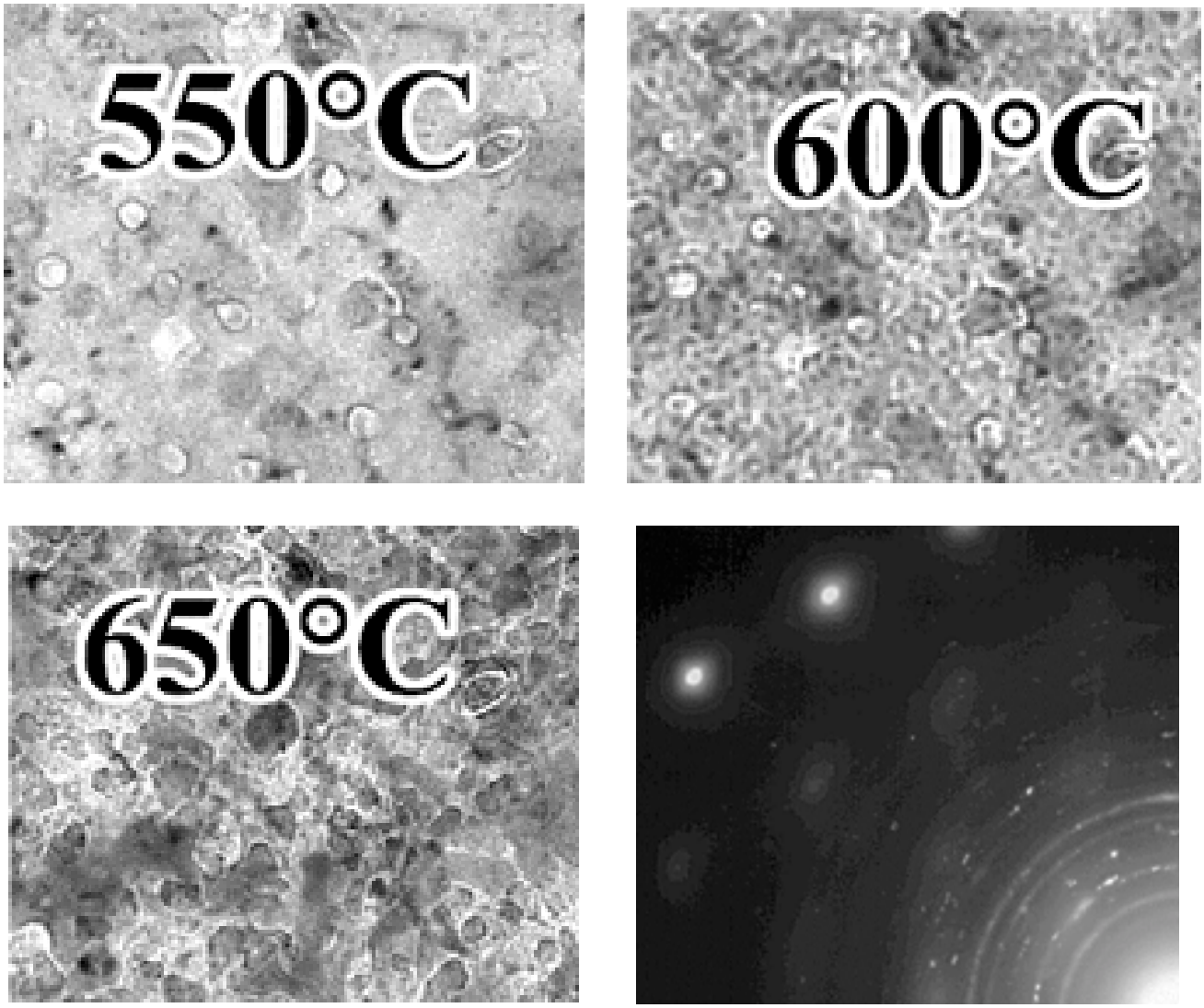

Figure 38 (continued). Microstructure as a Function of Annealing Temperature in the 316 SS Hex Duct irradiated to 30 dpa. Diffraction pattern illustrates oxide formation at 650°C.

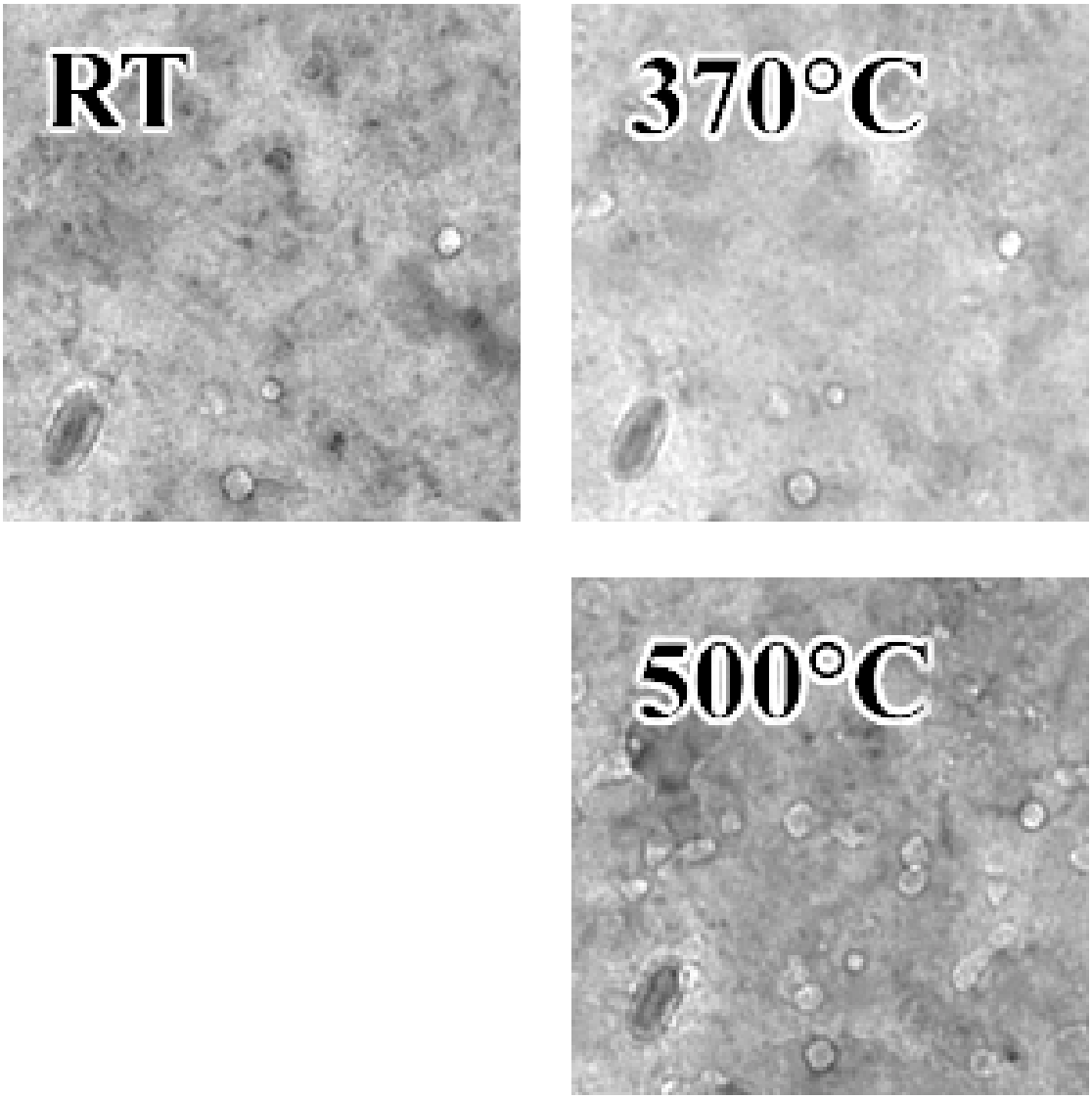

Figure 39. Microstructure of Near Grain Boundary Region as a Function of Annealing Temperature in the 316 SS Hex Duct Irradiated to 30 dpa

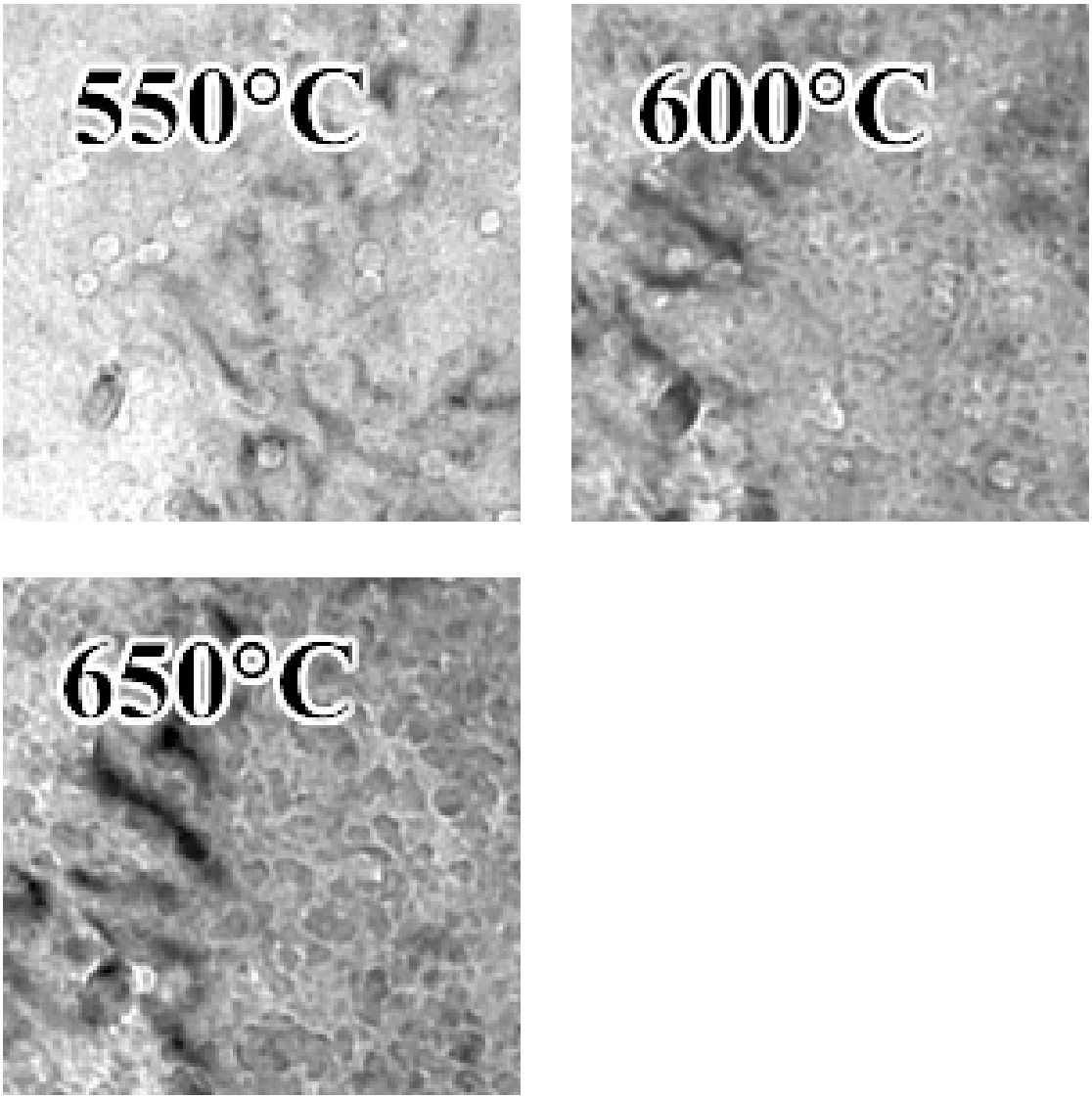

Figure 39 (continued). Microstructure of Near Grain Boundary Region as a Function of Annealing Temperature in the 316 SS Hex duct Irradiated to 30 dpa

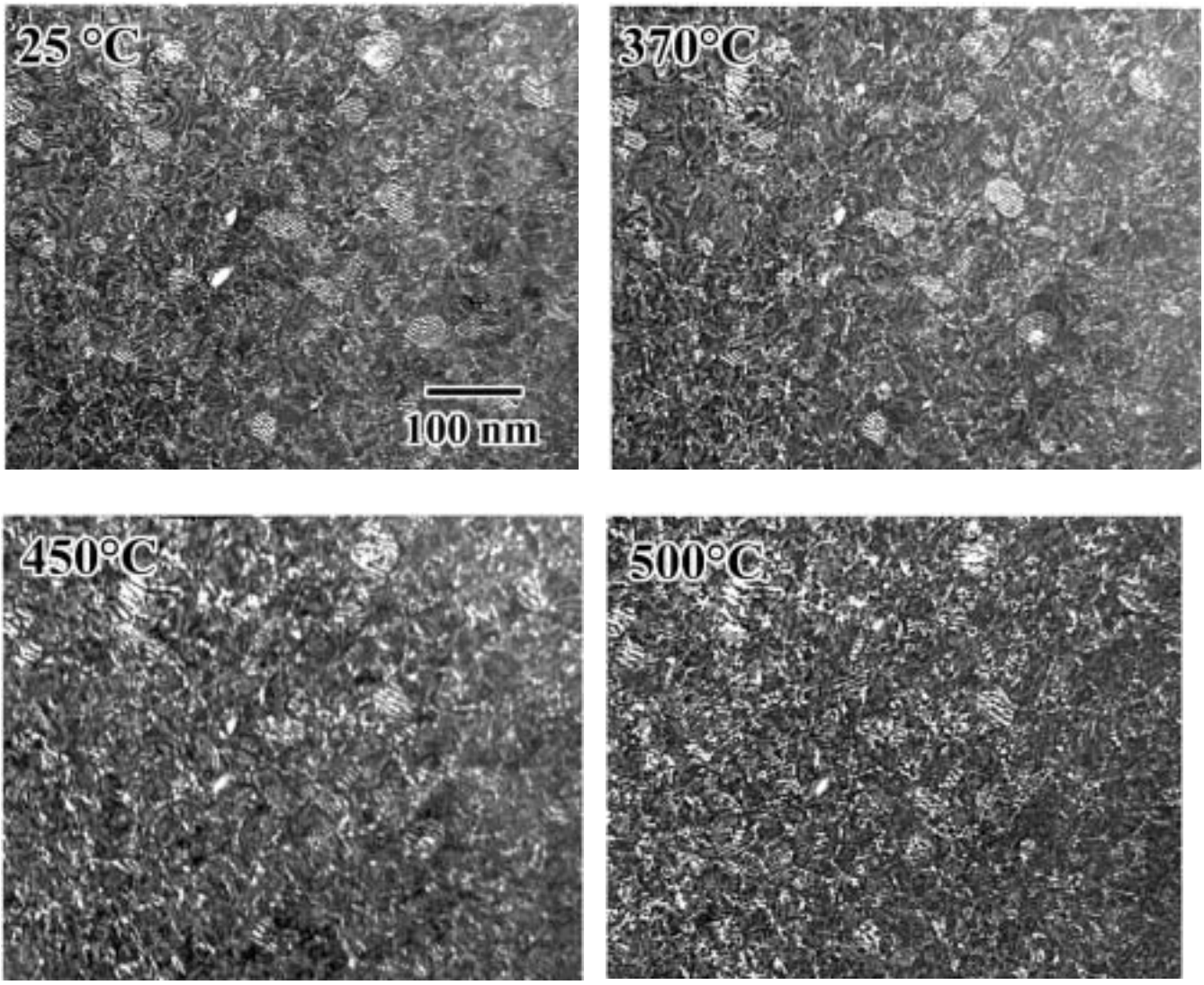

Figure 40. WBDF TEM Image of the Dislocation Structure as a Function of Annealing Temperature in the 316 SS Hex Duct Irradiated to 30 dpa

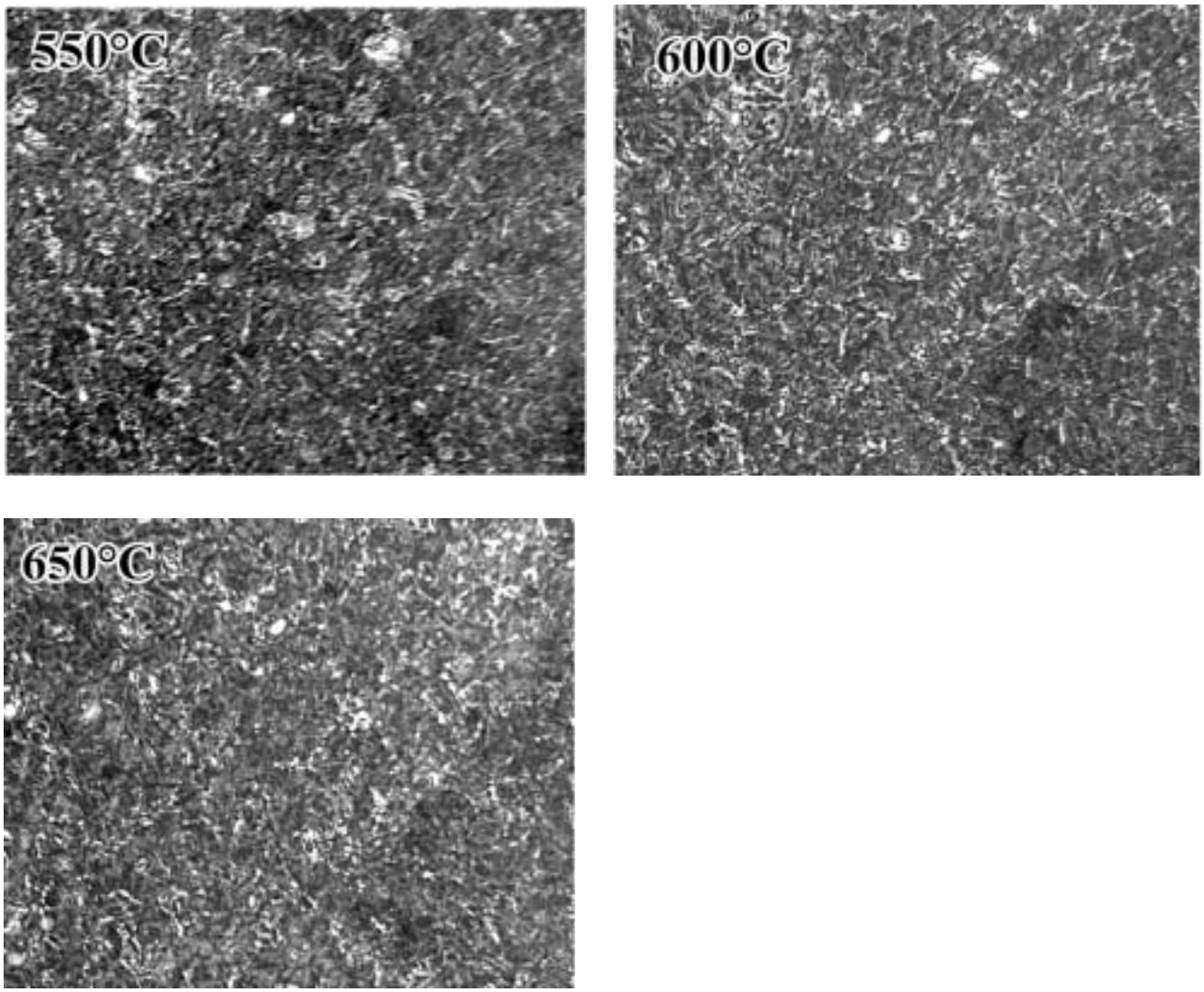

Figure 40 (continued). WBDF TEM Image of the Dislocation Structure as a Function of Annealing Temperature in the 316 SS Hex Duct Irradiated to 30 dpa

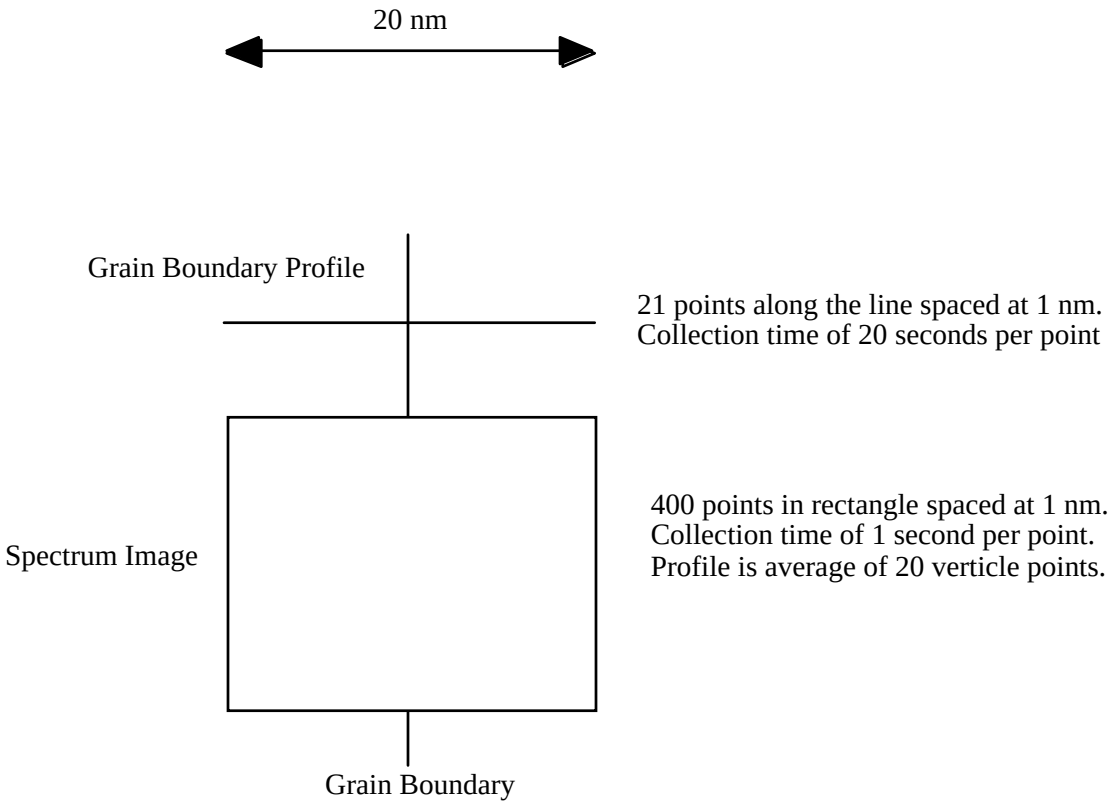

Figure 41. Spectrum Imaging and profile Techniques for Measuring Grain Boundary Segregation

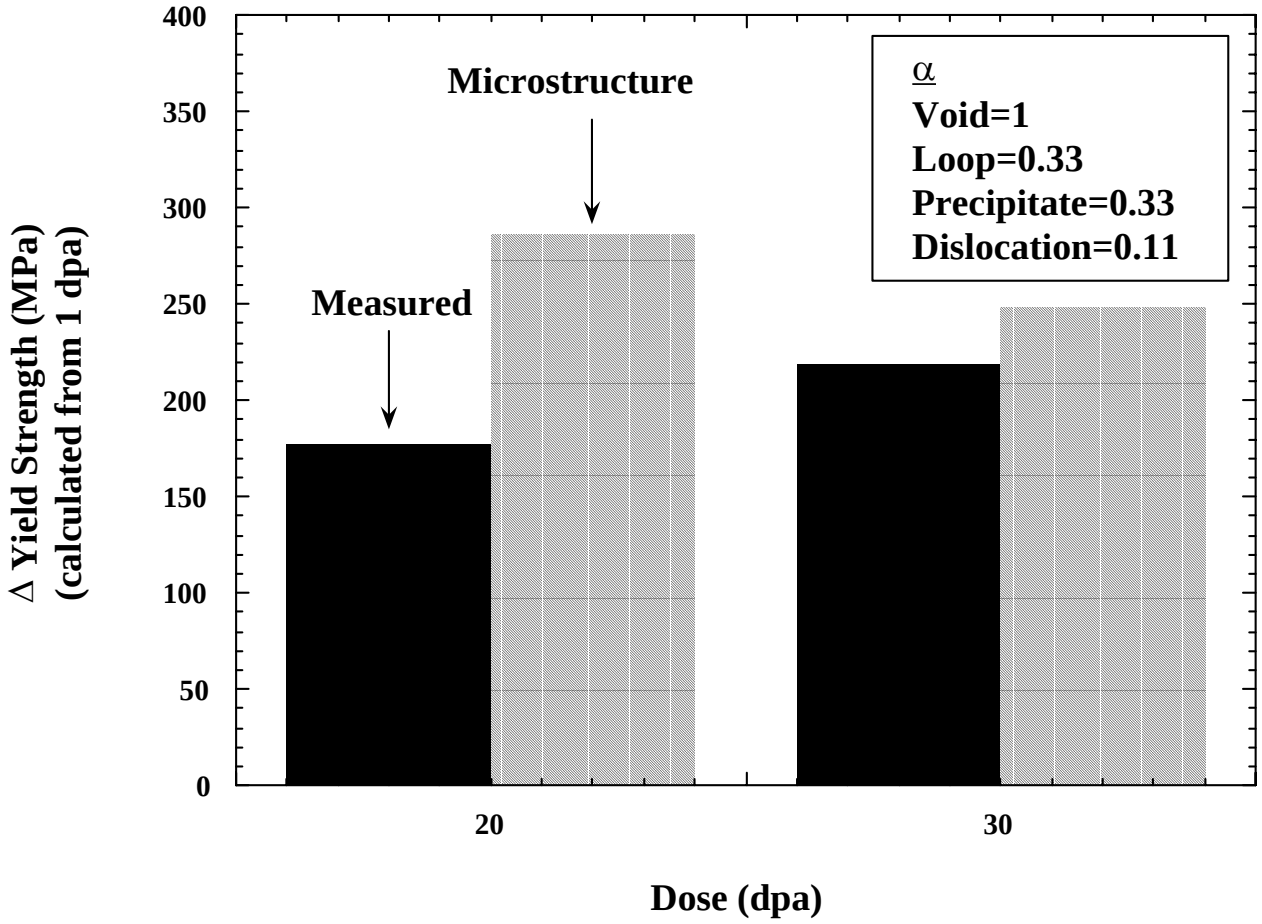

Figure 42. Comparison of Increase in Yield Strength and Increase in Yield Strength Estimated from Microstructural Features

Appendix A. Engineering Stress-Strain Curves for the Eight Tensile Tests

CRIEPI Tensile Test S1T1
YS: 677MPa; UTS: 810 MPa; UE: 2.9%; TE: 5.3%

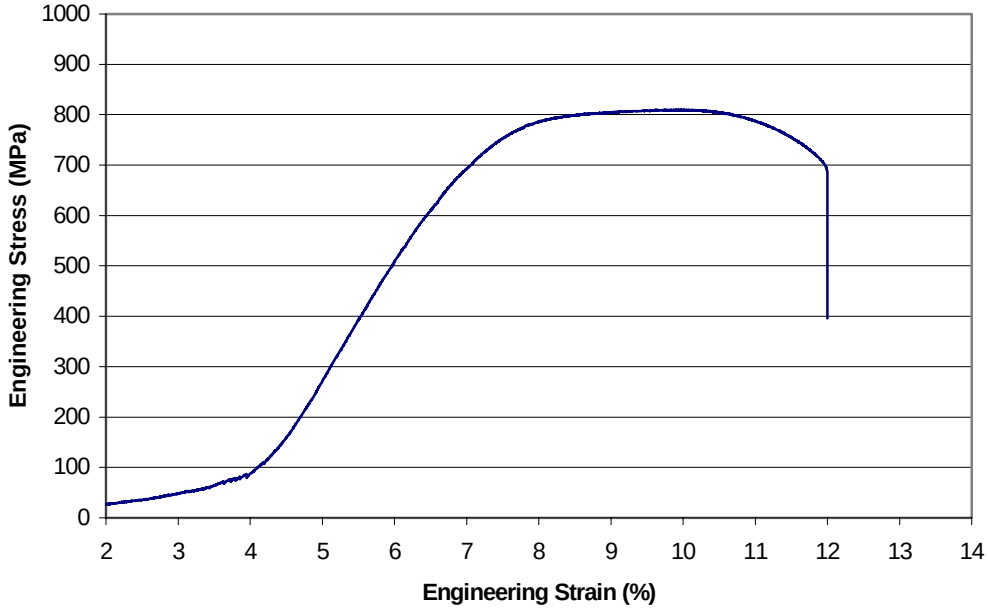

CRIEPI Tensile Test S1T2
YS: 680MPa; UTS: 824 MPa; UE: 3.5%; TE: 6.6%

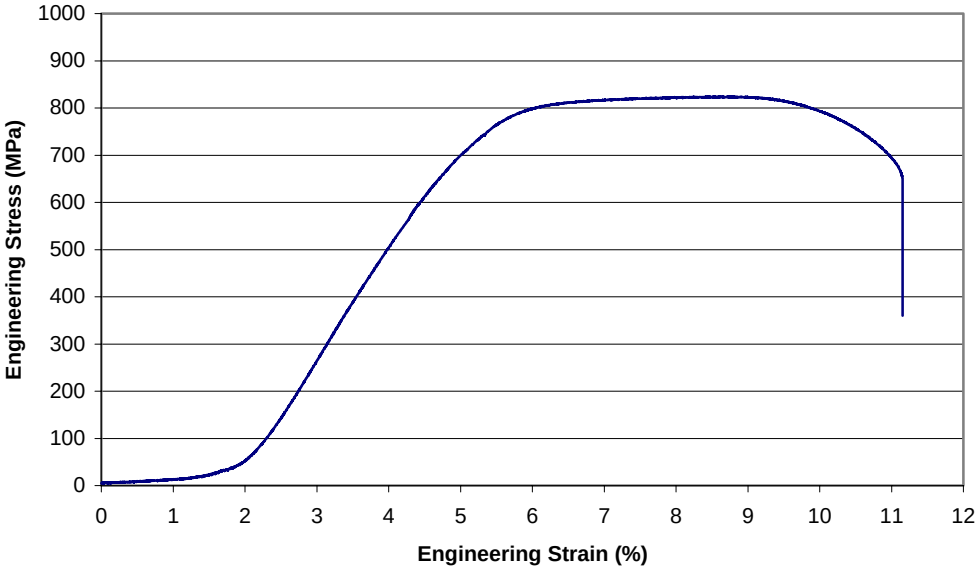

CRIEPI Tensile Test S1T3
YS: 767 MPa; UTS: 805 MPa; UE: 2.3%; TE:4.8%

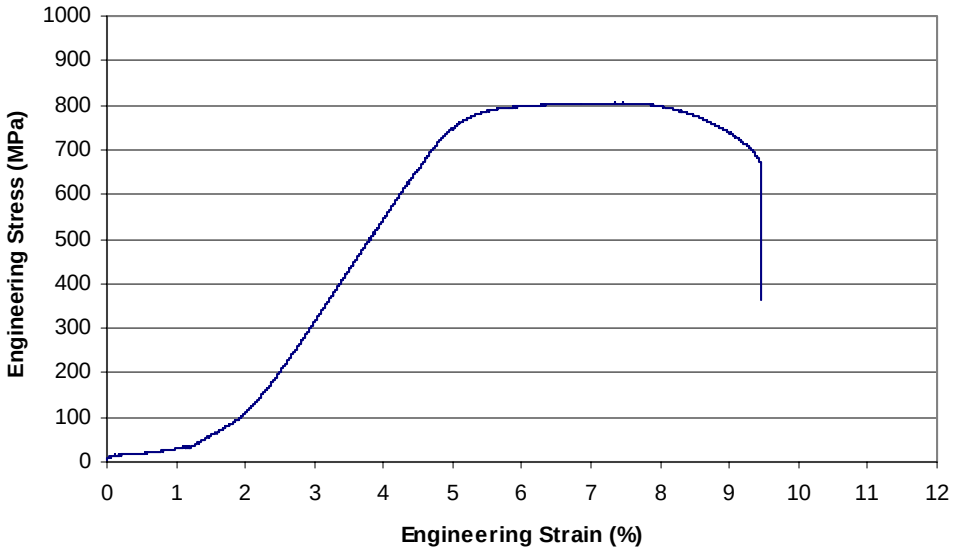

CRIEPI Tensile Test S1T4
YS: 676 MPa; UTS: 805 MPa; UE: 2.3%; TE:5.1%

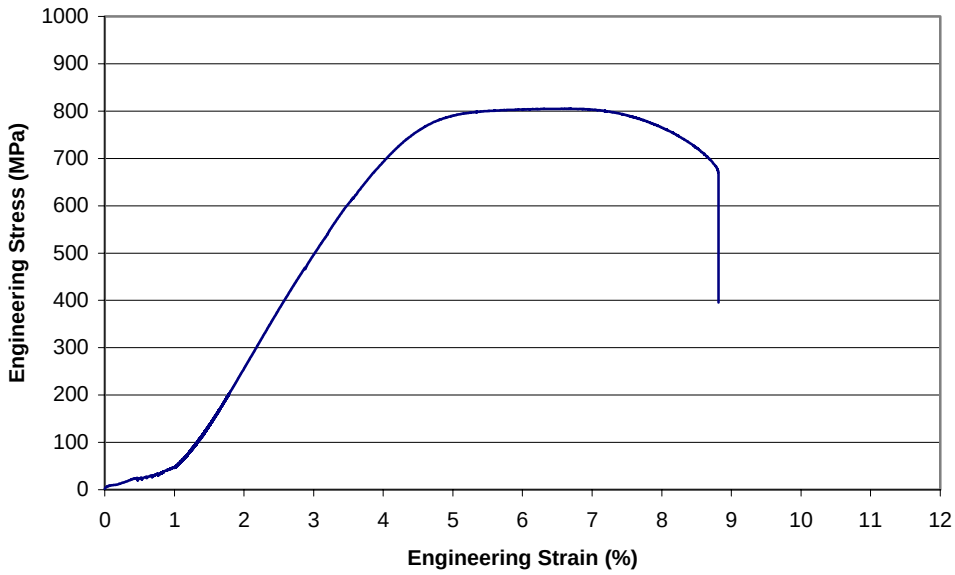

CRIEPI Tensile Test S1T5
YS: 741 MPa; UTS: 790 MPa; UE: 0.9%; TE:2.8%

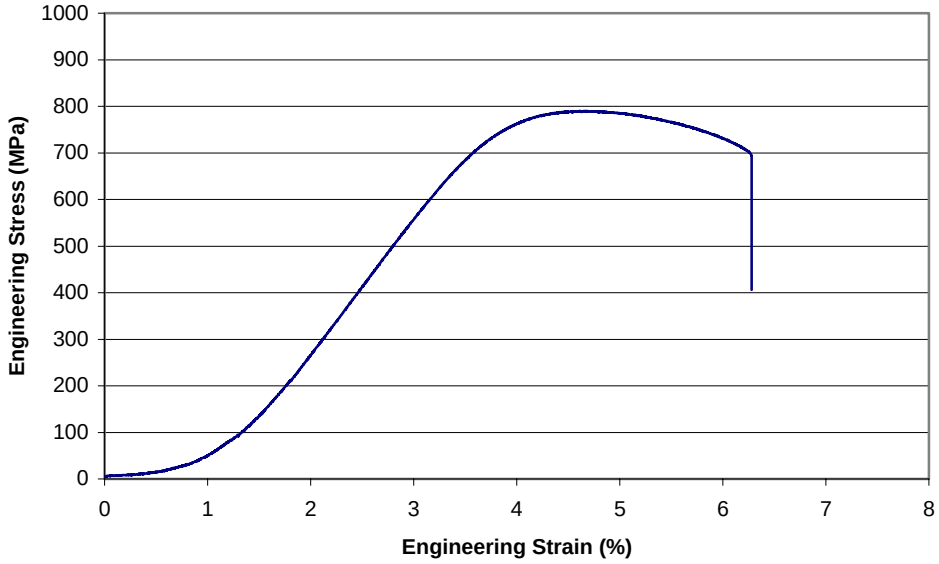

CRIEPI Tensile Test S1T6
YS: 770 MPa; UTS: 787 MPa; UE: 0.5%; TE:1.9%

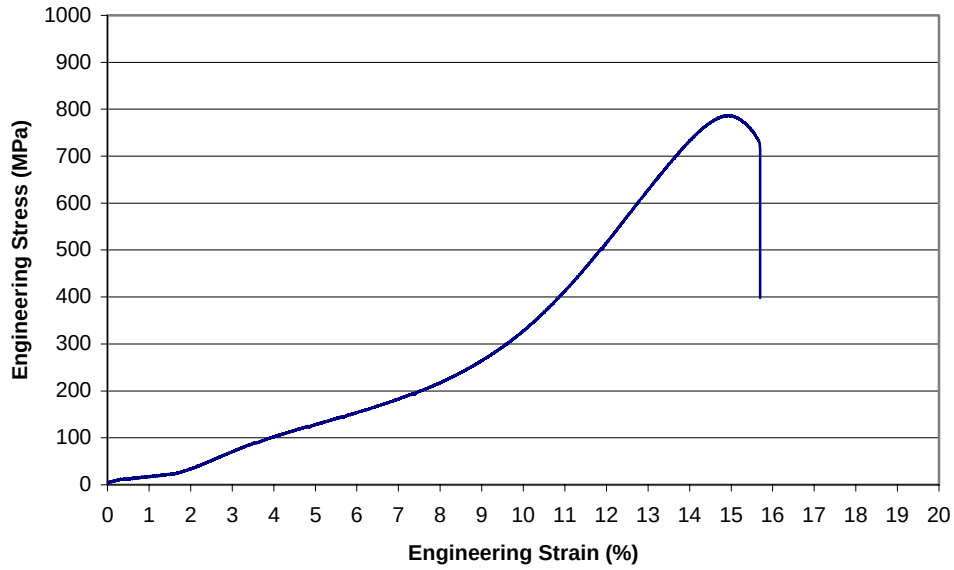

CRIEPI Tensile Test S2T1
YS: 511 MPa; UTS: 628 MPa; UE: 10.2%; TE: 16.5%

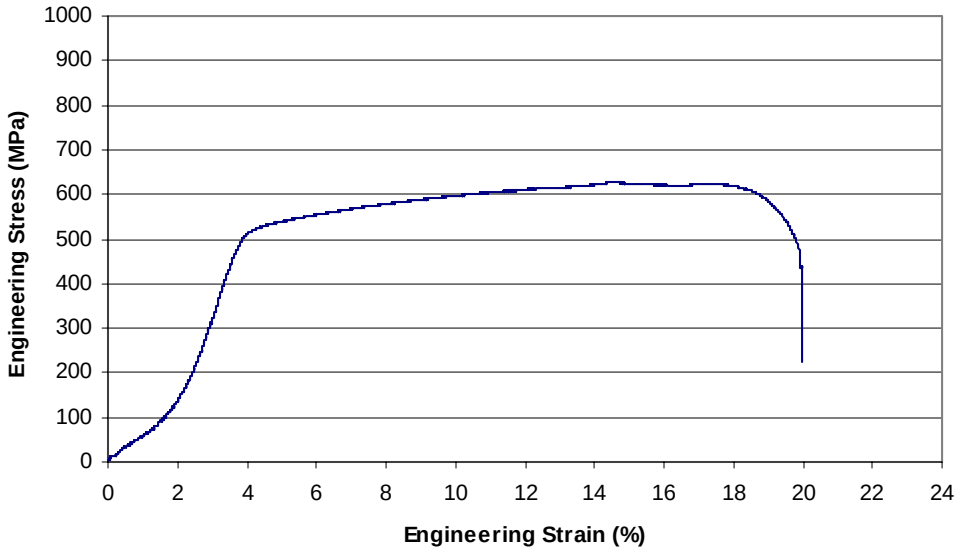

CRIEPI Tensile Test S2T2
YS: 473 MPa; UTS: 597 MPa; UE: 12.0%; TE: 15.4%

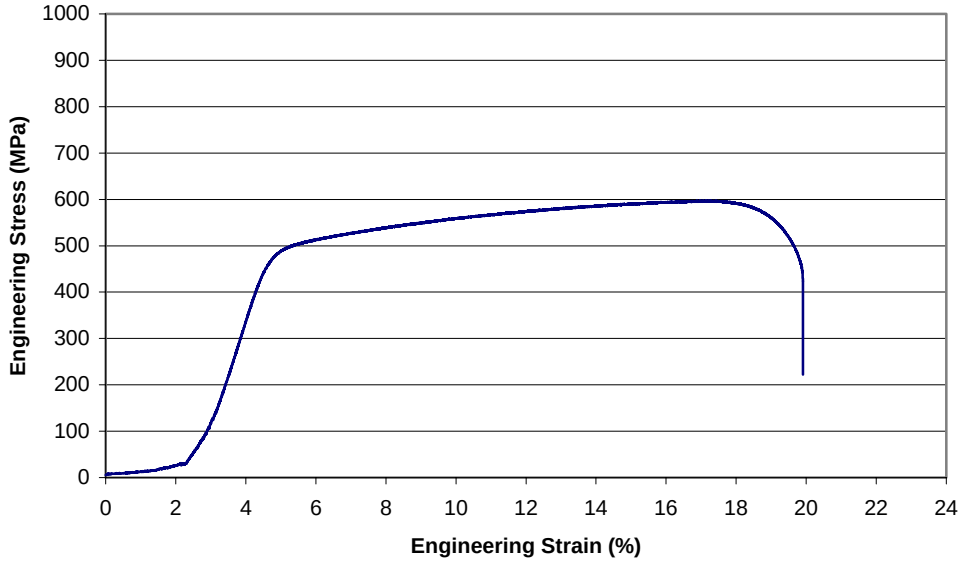

Appendix B. Grain Boundary Composition Measurements

B1. Grain Boundary Composition Measurements at 1 dpa

Table B1. Grain boundary composition measurement

	Fe	Cr	Ni	Mo	Si
Grain Boundary	61.7	20.1	13.4	4.1	0.7
Matrix	65.7	18.4	13.5	1.7	0.6

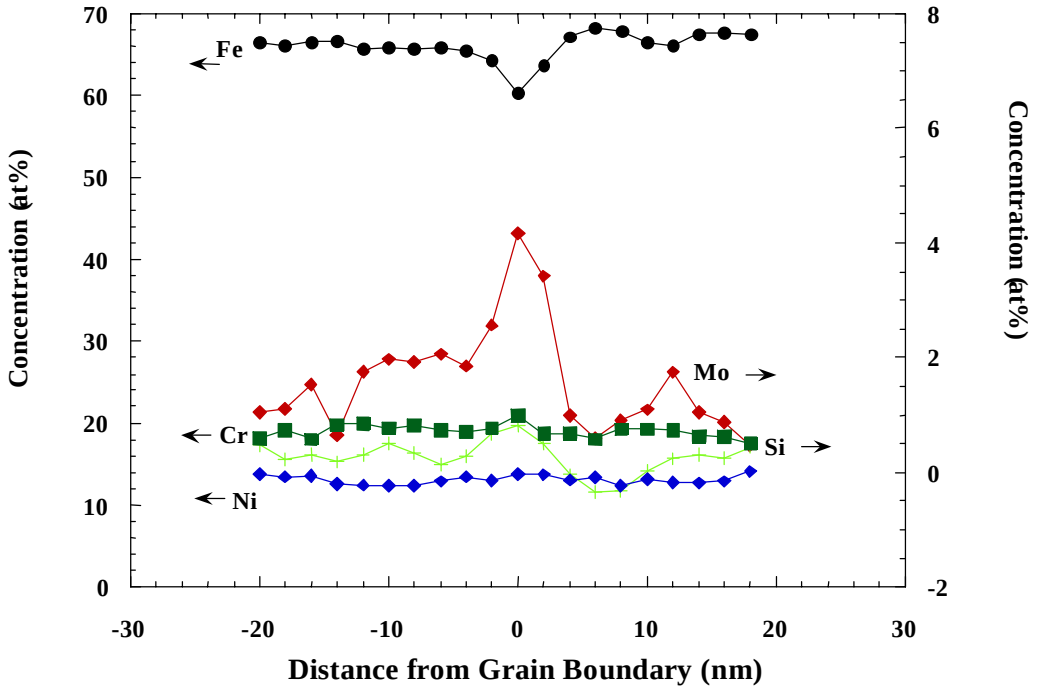

Figure B1. Grain boundary profile 002

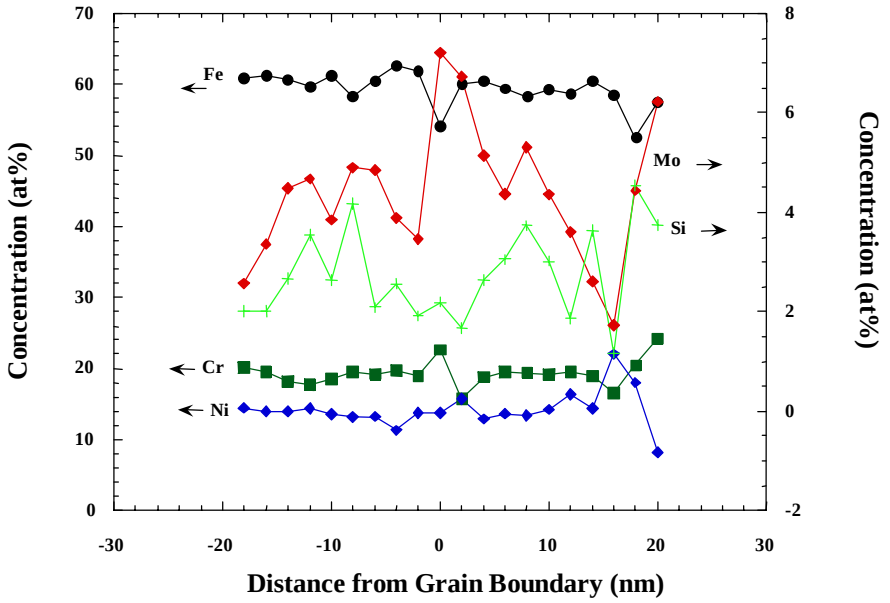

Figure B2. Grain boundary profile 006

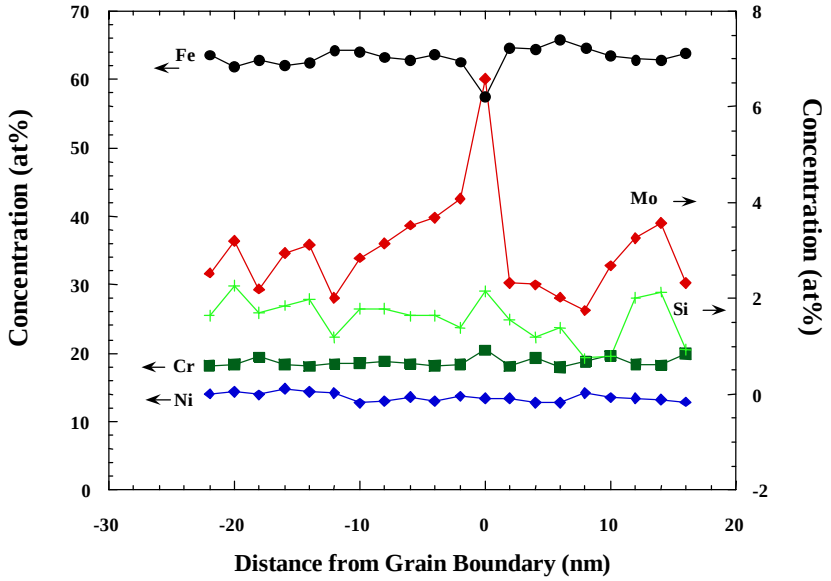

Figure B3. Grain Boundary Profile 007

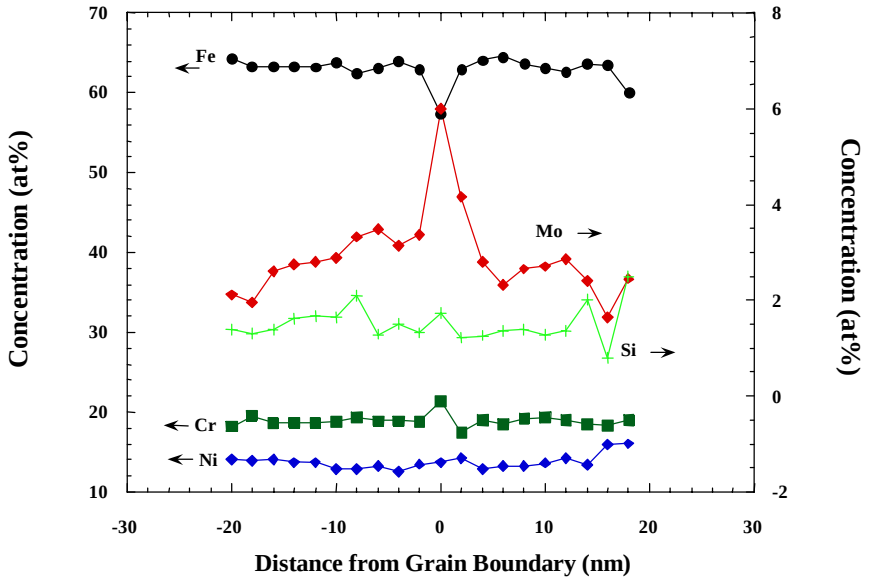

Figure B4 . Grain Boundary Profile using the average of the three profiles from Figures B1-B3

B2. Grain Boundary Composition Measurements at 20 dpa

Table B2. Grain boundary 1 composition measurements (at%)

	Fe	Cr	Ni	Mo	Si	Comment
Spectra						
Grain Boundary	67.7	16.7	13.9	1.5	0.2	Poor diffraction contrast
Grain Boundary	65.4	13.8	15.8	3.2	1.9	Good diffraction contrast
Grain Boundary	68.8	15.8	12.7	1.8	1.0	Thicker area
Grain Boundary (Prof)	66.0	11.8	18.0	2.9	1.2	
Grain Boundary (Prof)	67.8	13.6	15.1	2.2	1.3	
Grain Boundary (SI)	57.7	14.1	22.2	3.4	2.5	Thinner area than profiles
Average Grain Boundary	65.6	14.3	16.3	2.5	1.4	
Matrix	69.4	17.3	11.3	1.7	0.4	
Matrix	65.9	18.4	14.2	1.2	0.2	
Average Matrix	67.6	17.8	12.7	1.5	0.3	
Average Segregation (matrix-GB)	-0.5	-3.5	2.4	0.8	0.8	
Maximum Segregation (avg matrix-GB)	-9.9	-6	+9.5	+1.9	+2.2	

Prof=from a profile measurement
SI=from a spectrum image measurement

Table B3. Grain boundary 2 composition measurements (at%)

	Fe	Cr	Ni	Mo	Si	Comments
Spectra						
Grain Boundary	60.2	15.0	24.1	0.0	0.6	
Grain Boundary	64.5	17.6	16.7	0.4	0.8	Thicker area
Grain Boundary	65.5	11.7	21.6	0.7	0.6	
Grain Boundary	69.4	11.5	18.4	0.0	0.8	Thicker area
Grain Boundary (Prof)	65.6	14.1	17.4	2.4	0.5	
Grain Boundary (Prof)	65.6	11.7	22.0	0.0	0.7	
Grain Boundary (Prof)	64.2	15.3	18.5	2.0	0.0	
Grain Boundary (Prof)	68.0	13.6	16.3	1.5	0.6	
Grain Boundary (SI)	62.3	13.4	21.1	2.1	1.1	
Average Grain Boundary	65.0	13.8	19.6	1.0	0.6	
Matrix	69.7	16.7	11.0	2.3	0.4	
Matrix	63.5	19.0	14.7	2.4	0.4	
Average Matrix	66.6	17.9	12.8	2.3	0.4	
Average Segregation (matrix-GB)	-1.6	-4.1	6.7	-1.3	0.2	
Maximum Segregation (avg matrix-GB)	-6.4	-6.4	+11.3	-2.3	+0.4	

Prof=from a profile measurement
SI=from a spectrum image measurement

Table B4. 20 dpa All measurements (at%)

	Fe	Cr	Ni	Mo	Si
Spectra					
Grain Boundary	67.7	16.7	13.9	1.5	0.2
Grain Boundary	65.4	13.8	15.8	3.2	1.9
Grain Boundary		15.8	12.7	1.8	1
Grain Boundary	60.2	15	24.1	0	0.6
Grain Boundary	64.5	17.6	16.7	0.4	0.8
Grain Boundary	65.5	11.7	21.6	0.7	0.6
Grain Boundary	69.4	11.5	18.4	0	0.8
Grain Boundary (Prof)	66.0	11.8	18.0	2.9	1.2
Grain Boundary (Prof)	67.8	13.6	15.1	2.2	1.3
Grain Boundary (Prof)	65.6	14.1	17.4	2.4	0.5
Grain Boundary (Prof)	65.6	11.7	22.0	0.0	0.7
Grain Boundary (Prof)	64.2	15.3	18.5	2.0	0.0
Grain Boundary (Prof)	68.0	13.6	16.3	1.5	0.6
Grain Boundary (SI)	57.7	14.1	22.2	3.4	2.5
Grain Boundary (SI)	62.3	13.4	21.1	2.1	1.1
Average Grain Boundary	65.2	14.0	18.3	1.6	0.9
Matrix	69.4	17.3	11.3	1.7	0.4
Matrix	65.9	18.4	14.2	1.2	0.2
Matrix	69.7	16.7	11.0	2.3	0.4
Matrix	63.5	19.0	14.7	2.4	0.4
Average Matrix	67.1	17.9	12.8	1.9	0.4
Average Segregation (matrix-GB)	-1.9	-3.9	+5.5	-0.3	+0.6
Maximum Segregation (avg matrix-GB)	-9.4	-6.4	+11.3	-1.9	+2.1

Prof=from a profile measurement
SI=from a spectrum image measurement

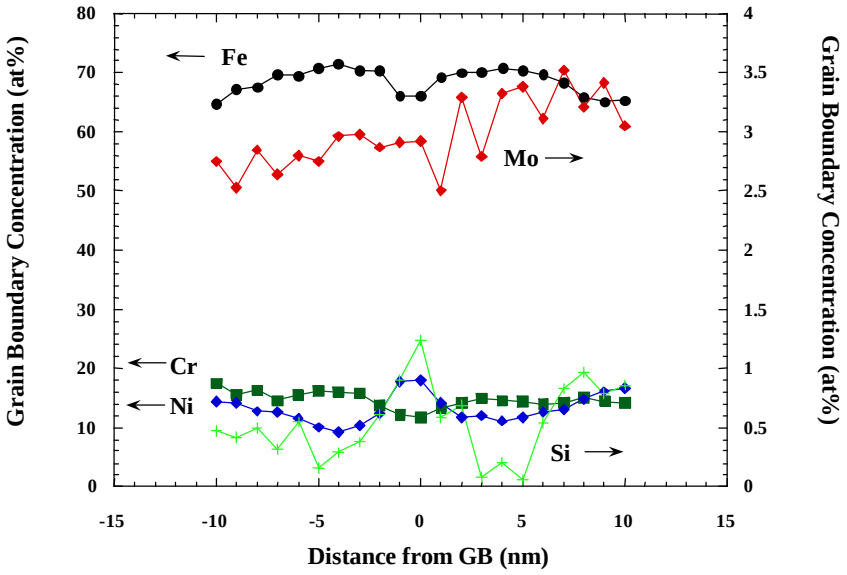

Figure B5. Grain Boundary 1 Profile 001

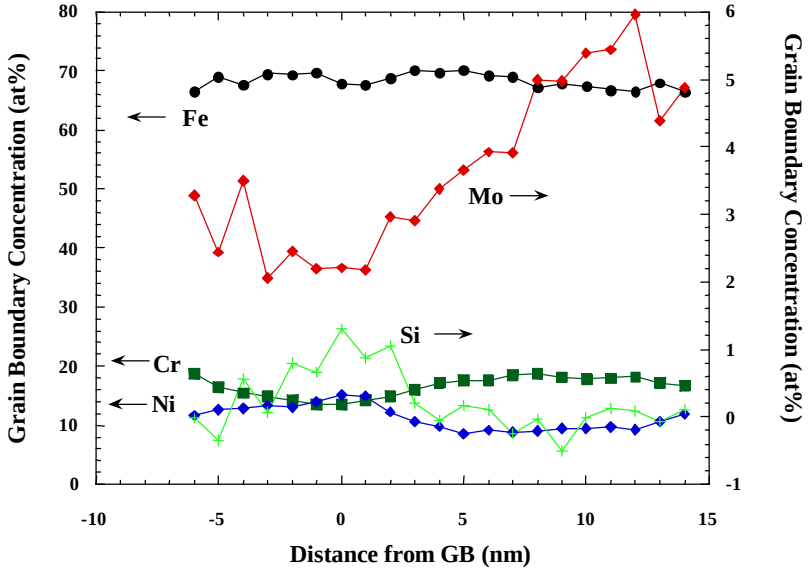

Figure B6. Grain Boundary 1 Profile 002

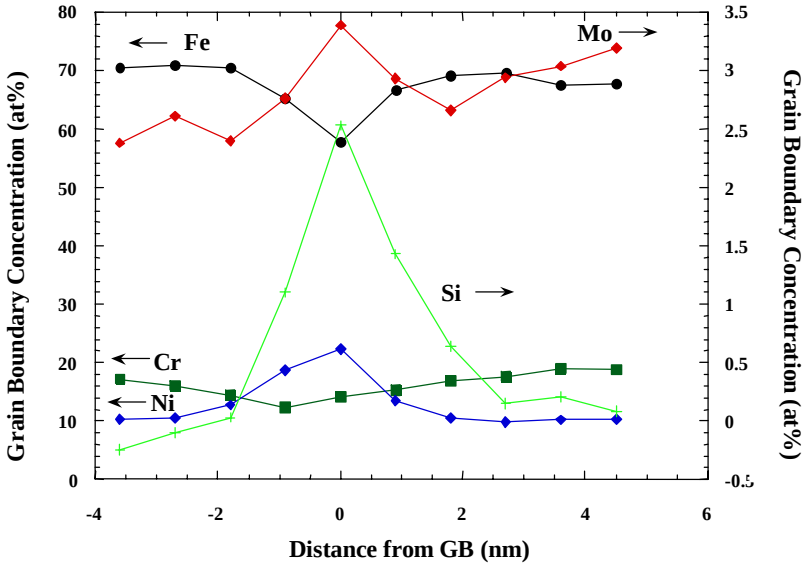

Figure B7. Grain Boundary 1 Spectrum Image 1

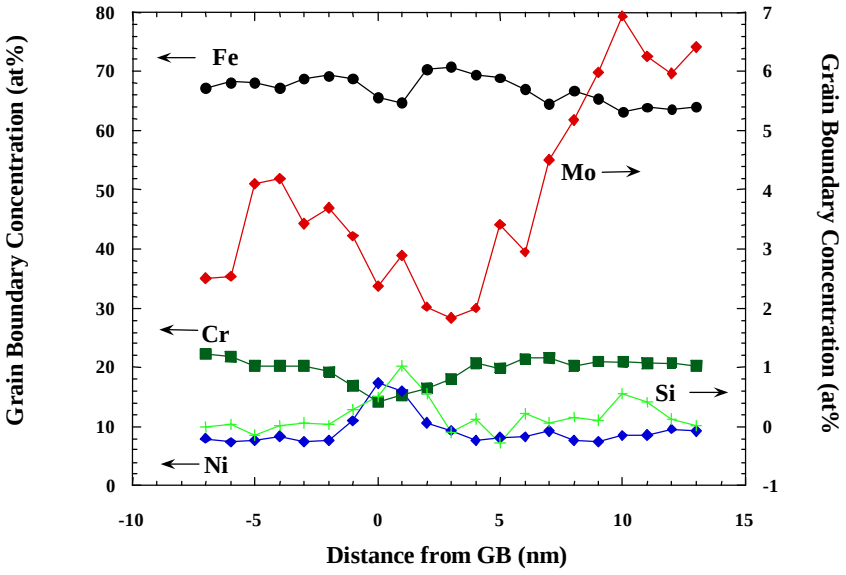

Figure B8. Grain Boundary 2 Profile 003

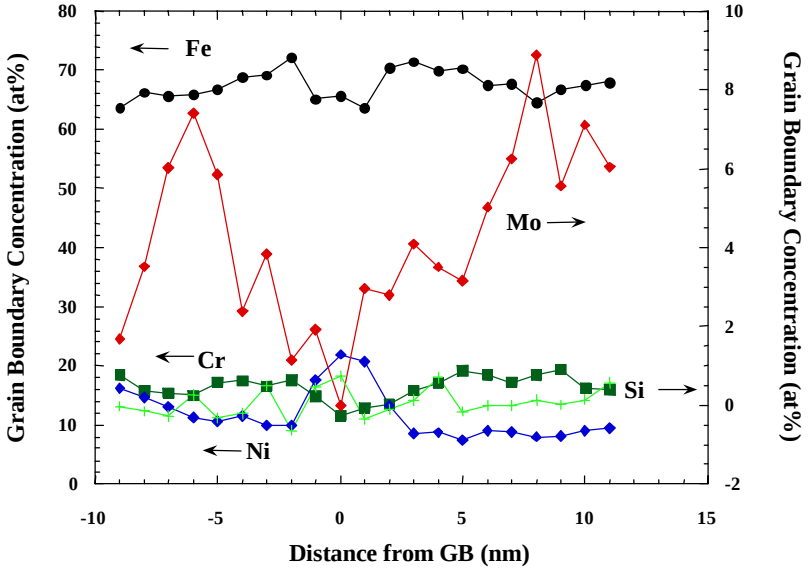

Figure B9. Grain Boundary 2 Profile 004

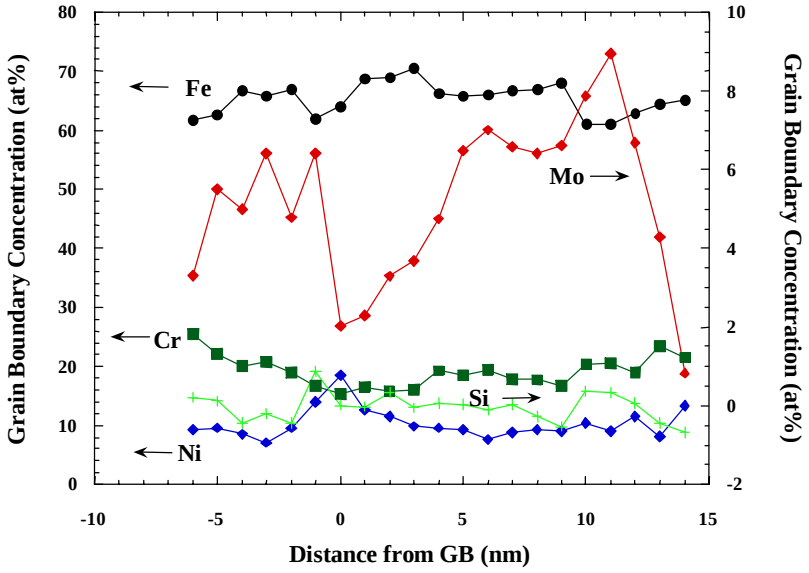

Figure B10. Grain Boundary 2 Profile 005

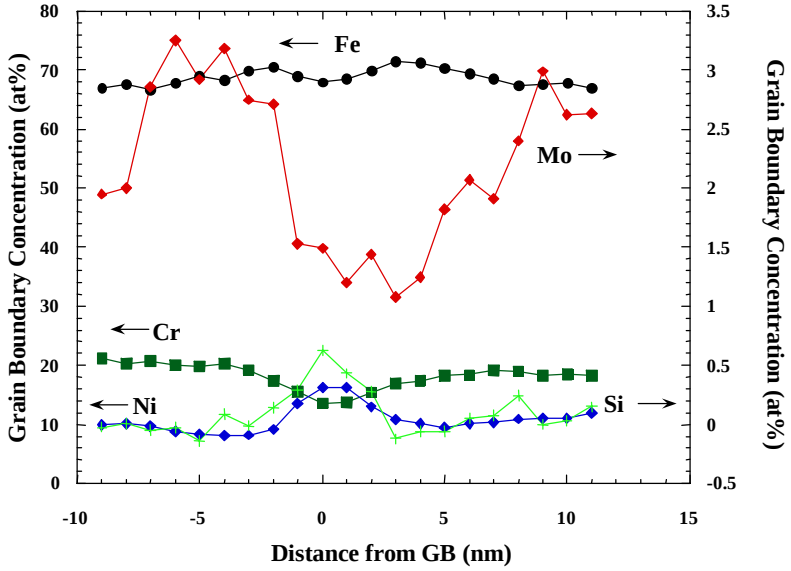

Figure B11. Grain Boundary 2 Profile 006

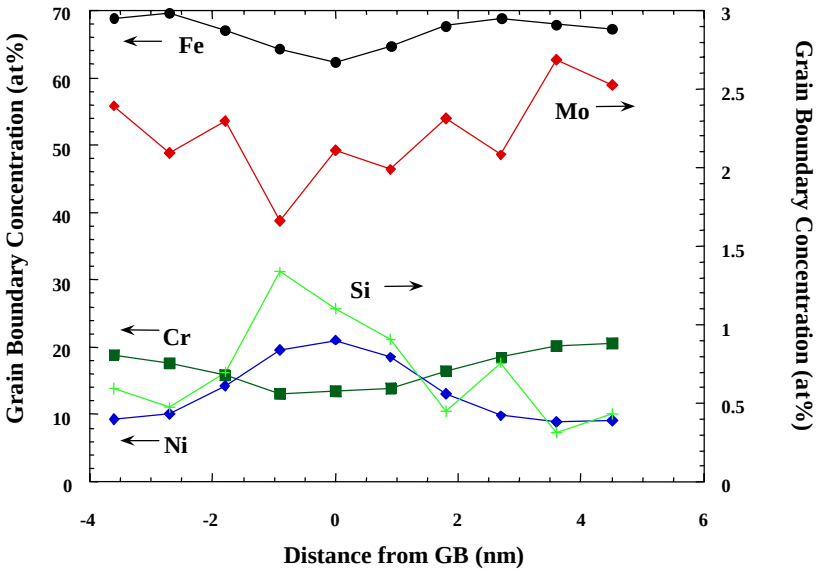

Figure B12. Grain Boundary 2 Spectrum Image 003

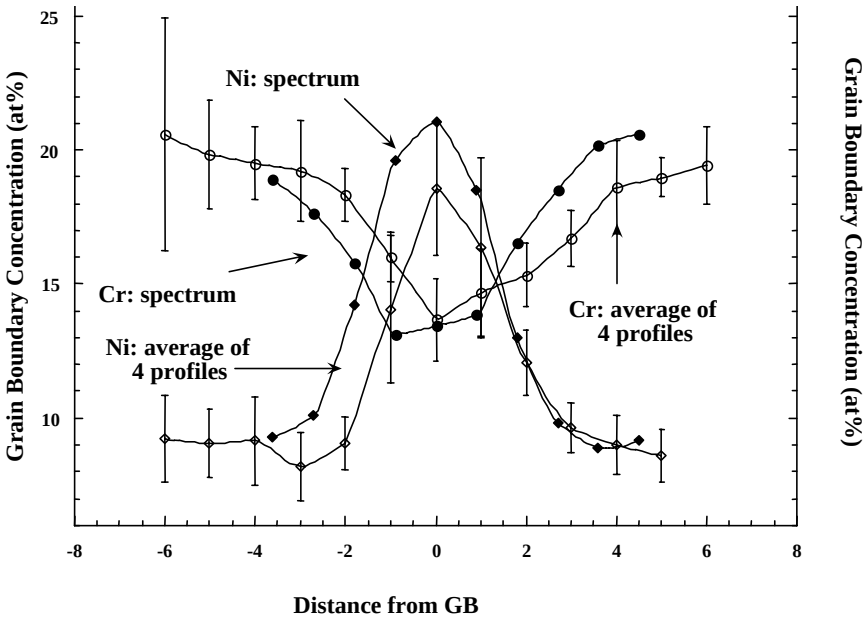

Figure B13. Comparison of profiles with Spectrum Images

B3. Grain Boundary Composition Measurements at 30 dpa

Table B5. Grain boundary 2 composition measurements (at%)

	Fe	Cr	Ni	Mo	Si
Spectra					
Grain Boundary	65.0	16.5	17.3	0.9	0.3
Grain Boundary (Prof)	64.2	15.9	18.7	1.0	0.4
Grain Boundary (Prof)	66.3	15.3	17.0	1.1	0.3
Grain Boundary (Prof)	66.7	16.7	15.1	1.2	0.3
Grain Boundary (SI)	66.9	15.5	16.9	0.6	0.1
Grain Boundary (SI)	67.8	15.6	15.5	0.9	0.3
Average Grain Boundary	66.2	15.9	16.8	1.0	0.3
Matrix	65.2	20.2	11.7	2.5	0.4
Matrix	67.0	19.8	10.9	2.0	0.3
Average Matrix	66.1	20.0	11.3	2.3	0.4
Average Segregation (matrix-GB)	0.1	-4.1	5.5	-1.3	-0.1
Maximum Segregation (avg matrix-GB)	-1.9	-4.7	+7.4	-1.4	-0.3
Precipitate 1	55.06	24.81	15.32	1.69	3.11
Precipitate 2	48.56	25.92	19.98	2.01	3.53
Precipitate 3	57.90	15.97	22.46	1.36	2.30

Prof=from a profile measurement
SI=from a spectrum image measurement

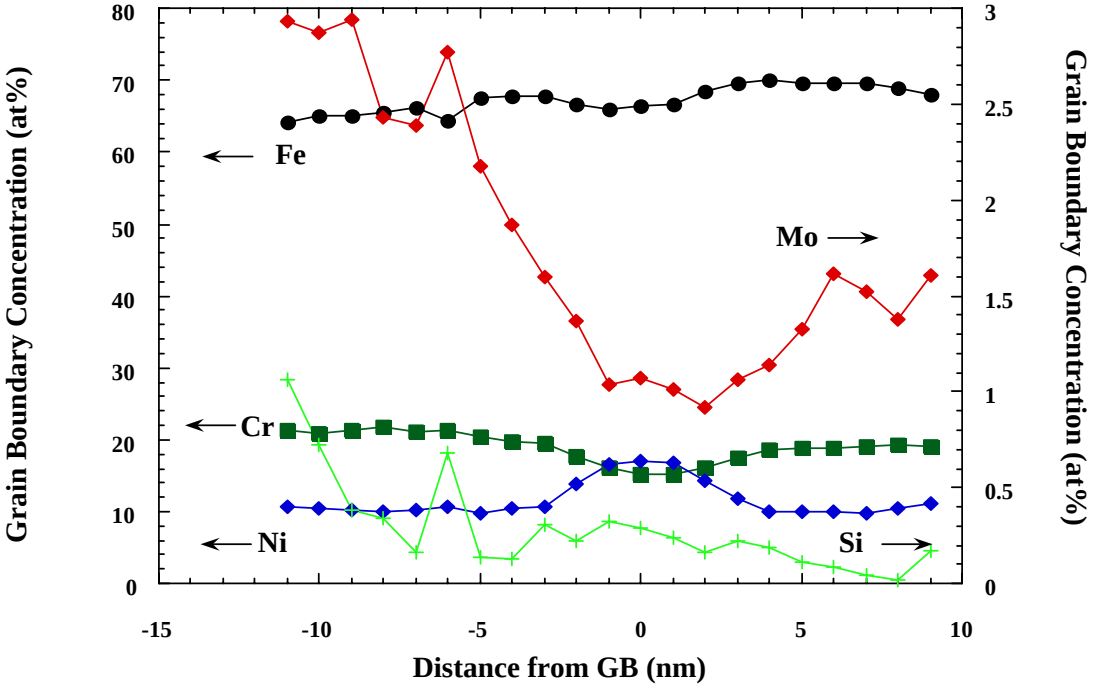

Figure B14. Grain Boundary 1 Profile 003

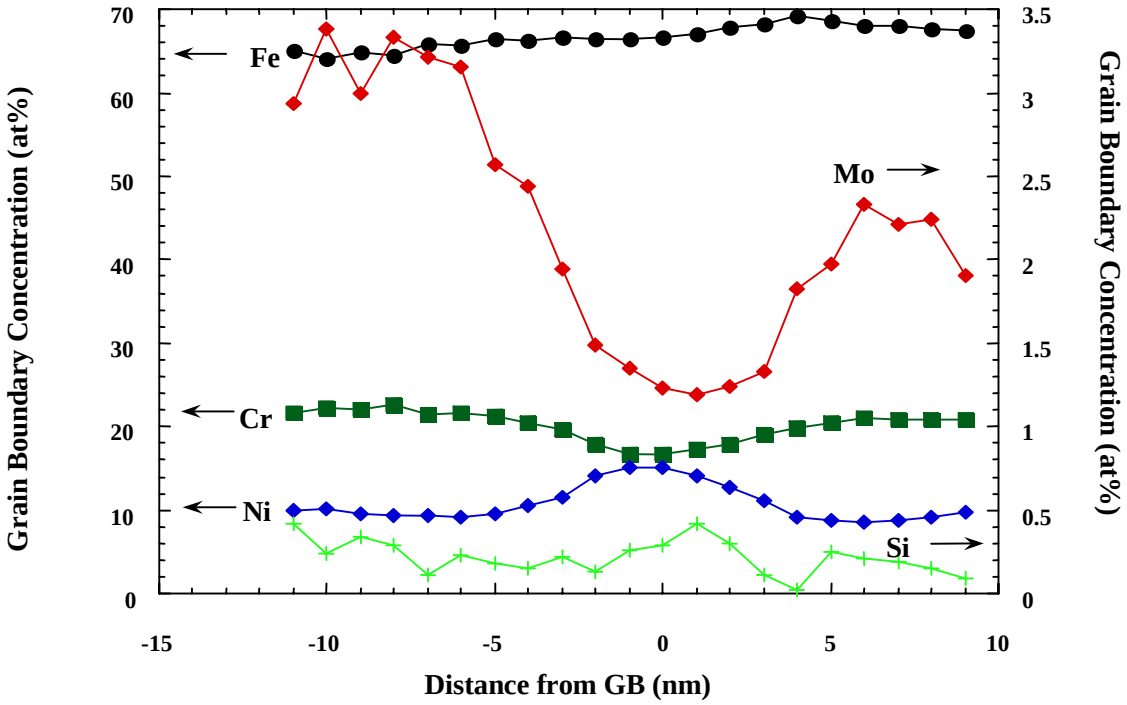

Figure B15. Grain Boundary 1 Profile 004

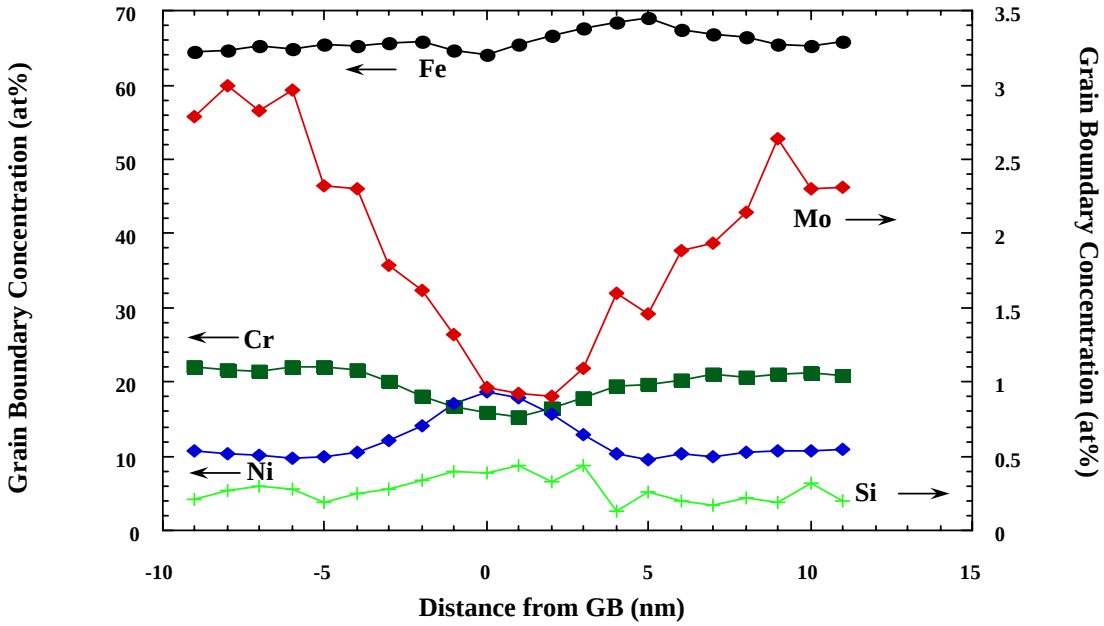

Figure B16. Grain Boundary 1 Profile 005

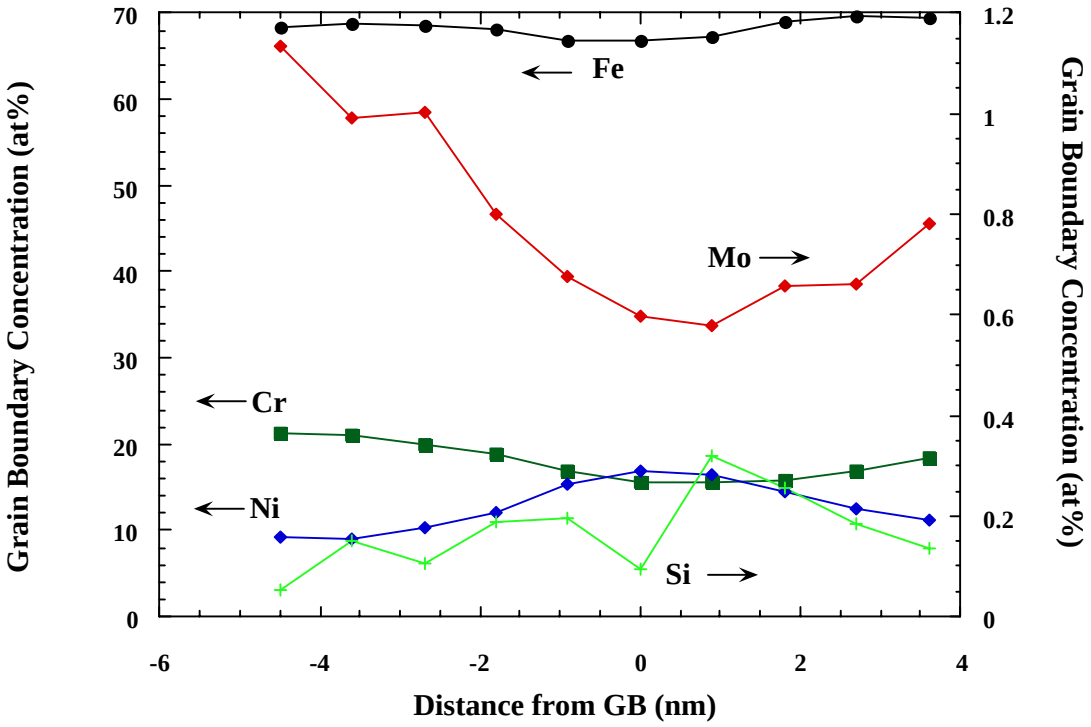

Figure B17. Grain Boundary 1 Spectrum Image 001

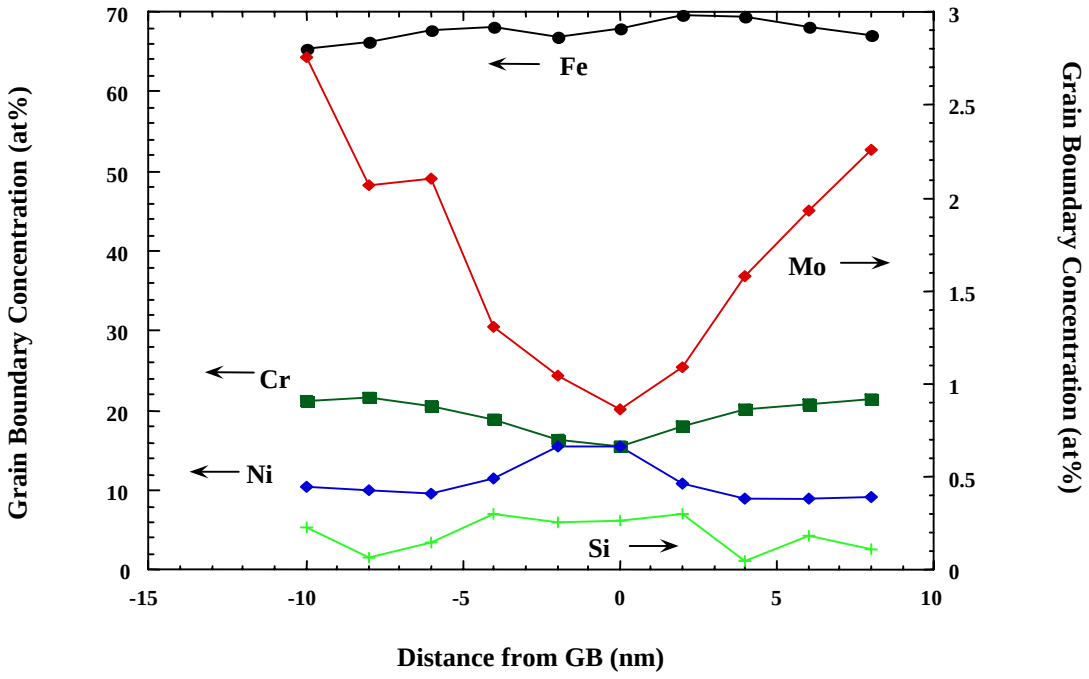

Figure B18. Grain Boundary 1 Spectrum Image 002

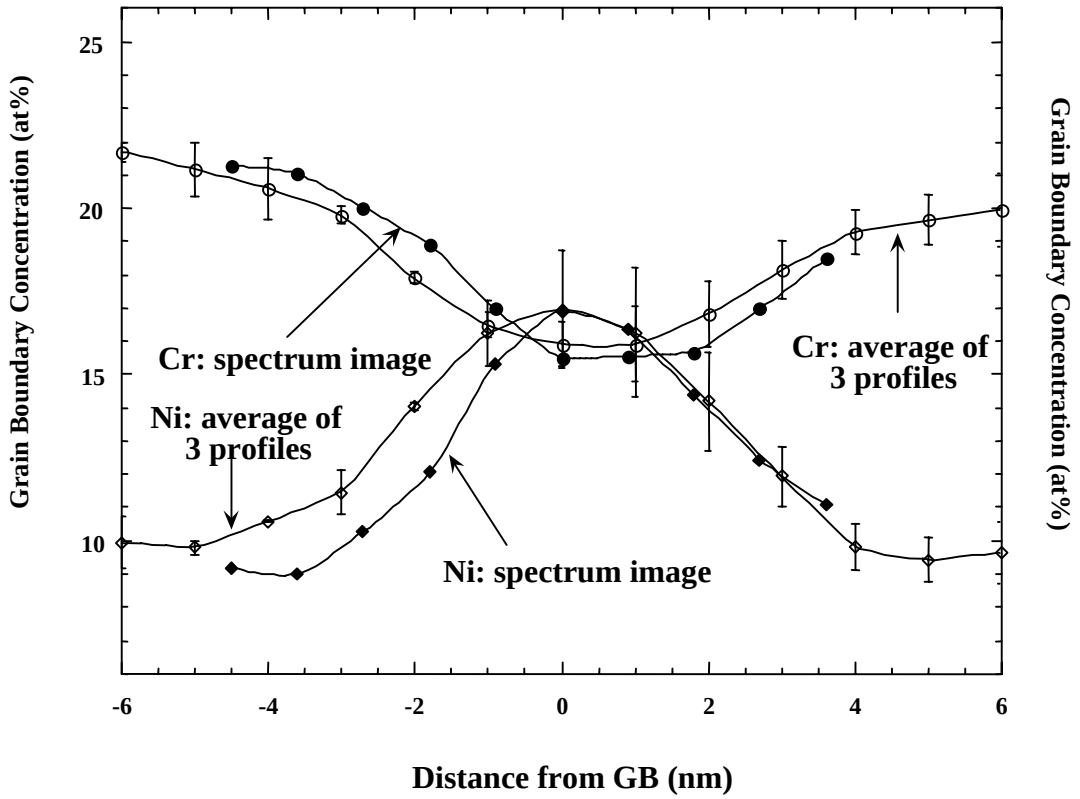

Figure B19. Comparison of profiles with Spectrum Image 002

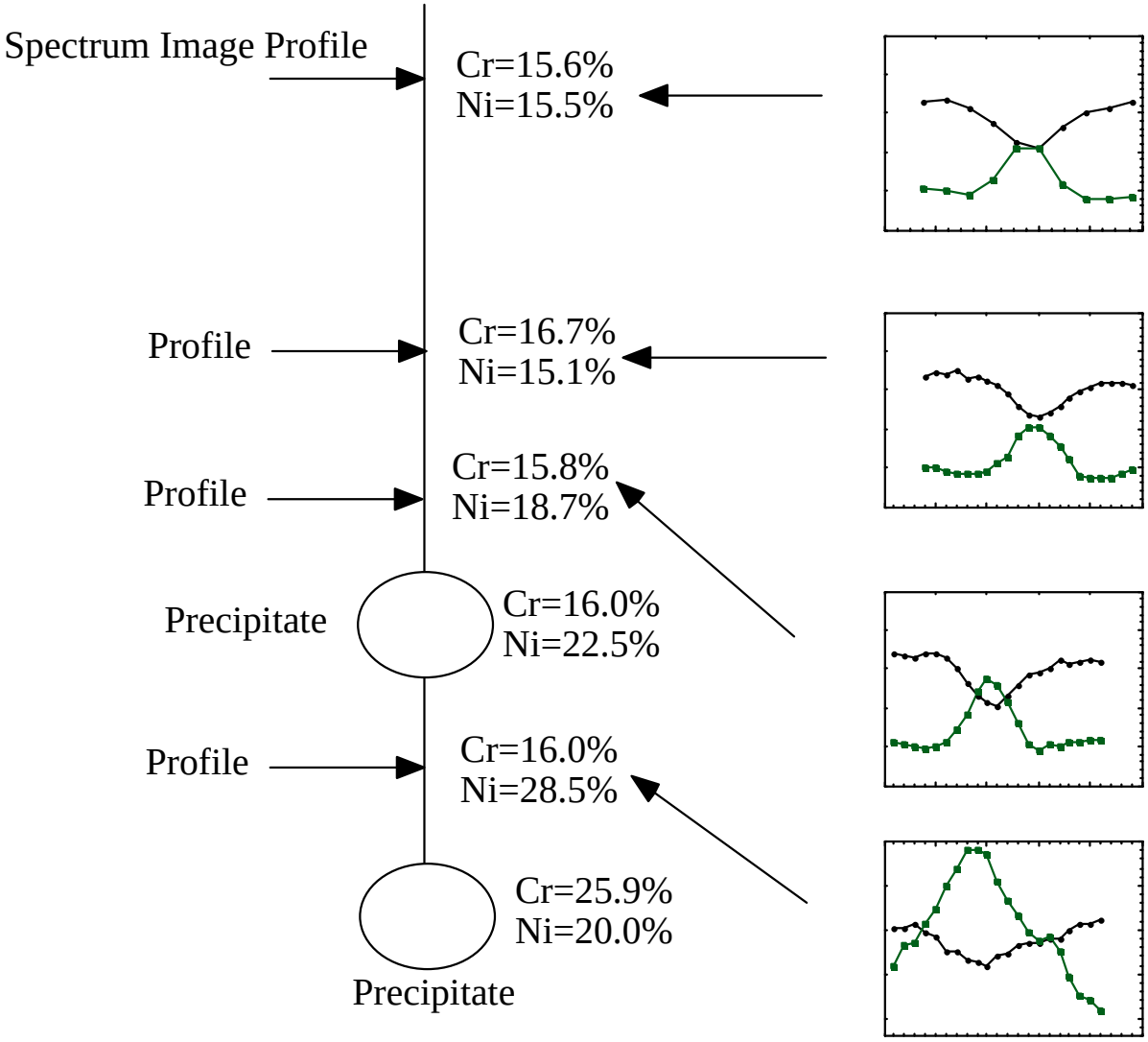

Figure B20. Grain boundary Composition near and away from a precipitate